Erlend Elias Isachsen

Dielectric Response of Phosphorene Subject to Strain

Master's thesis in Nanotechnology (MTNANO)
Supervisor: Mohammad Alidoust and Jaakko Akola
June 2021

Master's thesis

NTNU
Norwegian University of Science and Technology
Faculty of Natural Sciences
Department of Physics

NTNU
Norwegian University of
Science and Technology

Erlend Elias Isachsen

Dielectric Response of Phosphorene Subject to Strain

Master's thesis in Nanotechnology (MTNANO)
Supervisor: Mohammad Alidoust and Jaakko Akola
June 2021

Norwegian University of Science and Technology
Faculty of Natural Sciences
Department of Physics

NTNU
Norwegian University of
Science and Technology

Abstract

This thesis presents a theoretical study of the dielectric response of the two-dimensional (2D) material phosphorene, subjected to strain. The analysis starts from an effective low-energy $\mathbf{k} \cdot \mathbf{p}$ Hamiltonian, from which the valence and conduction bands are obtained, revealing anisotropic behaviour along the zigzag (x) and armchair (y) directions. The bandgap increases proportionally to applied strain, and ranges from 0.56 eV to 2.48 eV. Compressive strain shifts the conduction band below the Fermi energy, yielding metallic properties.

The optical conductivity $\sigma_{\alpha\beta}$ is obtained via the Greenwood-Kubo current-current correlator, and is anisotropic with the greatest dielectric activity in the y-direction. Elevating the chemical potential μ into the conduction band introduces Drude conductivity, and raises the interband transition energy by $\sim 2\mu$. The dynamic relative permittivity ϵ_r is obtained from $\sigma_{\alpha\beta}$, and essentially resides between 0 to 2 in the x-direction, and -5 to 30 in the y-direction, including photon frequencies Ω where $\epsilon'_{r,yy}(\Omega) = 0$. The Drude weights are obtained from both the band structure and the optical conductivity, with perfect agreement between the two. Overall, the results match physical expectations, experimental results and the available literature.

As an extension to the thesis, an attached manuscript presents an equivalent analysis utilising density functional theory with a random phase approximation (DFT-RPA). In contrast to the low-energy model, it shows how common DFT-RPA approaches are unable to reveal intricate features of the optoelectrical properties of 2D materials, and how they disagree with physical expectations. It also shows how accurate predictions of the dielectric response are essential for designing optoelectronic devices.

Sammendrag

I denne avhandlingen presenteres en teoretisk studie av den dielektriske responsen for det to-dimensjonale (2D) materialet fosforén utsatt for deformasjon, med utgangspunkt i en effektiv lav-energi $\mathbf{k} \cdot \mathbf{p}$ Hamilton-operator. Først blir valens- og ledningsbåndet regnet ut, som avdekker anisotrope egenskaper i sikksakk (x) og armstol (y) retning. Båndgapet øker proporsjonalt med påførte strekkrefter i xy-planet, og varierer fra 0.56 eV til 2.48 eV. Komprimerende krefter reduserer energien til lendingsbåndet under Ferminivået, som resulterer i metalliske egenskaper.

Den optiske ledningsevnen $\sigma_{\alpha\beta}$ ble regnet ut via Greenwood-Kubo strøm-strøm relasjonen, og er anisotropt med den største optiske aktiviteten i y-retningen. En økning av det kjemiske potensialet μ inn i ledningsbåndet introduserer Drude ledningsevne, og øker minsteenergien for bånd-til-bånd eksitasjoner med ca. 2μ. Den relative permittiviteten ϵ_r regnes ut fra $\sigma_{\alpha\beta}$, og ligger generelt mellom 0 og 2 i x-retning og -5 til 30 i y-retning. Sistnevnte inkluderer enkelte fotonfrekvenser Ω hvor $\epsilon'_{r,yy}(\Omega) = 0$. Drude-vektene regnes ut fra både båndstrukturen og den optiske konduktiviteten, og det viser seg å være perfekt samsvar mellom dem. Helhetlig samsvarer resultatene godt med fysiske forventninger, eksperimentelle resultater og litteraturen.

Som en utvidelse til avhandlingen er det vedlagt et manuskript som presenterer en ekvivalent analyse, som bruker tetthets-funksjonell teori med en tilfeldig-fase tilnærming (DFT-RPA). I motsetning til lavenergimodellen, viser manuskriptet hvordan populære DFT-RPA metoder ikke klarer å modellere de intrikate fotoelektriske egenskapene til 2D materialer, og hvordan de motsier fysiske forventninger. Manuskriptet forklarer også hvorfor nøyaktig modellering av dielektrisk respons er essensielt for å designe fotoelektriske kretser.

Acknowledgements

Contents

1 Introduction

The interaction between light and matter has been an important topic within physics for centuries, boosted by the discovery of the photovoltaic effect and photoconductivity in the 19th century by Alexandre Becquerel and Willoughby Smith, respectively [1, 2]. However, it was not before the 20th century that Max Planck and Albert Einstein developed a theoretical fundament for such processes, through the description of light as packets with quantized energy called photons [3, 4]. A lot of advances have been made since then through the development of quantum field theory and solid-state physics, making it possible to describe light-matter interactions from first principles. Light-matter interactions remain a central topic in modern physics and engineering, with a high demand for better photoelectrical devices and characterization methods of materials' photonic properties.

Accurate models for the dielectric response are essential for material physics and the development of optoelectronic devices. At the heart of dielectric modelling is the optical conductivity and permittivity, where the latter governs several measurable quantities such as the refractive index, absorbance, capacitance and electrical power dissipation. Techniques such as density functional theory (DFT) and low-energy models are excellent theoretical tools that have been proven useful to calculate the dielectric response of numerous ground-breaking materials.

In modern times, two-dimensional (2D) materials have been studied intensely for their promising photoelectric properties. This includes the renowned graphene as well as other materials with similar structures such as silicene and phosphorene [5]. Some examples of unique photoelectric properties are ultra-high photosensitivity devices [6] and nanosheet phototransistors with tenable energy gap [7, 8]. The tight dimensional confinement of charges leads to intriguing quantum mechanical effects not seen in their bulk counterparts, such as the Hall conductivity [9] and topologically protected phenomena [10].

This thesis presents a detailed study of the dielectric response of phosphorene subject to externally applied in-plane strain, obtained from a low-energy model of the system. Phosphorene is a single layer phosphorous that can be obtained from black Phosphorous, in the same sense that graphene is a single layer counterpart to graphite. A three-dimensional illustration of phosphorene is shown in Figure 1. The aim of this current study is to obtain the dielectric response functions from the fundamental properties of the material, employing quantum field theory and solid-state physics. More specifically, the goal is to calculate the optical conductivity, permittivity, and their related quantities, starting from an effective low-energy Hamiltonian. Then, the effect of strain and chemical potential μ on these properties shall be investigated within a low-energy regime. A deep analysis of the band structure, obtained from the effective Hamiltonian, will be performed to develop a good physical foundation to interpret the dielectric response functions from. This includes an analysis of the chemical potential dependency of the Drude weights, obtained from both the band structure and the optical conductivity.

For the band structure analysis, the conduction and valence bands will be obtained from the Hamiltonian analytically. By analysing the curvature of the conduction band, the Drude weights will be obtained numerically from the band structure. Next, the real part of the optical conductivity will be calculated numerically from the Hamiltonian through the Greenwood-

Kubo current-current correlator formula in its spectral representation. This is done by employing the Hamiltonian's corresponding Green's functions as an intermediate step. As the numerical evaluation is computationally highly demanding, an algorithm optimized for both central processing units (CPUs) and graphical processing units (GPUs) is developed and compared in terms of performance. An analytical expression for the first **k**-integrals of the optical conductivity is obtained, that incorporates both compressive and tensile in-plane strain.

The imaginary part of the optical conductivity is obtained from the real through the Kramer-Kronig relation. Next, the permittivity and the μ-dependent Drude weights will be obtained from the complex optical conductivity. Finally, the Drude weights that were calculated from both the band structure and the optical conductivity will be compared to link the band structure to the very-low-energy part of the optical conductivity.
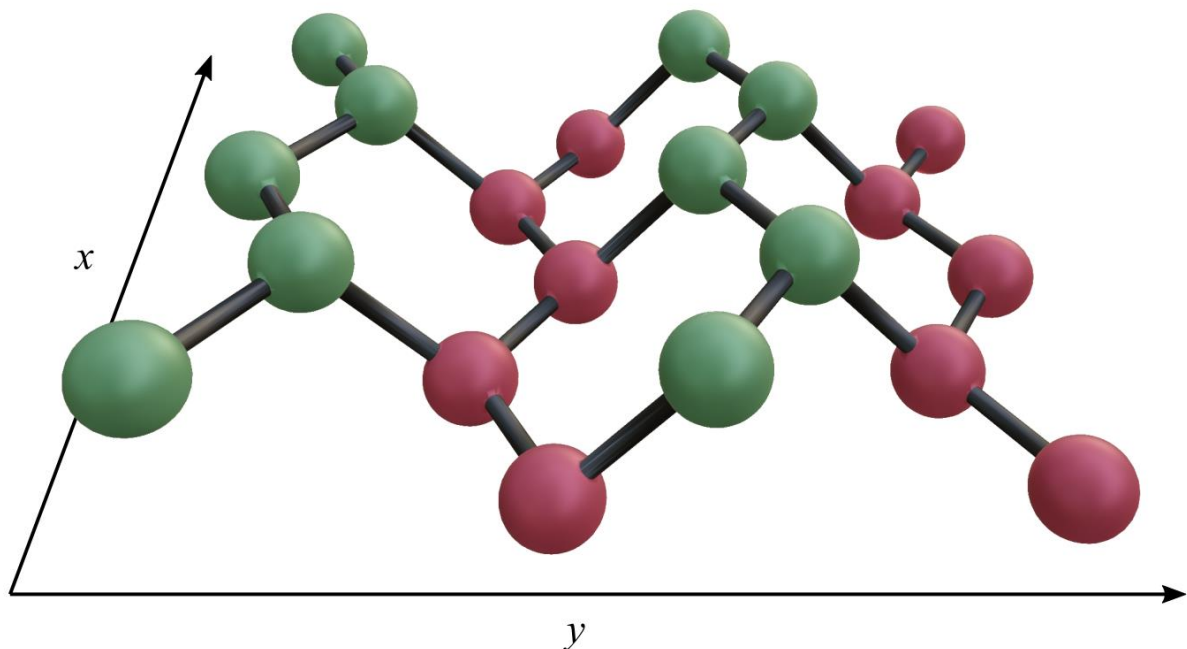

Figure 1: 3D view of the crystal structure of phosphorene, where the green and red points illustrate phosphorous atoms that reside in two different, parallel planes.

2 Theory

2.1 Fundamentals of solid-state physics and the k · p method

Materials can fundamentally be classified as either crystalline or non-crystalline (amorphous) materials. Crystalline materials can be described as a periodic assembly of atoms and cover a large range of the known materials including metals, rocks and ceramics. These are the materials that will be discussed in detail in the following sections, using the periodic representation to describe the electrical properties of the material. This is the standard crystalline representation used in solid-state physics.

In this description of materials, groups of points (the basis) are translated along vectors that span the entire lattice, called primitive vectors. Therefore, the basis and the primitive vectors are defined in such a way that all possible integer translations along the vectors construct the entire lattice. Each point is unique and none of the vectors are linear combination of one another. The primitive vectors each define what is referred to as a crystal axis, and properties such as conductivity and ultimate yield strength can vary along each crystal axis. Using this definition, atoms or charged carriers can be imposed on these points to describe the material. To describe the entire space within the lattice, the smallest unit of volume that is repeated through the lattice is called a primitive cell and can be translated along the axes in the same manner as the points.

While the real-space lattice contains a lot of useful properties of the structure, additional information can be extracted by applying a Fourier transform to the lattice. The result is a related lattice expressed in momentum-space, referred to as the reciprocal lattice with units of inverse length: m^{-1}. The reciprocal analogue to the real-space primitive cell is called a Brillouin zone. Due to the periodicity of the lattice, most interesting physical properties are contained within the first Brillouin zone. There are several important symmetry points in the reciprocal lattice such as the Γ-point in the centre of the Brillouin zone, M-points at the centre of an edge and K-points at the centre of an edge between two hexagonal faces.

Using the momentum-space representation of the crystal lattice, energy band diagrams can be constructed. The classical definition of a structure's band diagram is a domain of the allowed energy states for particles following Fermi-Dirac statistics, in essence allowed electron energy states for various electron momentums. Fermi-Dirac statistics are valid for electrons and other identical particles of half-integer spin, also called fermions, at thermal equilibrium. Regions in the band structure of forbidden momenta and energies are called band gaps [7].

The band structure of a specific solid can be calculated using the time-independent Schrödinger equation (SE), represented using a total wavefunction $\psi^\lambda(\mathbf{k}, \mathbf{r})$, which are eigenfunctions of the single-electron SE:

$$H\psi_n^\lambda(\mathbf{k}, \mathbf{r}) = E_n(\mathbf{k})\psi_n^\lambda(\mathbf{k}, \mathbf{r}). \tag{2.1.1}$$

Here, $E_n(\mathbf{k})$ are the allowed eigenenergies of the system, H is the Hamiltonian, $\mathbf{k}$ the wave vector, $\mathbf{r}$ a spatial vector, and λ the wavelength associated with the wavefunction [12]. In this equation, $\psi_n^\lambda(\mathbf{k})$ are eigenfunctions of the Hamiltonian operator, which has the corresponding eigenvalues $E_n(\mathbf{k})$. Plotting all the energy eigenvalues for various values of $\mathbf{k}$ results in the

band structure of the solid. A traditional approach to derive the Hamiltonian of a given system following equation (2.1.1) is what is known as the method of invariants.

The method of invariants was first introduced in 1956 by Luttinger, and is rooted in the idea that the Hamiltonian must be invariant with the symmetry groups of a crystal structure within the approximation of being quadratic in the wave vector $\mathbf{k}$ [9]. Introducing this method to the Desselhaus-Kip-Kittel (DKK) model, the resulting $n \times n$ matrix Hamiltonian is referred to as the DKK Hamiltonian. The DKK model uses second-order degenerate perturbation theory, starting from the $\mathbf{k} \cdot \mathbf{p}$ equation (obtained from the SE):

$$\left[\frac{\mathbf{p}^2}{2m_0} + V(\boldsymbol{r}) + \frac{\hbar}{m_0} \mathbf{k} \cdot \mathbf{p} \right] u_n(\mathbf{k}, \mathbf{r}) = \mathbb{E}_n(\mathbf{k}) u_{n\mathbf{k}}(\mathbf{r}),$$
(2.1.2)

where $\mathbf{p}$ is the momentum vector, V electrical potential, m_0 the electron mass, $\hbar$ the reduced Planck constant. $u_n(\mathbf{k})$ are states that arise from expressing $\Psi_n^\lambda(\mathbf{k}, \mathbf{r})$ as Bloch functions in terms of a set of periodic functions:

$$\psi_n^\lambda(\mathbf{k}, \mathbf{r}) = u_{n\mathbf{k}}(\mathbf{r}) e^{i\mathbf{k} \cdot \mathbf{r}}.$$
(2.1.3)

$\mathbb{E}_n(\mathbf{k})$ is related to the energy eigenvalues $E_n(\mathbf{k})$ through:

$$\mathbb{E}_n(\mathbf{k}) = E_n(\mathbf{k}) - \frac{\hbar^2 k^2}{2m_0}.$$
(2.1.4)

If the states $u_{n\mathbf{k}}$ form a complete set of periodic function, the representation of $H(\mathbf{k})$ in the basis is exact. This approach is particularly efficient for isolated bands, and in a finite region in $\mathbf{k}$-space. This holds true for the low-energy analysis of many semiconductors where the charges in the conduction band are restricted to a narrow region in $\mathbf{k}$-space at thermal equilibrium.

The method of invariants offers a way to calculate the band structure of simple solids from fundamental quantum mechanical properties. Solving equation (2.1.1) for $E_n(\mathbf{k})$ reveals the $\mathbf{k} \cdot \mathbf{p}$ band structure of the solid [14]. Illustrations of various band structures are shown in Figure 2, where the lower band represents the valence band and the upper represents the conduction band. The method of invariants therefore offers a way to find the Hamiltonian, the band structure and numerous related properties for various solids, starting from the SE.

2.2 Properties of solids

Most physical properties of a material can be derived from the fundamental principles described in the previous section. Some of the important properties that will be covered in this section are conductivity characteristics, material classification, and dielectric response. Additionally, these will be linked to some of the material parameters that attribute to these properties, such as the band structure, chemical potential and strain.

Most of these properties are closely related to the band structure, and materials are also classified based on their band structure as insulators, semiconductors, metals and semimetals. All of these classifications can be understood by the illustration in Figure 2, showing an example band structure for an insulator, semiconductor, metal as 2 a), 2 b), 2 c), and 2 d) respectively. In this figure, the conduction band of the material is plotted as a red line, and the valence band as a blue line. The main difference between the material classifications is the bandgap, which is defined as the energy difference between the bottom of the conduction band and the top of the valence band. As seen in Figure 2, the band gap is the largest for insulators, and non-existent for semimetals and metals. For metals, the conduction band is partially filled with mobile electrons even at zero temperature [7].
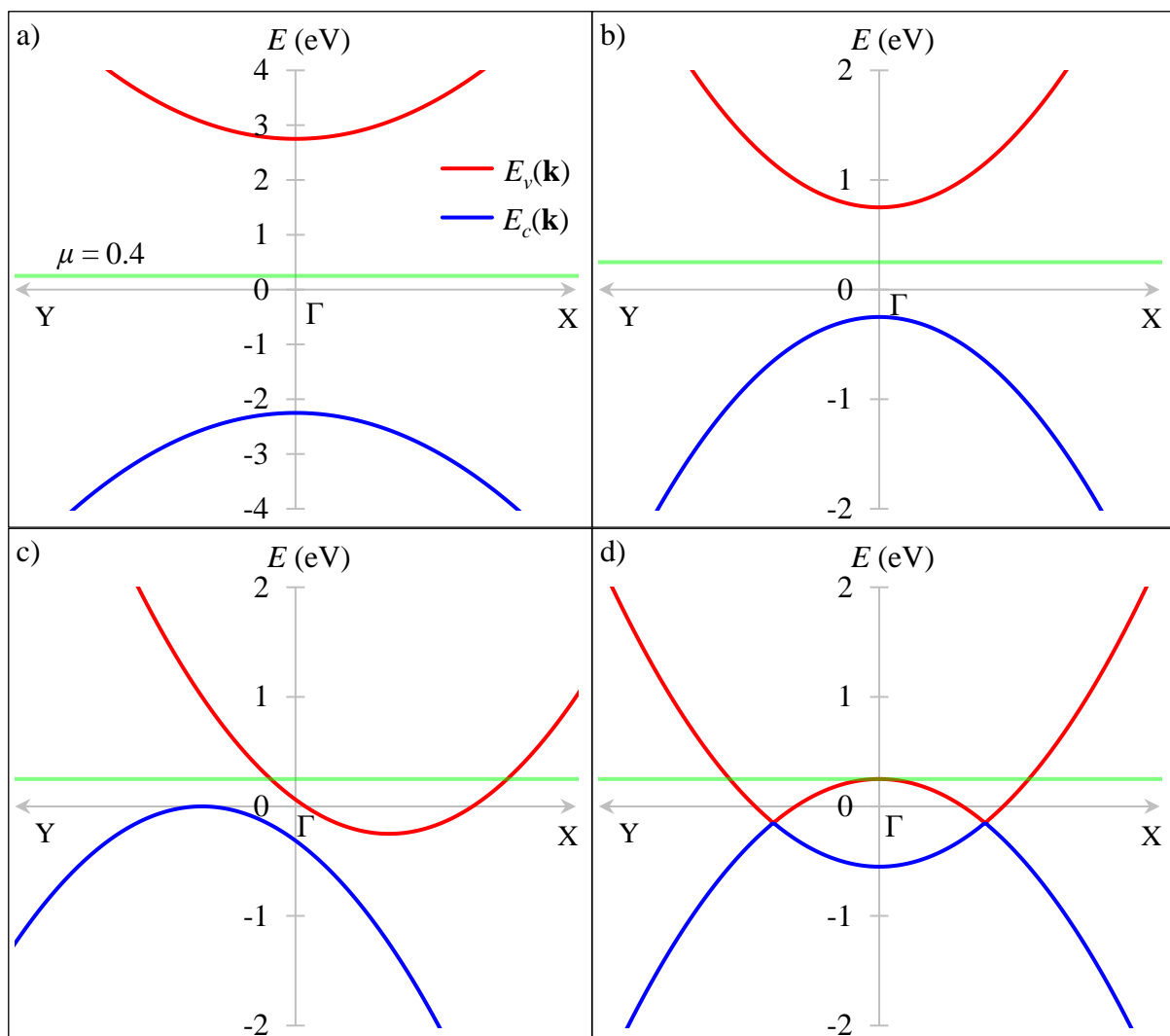

Figure 2: Illustration of the band structures for different types of materials. The valence band is shown in blue and the conduction band in red. a) illustrates an insulator while b) illustrates a semiconductor. c) shows a semimetal and d) a metal.

The partially filled conduction band in metals is the key characteristic that allows conduction at all temperatures. Overlapping states in the conduction and valence bands results in a surplus of available states, making the charge carriers conductive. For the same reason, semimetals will also conduct some electricity at zero temperature though the conduction band is nearly empty for most semimetals. The same type of conduction can also be introduced in semiconductors and theoretically in insulators by raising the chemical potential μ or thermally exciting electrons. The chemical potential is a measure of the electron concentration at a point and can be thought of as the Fermi-level E_F modified by an electrostatic potential $e\varphi(x)$ [7]:

$$\mu = E_F(x) - e\varphi(x) \cong \frac{\hbar^2}{2m_0} (3\pi^2 n_0)^{\frac{2}{3}}. \qquad (2.2.1)$$

Here, E_F is the Fermi energy, e the elementary charge and n_0 the thermal-equilibrium concentration of electrons. Increasing the chemical potential corresponds to raising the μ-line in Figure 2, and it sets the energy of the highest occupied electron state. With no external perturbations, all states below μ are filled. If the chemical potential is higher than the bottom of the conduction band, some metallic behaviour in terms of conduction arises. As can be seen from equation (2.2.1), the chemical potential can for instance be modified by changing the doping, which changes n_0.

Conductivity from free states at equilibrium is governed by the Drude model and is referred to as Drude conductivity. Since the Drude conductivity is determined by the level of μ relative to the conduction band, it can be described as a function of μ [7, 11]:

$$D_{\alpha\alpha}(\mu) \propto \int \delta\big(\mu - E_c(\mathbf{k})\big) \left(\frac{dE_c(\mathbf{k})}{dk_\alpha}\right)^2 d\mathbf{k}. \qquad (2.2.2)$$

Here, $E_c(\mathbf{k})$ is the conduction band, $\delta(\mathbf{k})$ the Dirac delta function and α an arbitrary crystal direction.

Changing μ is particularly interesting for semiconductors since the band gaps are so small that changing the chemical potential can drastically change the properties of the solid. Semiconductors can be grouped into four kinds, whose band structures are shown in Figure 3. Figure 3 a) shows a semiconductor with a direct bandgap, 3 b) shows a semiconductor with an indirect bandgap, 3 c) and 3 d) shows an n-type and p-type semiconductor, respectively. In terms of μ, the difference between 3 a), 3 c) and 3 d) is the most noteworthy. From these figures, it can be seen that changing the chemical potential can alter its n- and p-type characteristics. Raising the chemical potential by a great amount, will even introduce metal-like behaviour with the presence of Drude conductivity [12].
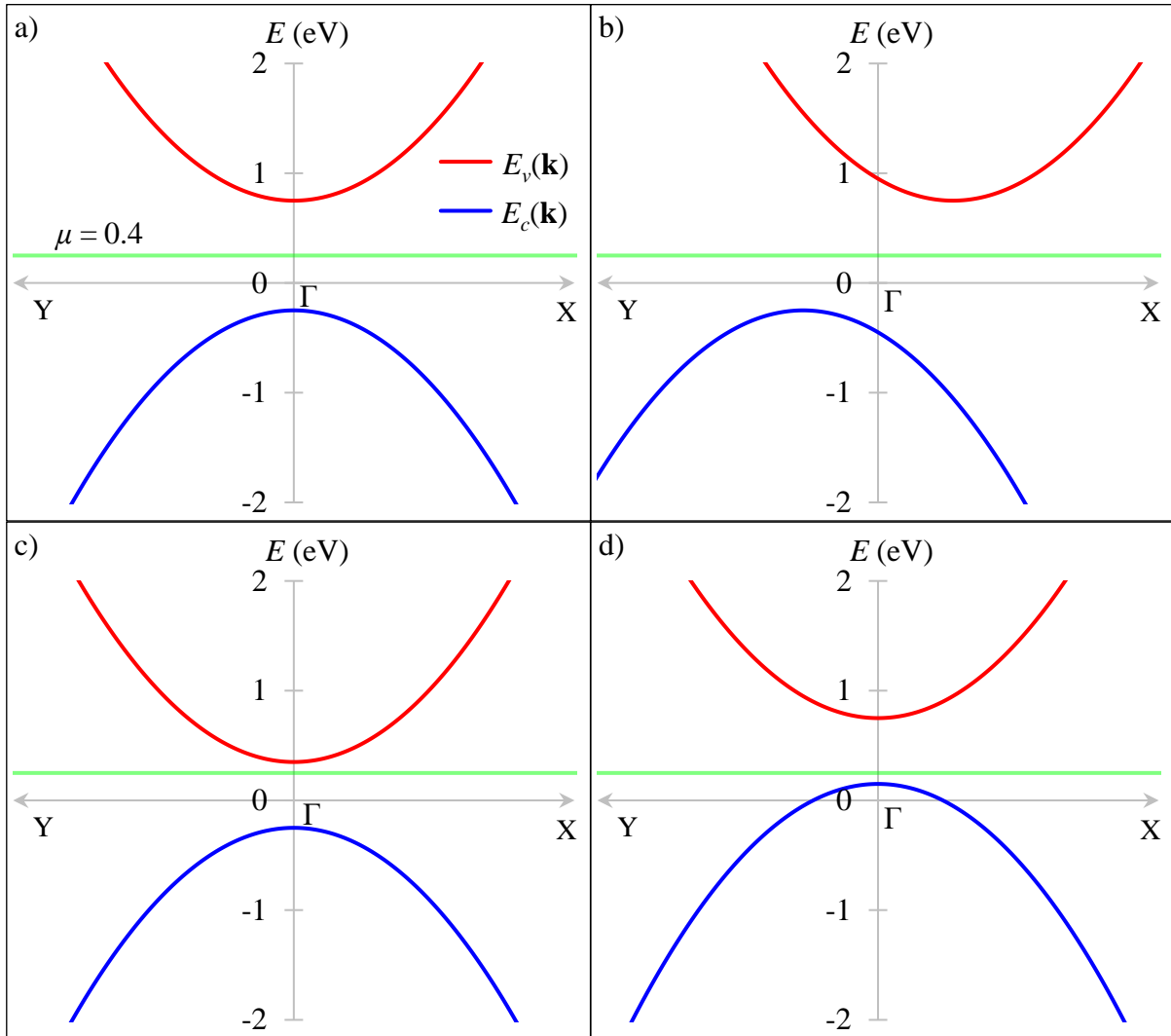
Figure 3: Illustration of the band structures for the different types of semiconductors. The valence band is shown in blue and the conduction band in red. a) belongs to a semiconductor with a direct bandgap, and b) to one with an indirect bandgap. c) and d) belongs to extrinsic semiconductors that are n-type and p-type, respectively.

Another useful property is the current density operator $\hat{J}$, which is closely related to the Hamiltonian. The current density operator can be derived from the Hamiltonian through the following relation [15, 17]:

$$\hat{J} = -\frac{e}{\hbar}\frac{\partial \mathbf{H}}{\partial \mathbf{k}}. \tag{2.2.3}$$

These are only some of the properties that are encapsuled in equation (2.1.1). Some other properties related to this equation is the optical conductivity and permittivity, which shall be discussed in greater detail in the next chapter.

2.3 Optical Conductivity

In the previous sections, the band structure of solids was presented as a potential lattice, resulting from the electrostatic forces created by the atoms at each lattice point. External electromagnetic forces can perturb the band structure and hence change the states of the electrons in this structure. When a solid is subjected to incident light, photons can interfere with the material in numerous ways: through reflection, transmission, and absorption. The two first phenomena will primarily leave the material unchanged and is therefore not addressed in detail here, while the latter gives rise to interesting physics within the solid.

Consider an incident photon of angular frequency Ω and energy $\hbar\Omega$ on a solid with a chemical potential μ as illustrated in Figure 4. Absorption of a photon can happen through electron transitions between different energy-momentum states within the solid. For a finite potential μ, all the states below are occupied and there are only a handful fermion transitions that are allowed by Pauli exclusion principle. Furthermore, such photon-electron interactions must also obey conservation of energy and momentum. Since the momentum of light is generally a lot smaller than the dimensions of the first Brillouin zone, transitions are predominantly vertical in the band diagram [14].
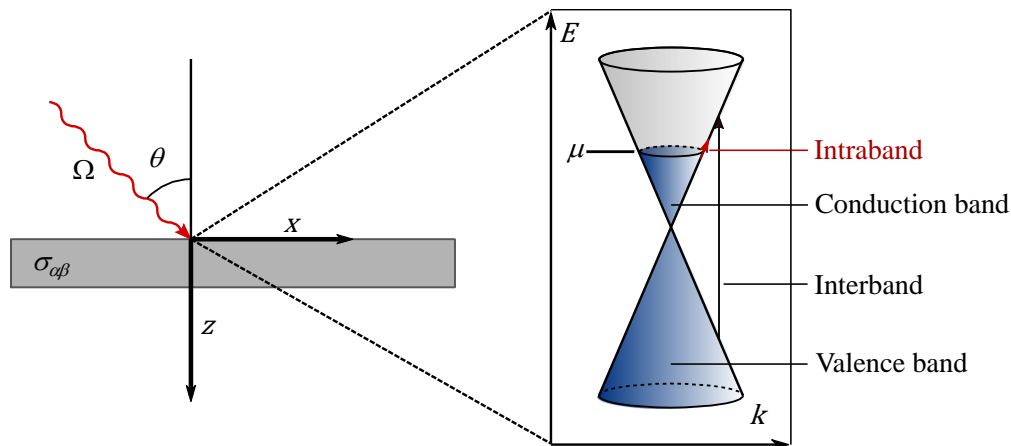
Figure 4: Illustration of the possible photon absorption processes of a low-energy band structure.

One of the allowed processes is called interband transitions, where a fermion is excited from one band to another. Using Figure 4 this process can occur for a photon of energy $\hbar\Omega \geq 2\mu$, though the exact photon energy required can vary between different band structures. In materials with a bandgap, the photon energy must also be greater than the energy of the gap. The essential requirements for the process, is that a state in the valence band is unoccupied for the same **k**-value in the conduction band. In this process, an electron is excited from the valence band to an unoccupied state in the conduction band, leaving behind a hole in the valence band. The valence band is represented as the lower cone, while the conduction band is described as the upper in Figure 4.

Another allowed process is intraband transitions. These are excitations of electrons between different states within the same band. In our model, such a transition is possible through the excitation of an electron just below μ to just above μ. This effect results in Drude conductivity, where the excited electrons are modelled as particles governed by kinetic theory [15]. For relatively steep band structures such as Figure 4, both the change of energy and momentum is

minimal in interband transitions. Both absorption effects results in conductivity, together comprising the optical conductivity of the material.

Finally, it is worth mentioning that photoelectric effects that are not directly vertical in the band diagram is possible. Since the photon momentum is too small to notably change the electron momentum, the momentum simply needs to be translated through other processes. One such process is interactions with vibrational modes in the lattice. The vibrational modes of the lattice are quantized through phonons, partly manifested as temperature. In other words, transitions in-between vertical and horizontal in the band diagram can happen through photon-electron-phonon interactions. Since a higher temperature results from a plethora of phonon modes, such indirect transitions can for the most part be ignored at lower temperatures. A second process is electron scattering, where electrons change momentum through collisions with the lattice. This is an important effect in the Drude model and can be quantized with a scattering parameter η [7].

Fundamentally, the connection between the optical conductivity and the band structure means that light can be used to obtain detailed information about the fundamental properties of a solid and vice versa. The optical conductivity of a material can be calculated using the Kubo formula, which for the electrical conductivity $\sigma_{\alpha\beta}$ is [11]:

$$\sigma_{\alpha\beta}(\mathbf{q}, \omega) = \frac{1}{\omega} \int_{-\infty}^{t} dt' e^{i\omega(t-t')} \langle \psi | [\hat{J}_{\alpha}^{\dagger}(\mathbf{q}, t), \hat{J}_{\beta}(\mathbf{q}, t')] | \psi \rangle + \frac{n_0 e^2}{m_0 \omega} i \delta_{\alpha\beta}, \qquad (2.3.1)$$

where α and β are arbitrary crystal directions, ω the angular fermion frequency with energy $\hbar\omega$, $\delta_{\alpha\beta}$ an unperturbed electron state, t and t' are different times and $\mathbf{q}$ is a displacement wave vector. This equation can be derived from the expectation value of the current density operator $\hat{J}_{\alpha\beta}(\mathbf{r}, t)$ imposed on ψ, representing the wave function appearing in the SE at time $t = 0$. The equation is valid for most 2D lattice systems since it is derived from the SE, the wave equation and a general Hamiltonian. Yet, it assumes that the steady-state current is zero $\langle \psi | j_{\alpha}(\mathbf{r}, t) | \psi \rangle = 0$.

For many problems, it is more convenient to write the Kubo formula in the Kubo-Greenwood representation. This representation uses a Green's function G related to the Hamiltonian through:

$$G^{-1}(\omega) = (\omega + i\eta)\tau_0 - H. \qquad (2.3.2)$$

The Green's function is a function of energy, η being a small scattering constant, and τ_0 the identity matrix. Often, it is useful to express the Green's function as a sum of two contributions, one being the retarded Green's function G^+ and the other being the advanced Green's function G^-. The former is used to evaluate how a field configuration will evolve from an initial state, while the latter is used to determine the history of a field ending at a certain state. By utilizing the retarded Green's function, the Kubo formula can be written in the Kubo-Greenwood formulation [16]:

$$\text{Re}[\sigma_{\alpha\beta}(\omega)] = \frac{g_v g_s e^2 \hbar}{\pi \Omega m_0^2} \int_{-\infty}^{\infty} dE \frac{f(E) - f(E + \hbar\omega)}{\hbar\omega}$$
$$\times \text{Tr}\{\hat{\mathbf{p}}_\alpha \text{Im}[G^+(E + \hbar\omega)] \hat{\mathbf{p}}_\beta \text{Im}[G^+(E)]\}, \tag{2.3.3}$$

where Ω is the angular frequency related to perturbation from the domain (such as an incident photon), $f(E)$ the Fermi function, $\hat{\mathbf{p}}_{\alpha\beta}$ the momentum operator and E energy. g_v and g_s are degeneracy factors accounting for symmetry- and spin-degeneracy, respectively. The Fermi function is defined as follows [17]:

$$f(x) = \frac{1}{e^{\gamma x} + 1}. \tag{2.3.4}$$

Here, $\gamma = (k_B T)^{-1}$ with k_B representing the Boltzmann constant and T the temperature. At zero temperature, the Fermi function becomes the Heaviside step function $f(x)_{T=0} = \Theta(-x)$.

By introducing a spectral function $\hat{A}(z)$, and rewriting the integral in the Greenwood-Kubo formula in terms of the wavenumber vector $\mathbf{k}$ and the current density operator $\hat{J}$, the optical conductivity can be written as follows [18]:

$$\text{Re}[\sigma_{\alpha\beta}] = \frac{g_s g_v}{2\Omega} \int_{-\infty}^{\infty} \frac{d\omega}{2\pi} [f(\omega - \mu) - f(\omega + \Omega - \mu)]$$
$$\times \int \frac{d^2 k}{(2\pi)^2} \text{Tr}[\hat{J}_\alpha \hat{A}(\mathbf{k}, \omega + \Omega) \hat{J}_\beta \hat{A}(\mathbf{k}, \omega)]. \tag{2.3.5}$$

Equation (2.3.5) is referred to as the many-body spectral representation of the Kubo formula. The spectral function introduced in this equation is related to the Green's function through:

$$\hat{G}_{ij}(z) = \int_{-\infty}^{\infty} \frac{d\omega}{2\pi} \frac{\hat{A}_{ij}(\mathbf{k}, \omega)}{z - \omega}. \tag{2.3.6}$$

The many body-spectral representation of the Kubo formula offers an efficient way to obtain the real part of the conductivity. However, the full optical conductivity consists of the real and imaginary parts. It is therefore necessary to introduce another relation, known as the Kramer-Kronig relation, which links the real part of the conductivity to its imaginary part. The Kramer-Kronig relation is a Hilbert transformation, that is defined as

$$\chi''(\Omega) = -\frac{2\Omega}{\pi} \int_0^{\infty} \frac{\chi'(\omega)}{\omega^2 - \Omega^2} d\omega, \tag{2.3.7}$$

where $\chi''(\Omega)$ is the imaginary response function of Ω related to the real response function $\chi'(\omega)$ [19]. The full conductivity is hence defined through the following expression, where the real and imaginary parts are denoted with a single and double apostrophe respectively:

$$\sigma_{\alpha\beta}(\Omega) = \sigma'_{\alpha\beta}(\Omega) + i\sigma''_{\alpha\beta}(\Omega). \tag{2.3.8}$$

2.4 Permittivity

By using the Kubo formula along with the Kramer-Kronig relation to arrive at equation (2.3.8), another closely related quantity is the permittivity. The permittivity of a material is a complex function defined as [19]:

$$\epsilon_{\alpha\beta}(\Omega) = \delta_{\alpha\beta} + \frac{4\pi i}{\Omega}\sigma_{\alpha\beta}(\Omega), \tag{2.4.1}$$

where $\delta_{\alpha\beta}$ is the Kronecker-delta, and the total permittivity is defined as $\epsilon(\Omega) = \epsilon_0\epsilon_r(\Omega)$ in which ϵ_0 is the vacuum permittivity and ϵ_r the relative permittivity. The real part of the permittivity is determined by the imaginary part of the optical conductivity, and the imaginary part by the real part. The permittivity is a measure of the polarizability of a dielectric material, in essence materials' ability to create an internal electric field in the presence of an external field. This effect is caused by displacement of the positively charged nucleus and the negatively charged electrons in a material, and is quantized by the polarization vector **P**. The external electric field is linked into the polarization and permittivity through:

$$\mathbf{P}(\Omega) = \epsilon_0\chi_e(\Omega)\mathbf{E}(\Omega), \tag{2.4.2}$$

in which χ_e is the electric susceptibility $\chi_e = \epsilon_r - 1$ and **E** denotes an external electric field. Furthermore, the permittivity is closely related to the electric displacement vector **D**:

$$\mathbf{D}(\Omega) = \epsilon(\Omega)\mathbf{E}(\Omega). \tag{2.4.3}$$

The relation in equation (2.4.2) describes the linearity of the medium, where a linear medium has a linear relationship between **E** and **P**. If additionally ϵ_r is a scalar, this in turn makes the medium isotropic. A material is also classified as homogeneous if ϵ_r is the same everywhere inside the material. Thus, studying the permittivity can determine if the material is linear, isotropic and or homogeneous [20].

For electronic devices, in particular interlayer insulators and capacitors, the permittivity is also a very important parameter. Because of the close relation between **D** and **E** seen in equation (2.4.3), the energy density w_e of an electric field is also determined by the permittivity through:

$$w_e = \frac{1}{2}\mathbf{D}\cdot\mathbf{E}. \tag{2.4.4}$$

For capacitors, a high energy density is crucial while a low energy density is desirable for interlayer insulators. Equation (2.4.4) does not hold for non-linear mediums, since time is of relevance in those cases. However, the underlying principle that the relative dielectric constant dictates the ability of a material to store electric energy still holds. The materials capacity to absorb electric energy is traditionally referred to as the dielectric constant κ, which is

essentially the same quantity as the real part of ϵ_r. In nanoelectronics, high-κ dielectrics for the gate oxide in transistors and capacitors are sought after, while low-κ dielectrics are sought after for the interlayer insulating layer between circuits. The capacitance C of a system separated by a dielectric materials is [12]:

$$C = \epsilon' \frac{A}{h},$$ (2.4.5)

where A and h are the area and width of the capacitor and ϵ' the real part of the dielectrics permittivity. If C is the capacitance between two plates separated by a dielectric medium with relative permittivity ϵ_r, and C_0 is the capacitance of the system with the dielectric replaced by vacuum, equation (2.4.5) can conveniently be rewritten as:

$$\epsilon'_r = \frac{C}{C_0}.$$ (2.4.6)

Equation (2.4.6) thus outlines measurable quantities to determine the relative permittivity of a material.

Setting up an electric field across a material with mobile charges will result in some conduction, and hence there will be an associated current. The current through a dielectric with an alternating voltage V with frequency ω is defined as:

$$I = i\omega\epsilon'_r C_0 V + \omega\epsilon''_r C_0 V.$$ (2.4.7)

The current consists of two components: one lossy and one lossless, where the latter is 90° out of phase with the applied field. The lossy part of equation (2.4.7) has some power dissipation associated with it, where the average power dissipation density is given by:

$$\bar{\rho} = \frac{1}{2}\omega E_0^2 \epsilon_0 \epsilon'_r \tan(\theta),$$ (2.4.8)

where θ is an angle related to the real and imaginary part of the permittivity through:

$$\tan(\theta) = \frac{\epsilon''_r}{\epsilon'_r}.$$ (2.4.9)

The relative permittivity therefore specifies how much electric energy is absorbed by the material. If either the real or imaginary part of ϵ is zero, it follows from equation (2.4.8) and (2.4.9) that the electric power dissipation is zero. The imaginary part of the permittivity arises from scattering processes of the electrons within the material. These include lattice vibrations or optical absorption in the case of electromagnetic disturbances [12].

Next, it is also possible to analyse the refractive index of a material based on the permittivity. The real refractive index of a material is defined through the following relation [21]:

$$n'_r = \sqrt{\epsilon'_r \mu'_r},$$
(2.4.10)

where μ_r is the relative permeability. The permeability reflects the magnetic properties of the material. If the permeability is close to 1, which is the case for many materials at optical frequencies, the refractive index becomes strictly dependent on the relative permittivity. In such a case, the full complex refractive index denoted as $n_r = n'_r + i\kappa''$ is related to the permittivity through [22]:

$$\epsilon_{r,\alpha\beta}(\Omega) = \left(n'_{r,\alpha\beta}(\Omega) + i\kappa''_{r,\alpha\beta}(\Omega) \right)^2.$$
(2.4.11)

The quantity $\kappa''_{r,\alpha\beta}$ is referred to as the extinction coefficient. Alternatively:

$$n'_{r,\alpha\beta}(\Omega) = \sqrt{\frac{|\epsilon_{r,\alpha\beta}(\Omega)| + \epsilon'_{r,\alpha\beta}(\Omega)}{2}}, \qquad \kappa''_{r,\alpha\beta}(\Omega) = \sqrt{\frac{|\epsilon_{r,\alpha\beta}(\Omega)| - \epsilon'_{r,\alpha\beta}(\Omega)}{2}}.$$
(2.4.12)

Here, $|\epsilon_{r,\alpha\beta}(\Omega)|$ is simply:

$$|\epsilon_{r,\alpha\beta}(\Omega)| = \sqrt{\epsilon'_{r,\alpha\beta}(\Omega)^2 + \epsilon''_{r,\alpha\beta}(\Omega)^2}.$$
(2.4.13)

The refractive index encapsulates a lot of interesting physics such as the refraction of light and speed of light within the medium. Furthermore, the refractive index is linked to other physical quantities such as the absorption coefficient A. The absorption coefficient is determined by the rate of electron-hole pair generation from interband transitions, and via the Fermi golden rule absorption of light polarized along a direction **a** is defined as [12]:

$$A = \frac{\pi e^2 \hbar}{m_0^2 c n'_r \epsilon_0} \frac{1}{\hbar\Omega} |(\mathbf{a} \cdot \mathbf{p})_{if}|^2 N_{cv}(\hbar\omega).$$
(2.4.14)

In this equation, many of the quantities such as the Planck constant $\hbar$, the elementary charge e, the speed of light in vacuum c, the electron mass m_0 and the vacuum permittivity ϵ_0 are physical constants. This means that the absorption coefficient varies from material to material based on the value of the dipole matrix element between the conduction and the valence band $|(\mathbf{a} \cdot \mathbf{p})_{if}|^2$, the joint density of states N_{cv} and finally the refractive index n_r. The dipole averaged matrix element is specific for a given material, or more precisely a specific band structure and is found to be $(2/3)p_{cv}^2$ in which p_{cv} is the momentum of charged carriers. For most semiconductors, $(2p_{cv}^2)/m_0 \cong 20$ to 24 eV.

The joint density of states is given by [12]:

$$N_{cv}(\hbar\omega) = \frac{\sqrt{2}(m_r^*)^{\frac{3}{2}}(\hbar\omega - E_g)^{\frac{1}{2}}}{\pi^2 \hbar^3}, \tag{2.4.15}$$

where m_r^* is the effective mass of the electron-hole system and E_g is the bandgap. The bandgap is defined as the energy difference between the top of the valence band and the bottom of the conduction band [7]. The essence of equation (2.4.14) and its related quantities is that the absorption coefficient of a material is ultimately determined by the band structure and the relative permittivity, given that the magnetic permeability μ_r is sufficiently close to 1. For instance, if the relative permittivity approaches zero, the refractive index n_r in turn approaches zero, which drives the absorption coefficient towards infinity. With a relative permittivity equal to zero, the material is a perfect absorber at that frequency.

2.5 Phosphorene

In section 2.1, the concept of a mathematical representation of crystalline materials was introduced. If a crystalline material can be described by translating the basis along only two primitive vectors, it is known as a two-dimensional material [7]. In these materials, the electrons have lower dimensional freedom, which leads to quantum confinement. This confinement in turn leads to distinctive properties not seen in 3D materials. For this reason, 2D materials have been extensively studied with the most famous example being graphene for its extraordinary mechanical and electrical properties.

A promising material, which alike graphene exhibits a 2D hexagonal structure, but puckered in the third dimension z, is phosphorene which will be discussed in this section. Phosphorene is a single-layer sheet of phosphorous atoms, which when stacked forms its three-dimensional (3D) counterpart called black phosphorous. Phosphorene is particularly interesting since has been found to a high carrier mobility up to 1000 $cm^2V^{-1}s^{-1}$ [23], and a relatively high on/off ratio in the order of magnitude of 10^4 [24]. Also, it was found in a theoretical study that the strain-engineered phosphorene can afford the Majorana zero energy modes and self-biased anomalous Josephson state, which makes phosphorene an intriguing platform for nanoelectronics and studying two-dimensional Dirac and Weyl superconductivity [25].

a)   b)
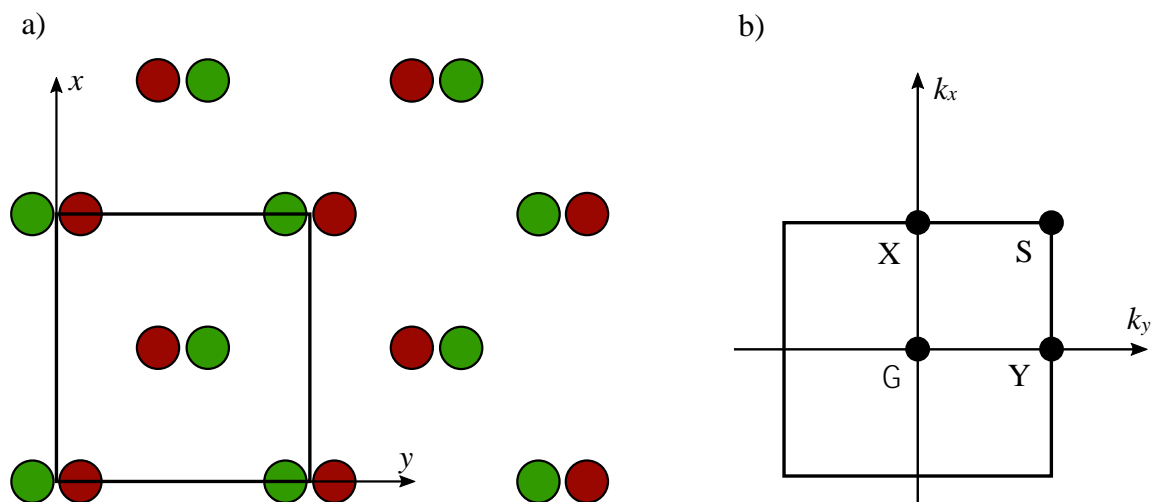

Figure 5: 2D illustration of the crystal structure of phosphorene in a) real space and b) reciprocal space. Some important symmetry points such as the Γ-, X- and Y-points are denoted in b).

A 3D illustration of the crystal structure of phosphorene is shown in Figure 1, where it is seen to have a puckered hexagonal structure. In crystallographic terms, it can be described as a non-symmorphic space group that is base-centred orthorhombic [26]. This representation and its reciprocal-space counterpart is shown in Figure 5. From these figures, it can be seen that the crystal structure of phosphorene is highly anisotropic between its zigzag (x) and armchair (y) directions.

Applying the method of invariants to the structure presented in Figure 5, an effective strain-dependent Hamiltonian can be constructed. The leading terms in one such Hamiltonian is shown in equation (2.5.1) [31]. In this model, strain is incorporated as the parameter $\mathcal{E}_{\alpha\beta}$ and is a spatial ratio. This means that $\mathcal{E}_{xx} = -0.1 = -10\%$ corresponds to a negative strain that

compresses the material by 10% in the x-direction shown in Figure 5. Similarly, $\mathcal{E}_{xx} = 10\%$ corresponds to a positive, tensile strain that elongates the material by 10% in the x-direction.

Considering strain in only the x- and y-directions, a low-energy $\mathbf{k} \cdot \mathbf{p}$ Hamiltonian $H(\mathbf{k})$ for phosphorene is [28]:

$$
\begin{aligned}
H &= \int \frac{d\mathbf{k}}{(2\pi)^2} \hat{\psi}_{\mathbf{k}}^\dagger H(\mathbf{k})\hat{\psi}_{\mathbf{k}} \\
&= \int \frac{d\mathbf{k}}{(2\pi)^2} \hat{\psi}_{\mathbf{k}}^\dagger \sum_{i,j=x,y} \left\{ \left[u_0 + \alpha_i \mathcal{E}_{ii} + \left(\eta_j + \beta_{ij}\mathcal{E}_{ii} \right)k_j^2 \right]\tau_0 \right. \\
&\qquad\qquad\qquad \left. + \left[\delta_0 + \mu_i \mathcal{E}_{ii} + \left(\gamma_j + \nu_{ij}\mathcal{E}_{ii} \right)k_j^2 \right]\tau_x - \chi_y \tau_y k_y \right\} \hat{\psi}_{\mathbf{k}},
\end{aligned}
\tag{2.5.1}
$$

where $u_0, \alpha_i, \eta_j, \beta_{ij}, \delta_0, \mu_i, \gamma_j, \nu_{ij}$ and χ_y are variables whose values are presented in Table 1. Here, τ_i are the Pauli matrices in pseudo-spin space [29]:

$$
\tau_0 = \begin{pmatrix} 1 & 0 \\ 0 & 1 \end{pmatrix}, \qquad \tau_x = \begin{pmatrix} 0 & 1 \\ 1 & 0 \end{pmatrix}, \qquad \tau_y = \begin{pmatrix} 0 & -i \\ i & 0 \end{pmatrix}.
\tag{2.5.2}
$$

Modelling phosphorene as presented in this section makes it possible to study several properties of the material, such as the mechanical properties. For instance, the strain-stress relation can be derived using the first-principles calculations. The first-principles calculations have shown that phosphorene subject to biaxial strain has an elastic stress-response in the range $\mathcal{E}_{xy} \in [-12\%, 22\%]$. Increasing the tensile strain beyond 22% results in plastic deformation, and phosphorene ultimately deforms into a flat hexagonal structure that is similar to graphene's at a biaxial strain of 0.29. For compressive strain plastic deformation occurs beyond a biaxial strain of -12% [31].

Table 1: Material-specific parameters for phosphorene, subject to externally applied in-plane strain $\mathcal{E}_{\alpha\beta}$ [31, 35].

u_0 (eV)	δ_0 (eV)	α_x (eV)	α_y (eV)	μ_x (eV)
-0.42	0.76	3.15	-0.58	2.65
μ_y (eV)	η_x (eVÅ^2)	η_y (eVÅ^2)	γ_x (eVÅ^2)	γ_y (eVÅ^2)
2.16	0.58	1.01	3.93	3.83
β_{xx} (eVÅ^2)	β_{yx} (eVÅ^2)	β_{xy} (eVÅ^2)	β_{yy} (eVÅ^2)	
-3.48	-0.57	0.80	2.39	
ν_{xx} (eVÅ^2)	ν_{yx} (eVÅ^2)	ν_{xy} (eVÅ^2)	ν_{yy} (eVÅ^2)	χ_y (eVÅ)
-10.90	-11.33	-41.40	-14.80	5.25

2.6 Numerical and mathematical concepts

There are a few mathematical concepts that are presented so far in this text. Equation (2.3.5) expresses the optical conductivity and can be obtained from the Hamiltonian. For some simple systems it can even be solved analytically. However, numerical approaches can be both necessary and beneficial for complicated systems.

One of the most straight-forward methods to solve such integrals, is done by dividing each integral into Riemann sums and iterate through each sum. The value at each point can be approximated with the midpoint rule. In the midpoint rule, the function is estimated at a point $f(\bar{x}_i, \bar{y}_j, \bar{z}_k)$ which is the average of an interval Δx, Δy and Δz. The integrand is assumed to be constant within the volume $\Delta x \cdot \Delta y \cdot \Delta z$. A triple integral on this form can be written as [32]:

$$\lim_{l,m,n \to \infty} \sum_{i=1}^{l} \sum_{j=1}^{m} \sum_{k=1}^{n} f(\bar{x}_i, \bar{y}_j, \bar{z}_k) \Delta x \Delta y \Delta z = \int \int \int_D f(x, y, z) dx \, dy \, dz. \qquad (2.6.1)$$

The number of iterations N used to approximate an integral using the midpoint rule is proportional to the number of steps: $N \propto lmn$. For $l = m = n$ this can be rewritten as $N \propto n^3$.

In solid state physics, analyses involving electron-photon interactions very often include processes that exhibit Dirac-delta like behaviour. An example of this can be seen in equation (2.2.2). To solve this kind of integrals, there are several useful relations that can be utilized, which intuitively can be understood from the mathematical properties of the Dirac delta functions. Some important relations are presented in Table 2. For numerical evaluation, it is necessary to introduce an approximation of the delta function as computers are unable to handle such singularities. A very useful approximation is the Lorentzian form of the delta function $\delta_L(x)$, which is a probability density function whose integral is unity. For this reason, the Lorentzian function is a good approximation for the delta function that conserves most of its distinctive characteristics. It is defined through [33]:

$$\delta_L(x) = \frac{1}{\pi} \frac{\eta}{\eta^2 + x^2}, \qquad (2.6.2)$$

where η is a broadening parameter which is also incorporated in equation (2.3.2). Physically, η represents inelastic scattering effects in the material. In the limit $\eta \to 0$ this function $\delta_L(x)$ becomes equal to the Dirac delta function $\delta(x)$.

Table 2: Useful properties of the Dirac delta function [29]. x_i are the roots of $h(x) = 0$.

1.	$\delta(x) = \delta(-x)$
2.	$\int_{-\infty}^{\infty} \delta(a - x)\delta(b - x)dx = \delta(a - b)$
3.	$f(x)\delta(x - a) = f(a)\delta(x - a)$
4.	$\delta(h(x)) = \sum_i \frac{\delta(x - x_i)}{|h'(x_i)|}$

3 Methods

3.1 Foundation

To begin the analysis of phosphorene, we employ the effective low-energy $\mathbf{k} \cdot \mathbf{p}$ Hamiltonian presented in equation (2.5.1). Writing out the sum, the Hamiltonian can be presented in matrix form as follows:

$$H(k_x, k_y) = \begin{pmatrix} a_1 + b_1 k_x^2 + b_2 k_y^2 & a_2 + c_1 k_x^2 + c_2 k_y^2 + i\chi_y k_y \\ a_2 + c_1 k_x^2 + c_2 k_y^2 - i\chi_y k_y^2 & a_1 + b_1 k_x^2 + b_2 k_y^2 \end{pmatrix}. \tag{3.1.1}$$

Where we have employed the following substitutions:

$$a_1 = u_0 + \alpha_x \mathcal{E}_{xx} + \alpha_y \mathcal{E}_{yy}, \qquad\qquad a_2 = \delta_0 + \mu_x \mathcal{E}_{xx} + \mu_y \mathcal{E}_{yy},$$

$$b_1 = \eta_x + \beta_{xx} \mathcal{E}_{xx} + \beta_{yx} \mathcal{E}_{yy}, \qquad\qquad b_2 = \eta_y + \beta_{xy} \mathcal{E}_{xx} + \beta_{yy} \mathcal{E}_{yy},$$

$$c_1 = \gamma_x + \nu_{xx} \mathcal{E}_{xx} + \nu_{yx} \mathcal{E}_{yy}, \qquad\qquad c_2 = \gamma_y + \nu_{xy} \mathcal{E}_{xx} + \nu_{yy} \mathcal{E}_{yy}. \tag{3.1.2}$$

In this substitution, it is worth noting that all the parameters are ultimately numeric values that can be calculated from the values presented in Table 1 for any given strain. This Hamiltonian is the foundation for the remainder of the analysis: First to obtain the band structure, then to obtain the optical conductivity and permittivity through the Greenwood-Kubo formula.

3.2 Band structure analysis

The energy eigenstates can be derived from the Hamiltonian. These are simply the eigenvalues of equation (3.1.1), which in this case are the two functions:

$$E_c(k_x, k_y) = a_1 + b_1 k_x^2 + b_2 k_y^2 + \sqrt{\left(a_2 + c_1 k_x^2 + c_2 k_y^2\right)^2 + \chi_y^2 k_y^2}, \tag{3.2.1}$$

$$E_v(k_x, k_y) = a_1 + b_1 k_x^2 + b_2 k_y^2 - \sqrt{\left(a_2 + c_1 k_x^2 + c_2 k_y^2\right)^2 + \chi_y^2 k_y^2}. \tag{3.2.2}$$

Here, $E_v(k_x, k_y)$ is the valence band and $E_c(k_x, k_y)$ the conduction band. Thus, this set of equations describes the two bands that most of the low-energy physics is restricted to. There also exists higher and lower bands that are not included in this analysis. Band structures for various strains, both uniaxial and biaxial, were studied from equations (3.2.1) and (3.2.2).

By employing equation (2.2.2) on the conduction band, the Drude weights at various strains can be obtained. Focusing on $D_{xx}(\mu)$, we can rewrite this equation as:

$$D_{xx}(\mu) \propto \int \int \delta\big(h(k_x)\big) \cdot f(k_x)\, dk_x dk_y, \tag{3.2.3}$$

where we have performed the following substitutions:

$$h(k_x) = \mu - E_c\big(k_x, k_y\big),$$
$$h'(k_x) = -\frac{dE_c\big(k_x, k_y\big)}{dk_x},$$
$$f(k_x) = \left(\frac{dE_c\big(k_x, k_y\big)}{dk_x}\right)^2. \tag{3.2.4}$$

Using the fourth relation presented in Table 2, the integral becomes:

$$D_{xx}(\mu) \propto \sum_i \frac{1}{\big|h'\big(k_{x,i}\big)\big|} \int \int_{-\infty}^{\infty} \delta\big(k_x - k_{x,i}\big) \cdot f(k_x)\, dk_x dk_y, \tag{3.2.5}$$

where $k_{x,i}$ are the solutions to $h(k_x) = 0$. The integral above is in fact determined through the second relation in Table 2, which yields the solution to the first integral:

$$D_{xx}(\mu) \propto \int \sum_i \frac{f\big(k_{x,i}\big)}{\big|h'\big(k_{x,i}\big)\big|}\, dk_y. \tag{3.2.6}$$

By reimplementing our original values for the substitutions in equation (3.2.4), the relation between $f(k_x)$ and $h'(k_x)$ becomes useful and the integral is reduced to:

$$D_{xx}(\mu) \propto \int \sum_i \left|\frac{dE_c\big(k_{x,i}, k_y\big)}{dk_x}\right| dk_y, \tag{3.2.7}$$

and similarly for D_{yy} it is:

$$D_{yy}(\mu) \propto \int \sum_i \left|\frac{dE_c\big(k_x, k_{y,i}\big)}{dk_y}\right| dk_x. \tag{3.2.8}$$

If we were to write out the sums and expressions in equations (3.2.7) and (3.2.8), the expressions become very extensive due to the fact that $k_{x,i}$ and $k_{y,i}$ are complicated solutions that are inserted into relatively complicated expressions. Solving the integrals analytically thus becomes very difficult, if not impossible. For this reason, equations (3.2.7) and (3.2.8) were therefore evaluated numerically. The integration was repeated for multiple values of $\mathcal{E}_{xx}$ and $\mathcal{E}_{yy}$.

When solving the final integral, the domain of k_x and k_y needs to be considered. The physical interpretation of equations (3.2.7) and (3.2.8) is that the Drude weight in for instance the x-direction is proportional to the k_x-component of the band curvature along the curve at the intersection $E_c = \mu$, integrated over all possible values for k_y. Thus, the domain of k_x and k_y are the values that lies where the μ-plane intersects the conduction band, which is half an ellipse for each variable. In essence, the Drude weight is determined by how quickly new near-vertically states are unlocked in k_x direction as μ increases. If the conduction band is increasing rapidly at a given energy level, increasing the chemical potential introduces new available energy states rapidly. This is given the fact that electron transitions are predominantly between energy states separated vertically in the band diagram. Even though new energy states are unlocked faster for more horizontal bands, these states are not available for intraband transitions due to large separation in **k**-space.

3.3 Optical conductivity

3.3.1 Obtaining the Green's functions

To calculate the optical conductivity of phosphorene, we need to obtain the spectral functions that appear in the Kubo formula presented in equation (2.3.5). To do this we start by obtaining the inverse Green's function from the Hamiltonian presented in equation (3.1.1), according to their relation in equation (2.3.2). By inverting the result, we get the following Green's function components, where $z = \omega + i\eta$ has been used to represent a complex number with frequency ω and scattering η:

$$G_{11} = -\frac{z + a_1 + b_1 k_x^2 + b_2 k_y^2}{\left(-z + a_1 + b_1 k_x^2 + b_2 k_y^2\right)^2 - \left(a_2 + c_1 k_x^2 + c_2 k_y^2\right)^2 - \chi_y^2 k_y^2},$$

$$G_{12} = \frac{a_2 + c_1 k_x^2 + k_y(c_2 k_y + i\chi_y)}{\left(-z + a_1 + b_1 k_x^2 + b_2 k_y^2\right)^2 - \left(a_2 + c_1 k_x^2 + c_2 k_y^2\right)^2 - \chi_y^2 k_y^2},$$

$$G_{21} = \frac{a_2 + c_1 k_x^2 + k_y(c_2 k_y - i\chi_y)}{\left(-z + a_1 + b_1 k_x^2 + b_2 k_y^2\right)^2 - \left(a_2 + c_1 k_x^2 + c_2 k_y^2\right)^2 - \chi_y^2 k_y^2},$$

$$G_{22} = -\frac{z + a_1 + b_1 k_x^2 + b_2 k_y^2}{\left(-z + a_1 + b_1 k_x^2 + b_2 k_y^2\right)^2 - \left(a_2 + c_1 k_x^2 + c_2 k_y^2\right)^2 - \chi_y^2 k_y^2}. \tag{3.3.1}$$

Here, the subscripts denote the matrix element index of the full Green's function. By inspection, there are several recurring factors in this equation. Thus, we can simplify the Green's function further:

$$G(k_x, k_y, z) = \frac{1}{(z - f_1)^2 - g_1^2} \begin{pmatrix} z - f_1 & f_2 + i\chi_y k_y \\ f_2 - i\chi_y k_y & z - f_1 \end{pmatrix}, \tag{3.3.2}$$

where the following substitutions have been employed:

$$f_1 = a_1 + b_1 k_x^2 + b_2 k_y^2,$$

$$f_2 = a_2 + c_1 k_x^2 + c_2 k_y^2,$$

$$g_1 = \sqrt{f_2^2 + \chi_y^2 k_y^2}. \tag{3.3.3}$$

3.3.2 Obtaining the spectral functions

Next, we need to obtain the spectral function from the Green's function in equation (3.3.2). In its current formulation, it is very difficult to obtain the spectral functions through relation (2.3.6). Therefore, they need to be rewritten so that the shape of the Green's function resembles a solution to a known integral. If we inspect the first and the last term is similar to the of the Green's function, we can write them in the following form:

$$G_{11} = G_{22} = \frac{z - f_1}{(z - f_1 + g_1)(z - f_1 - g_1)}. \tag{3.3.4}$$

Now, we can take notice of the following equality. Here, the right-hand side is simply obtained by writing the left-hand side as two separate terms and then simplifying each term:

$$\frac{(z - f_1 - g_1) + (z - f_1 + g_1)}{(z - f_1 + g_1)(z - f_1 - g_1)} = \frac{1}{z - f_1 + g} + \frac{1}{z - f_1 - g}. \tag{3.3.5}$$

If we calculate the numerator on left-hand side of equation (3.3.5), it becomes $2(z - f)$. Thus, we can see that the right-hand side of equation (3.3.4) can be rewritten as follows:

$$\frac{z - f_1}{(z - f_1 + g_1)(z - f_1 - g_1)} = \frac{1}{2}\left(\frac{1}{z - f_1 + g_1} + \frac{1}{z - f_1 - g_1}\right). \tag{3.3.6}$$

Hence, the diagonal terms of the Green's function can be written as:

$$G_{11} = G_{22} = \frac{1}{2}\left(\frac{1}{z - f_1 + g_1} + \frac{1}{z - f_1 - g_1}\right). \tag{3.3.7}$$

For the remaining terms, we can follow a similar approach where we instead of equation (2.4.7) utilize the following equality:

$$\frac{(z - f_1 - g_1) - (z - f_1 + g_1)}{(z - f_1 + g_1)(z - f_1 - g_1)} = \frac{1}{z - f_1 + g_1} - \frac{1}{z - f_1 - g_1}. \tag{3.3.8}$$

By simplifying the numerator of the left-hand side, we get $-2g_1$ in this case. This means that:

$$\frac{a}{(z - f_1 + g_1)(z - f_1 - g_1)} = \frac{a}{2g_1}\left(\frac{1}{z - f_1 - g_1} - \frac{1}{z - f_1 + g_1}\right). \tag{3.3.9}$$

The remaining Green's function elements can therefore be written on the following form:

$$G_{12} = \frac{f_2 + i\chi_y k_y}{2g_1}\left(\frac{1}{z - f_1 - g_1} - \frac{1}{z - f_1 + g_1}\right), \tag{3.3.10}$$

$$G_{21} = \frac{f_2 - i\chi_y k_y}{2g_1}\left(\frac{1}{z - f_1 - g_1} - \frac{1}{z - f_1 + g_1}\right). \tag{3.3.11}$$

Although this representation might seem slightly more complicated than equation (3.3.2), it makes the process of obtaining the spectral functions easier. In its current form, we can see that the components of the Green's function resembles the solution to the following integral, which is defined through the properties presented in Table 2:

$$\int_{-\infty}^{\infty} \frac{d\omega}{2\pi} \frac{\delta(\omega \pm a)}{z - \omega} = \frac{1}{2\pi(z \pm a)}. \tag{3.3.12}$$

Therefore, if the elements of the spectral function consists of delta functions, the solution to (2.3.6) results in the Green's functions that have been obtained. Hence, the elements of the spectral function are:

$$A_{11} = \pi[\delta(\omega - f_1 + g_1) + \delta(\omega - f_1 - g_1)],$$

$$A_{12} = -\frac{\pi(f_2 + i\chi_y k_y)}{g_1}[\delta(\omega - f_1 + g_1) - \delta(\omega - f_1 - g_1)],$$

$$A_{21} = -\frac{\pi(f_2 - i\chi_y k_y)}{g_1}[\delta(\omega - f_1 + g_1) - \delta(\omega - f_1 - g_1)],$$

$$A_{22} = \pi[\delta(\omega - f_1 + g_1) + \delta(\omega - f_1 - g_1)]. \tag{3.3.13}$$

3.3.3 Insertion into the Kubo formula

The final step in obtaining the integrand for the Kubo formula, is to derive an expression for the current density operators $\hat{J}_x$ and $\hat{J}_y$. This can be done from equation (2.2.3) which yields:

$$\hat{J}_x = \frac{2ek_x}{\hbar}\begin{pmatrix} b_1 & c_1 \\ c_1 & b_1 \end{pmatrix}, \tag{3.3.14}$$

$$\hat{J}_y = \frac{e}{\hbar}\begin{pmatrix} 2b_2 k_y & 2c_2 k_y + i\chi_y \\ 2c_2 k_y - i\chi_y & 2b_2 k_y \end{pmatrix}. \tag{3.3.15}$$

At this point, all that remains is to insert these quantities into the Kubo formula presented in equation (2.3.5), yielding:

$$\text{Re}[\sigma_{\alpha\beta}] = \frac{g_s g_v e^2}{2\pi\hbar\Omega}\int_{-\infty}^{\infty} d\omega [f(\omega - \mu) - f(\omega + \Omega - \mu)] \times \int_{-\infty}^{\infty}\int_{-\infty}^{\infty} dk_y dk_x$$

$$\times \{h_{\alpha\beta,1}[\delta(\omega - f_1 + g_1)\delta(\omega + \Omega - f_1 - g_1)] + h_{\alpha\beta,2}[\delta(\omega - f_1 - g_1)\delta(\omega + \Omega - f_1 + g_1)]$$

$$+ h_{\alpha\beta,3}[\delta(\omega - f_1 + g_1)\delta(\omega + \Omega - f_1 + g_1)] + h_{\alpha\beta,4}[\delta(\omega - f_1 - g_1)\delta(\omega + \Omega - f_1 - g_1)]\},$$

$$\tag{3.3.16}$$

where $h_{\alpha\beta,i}$ for each material direction are presented in Table 3.

From equation (3.3.16) along the expressions presented in Table 3, it is possible to make some general remarks about the integral. First it can be seen that the functions f_1, f_2 and g_1 are all functions of k_x^2 and k_y^2, which in turn makes them even functions of these variables. Hence, it follows that all the delta functions in equation (3.3.16) are even with respect to momentum in the x- and y-directions. In fact, it can be seen that the symmetry of the **k**-integrals rely entirely on the symmetry of $h_{\alpha\beta,i}$. Going through each expression in Table 3, the integrals in the x- and y-direction are even while the integrals in the diagonal xy- and yx-directions are odd. Consequently, the conductivities σ_{xy} and σ_{yx} are strictly zero and the integration limits can be adjusted for σ_{xx} and σ_{yy}. If we additionally insert $g_s = 2$ and $g_v = 1$ for phosphorene [34], equation (3.3.16) becomes:

$$\text{Re}[\sigma_{\alpha\alpha}] = \frac{4e^2}{\pi\hbar\Omega}\int_{-\infty}^{\infty} d\omega [f(\omega - \mu) - f(\omega + \Omega - \mu)] \times \int_{0}^{\infty}\int_{0}^{\infty} dk_y dk_x$$

$$\times \{h_{\alpha\alpha,1}[\delta(\omega - f_1 + g_1)\delta(\omega + \Omega - f_1 - g_1)] + h_{\alpha\alpha,2}[\delta(\omega - f_1 - g_1)\delta(\omega + \Omega - f_1 + g_1)]$$

$$+ h_{\alpha\alpha,3}[\delta(\omega - f_1 + g_1)\delta(\omega + \Omega - f_1 + g_1)] + h_{\alpha\alpha,4}[\delta(\omega - f_1 - g_1)\delta(\omega + \Omega - f_1 - g_1)]\},$$

$$\tag{3.3.17}$$

where the extra factor of 4 comes from the change of integration limits in k_x- and k_y-direction.

Table 3: Definitions of the $h_{\alpha\beta,i}$ substitutions in equation (3.3.16).

x-direction	$h_{xx,1} = h_{xx,2} =$	$4k_x^2\left(\dfrac{c_1^2\chi_y^2 k_y^2}{g_1^2}\right)$
	$h_{xx,3} =$	$4k_x^2\left(b_1^2 + \dfrac{c_1^2 f_2^2}{g_1^2} - \dfrac{2b_1 c_1 f_2}{g_1}\right)$
	$h_{xx,4} =$	$4k_x^2\left(b_1^2 + \dfrac{c_1^2 f_2^2}{g_1^2} + \dfrac{2b_1 c_1 f_2}{g_1}\right)$
xy-direction	$h_{xy,1} = h_{xy,2} =$	$\dfrac{2c_1\chi_y^2 k_x k_y}{g_1^2}\left(2c_2 k_y^2 - f_2\right)$
	$h_{xy,3} =$	$\dfrac{2k_x k_y}{g_1^2}(c_1 f_2 - b_1 g_1)\left(2c_2 f_2 - 2b_2 g_1 + \chi_y^2\right)$
	$h_{xy,4} =$	$\dfrac{2k_x k_y}{g_1^2}(c_1 f_2 + b_1 g_1)\left(2c_2 f_2 + 2b_2 g_1 + \chi_y^2\right)$
yx-direction	$h_{yx,1} = h_{yx,2} =$	$\dfrac{2c_1\chi_y^2 k_x k_y}{g_1^2}\left(2c_2 k_2^2 - f_2\right)$
	$h_{yx,3} =$	$\dfrac{2k_x k_y}{g_1^2}(c_1 f_2 - b_1 g_1)\left(2c_2 f_2 - 2b_2 g_1 + \chi_y^2\right)$
	$h_{yx,4} =$	$\dfrac{2k_x k_y}{g_1^2}(c_1 f_2 + b_1 g_1)\left(2c_2 f_2 + 2b_2 g_1 + \chi_y^2\right)$
y-direction	$h_{yy,1} = h_{yy,2} =$	$\dfrac{\left(-2c_2 k_y^2 + f_2\right)^2 \chi_y^2}{g_1^2}$
	$h_{yy,3} =$	$k_y^2\left(4b_2^2 + \dfrac{\left(2c_2 f_2 + \chi_y^2\right)^2}{g_1^2} - \dfrac{4b_2\left(2c_2 f_2 + \chi_y^2\right)}{g_1}\right)$
	$h_{yy,4} =$	$k_y^2\left(4b_2^2 + \dfrac{\left(2c_2 f_2 + \chi_y^2\right)^2}{g_1^2} - \dfrac{4b_2\left(2c_2 f_2 + \chi_y^2\right)}{g_1}\right)$

3.3.4 Analytical approach

One can approach Equation (3.3.17) analytically, and the two **k**-integrals are solved in this section. First, the **k**-integrals can be split into four terms, which all follow the same pattern. We can represent the first k_x-integral as a sum of independent integrals:

$$\sum_{i=1}^{4} \int_0^\infty h_{\alpha\alpha,i}\delta(m_{x,i,1})\delta(m_{x,i,2})dk_x, \tag{3.3.18}$$

where $m_{x,i,n}$ are substitutions for the functions within the delta functions in (3.3.17) and are functions of k_α. Here, the indices α and x denotes the crystallographic directions as before. The new parameters $i \in \{1,2,3,4\}$ and $n \in \{1,2\}$ denotes the index of each term and delta function, respectively. As an example, $m_{x,1,2}$ is therefore the function inside the second delta function, within the first term of equation (3.3.17), namely $\omega + \Omega - f_1 - g_1$. This can also be understood by inspecting equation (3.3.18) carefully. Writing the integral on this form already makes it easier to solve, and the next step is to write the delta functions in terms of k_x directly rather than a function of it. Using Table 2 we get:

$$\sum_{i=1}^{4} \int_0^\infty h_{\alpha\alpha,i}\left[\sum_j \frac{\delta(k_x - k_{x,i,1,j})}{|m'_{x,i,1}(k_{x,i,1,j})|} \times \sum_j \frac{\delta(k_x - k_{x,i,2,j})}{|m'_{x,i,2}(k_{x,i,2,j})|}\right] dk_x, \tag{3.3.19}$$

where $k_{x,i,n,j}$ denotes all the roots of $m_{x,i,n}$, and j is the index of them. Next, we wish to get the expression on the form:

$$\sum_i \int f_i(x)\delta(x - x_{1,i})\delta(x - x_{2,i})dx, \tag{3.3.20}$$

as this integral is defined in Table 2. This can be done by utilizing that $h_{\alpha\alpha,i} = \sqrt{h_{\alpha\alpha,i}}^2$ and the fact that the denominators in equation (3.3.19) are independent of k_x. Taking this into consideration, we can rewrite equation (3.3.19) so that it becomes:

$$\sum_{i=1}^{4} \int_0^\infty \left[\sum_j \frac{\sqrt{h_{\alpha\alpha,i}}\delta(k_x - k_{x,i,1,j})}{|m'_{x,i,1}(k_{x,i,1,j})|} \times \sum_j \frac{\sqrt{h_{\alpha\alpha,i}}\delta(k_x - k_{x,i,2,j})}{|m'_{x,i,2}(k_{x,i,2,j})|}\right] dk_x. \tag{3.3.21}$$

This is the furthest that it is possible to go without making specific remarks about the expressions themselves. The integral in equation (3.3.21) is defined through equation (3.3.20) so long as each $m'_{x,i,n}$ has no more than two roots. By studying the roots of all the expressions, they have four each. However, it can be noted that the solutions come in sets of two with one negative and one positive variant. Since the solutions are inserted into expressions dependent of k_x^2, there are thus only two unique solutions for each $m'_{x,i,n}$, i.e., $j \in \{1,2\}$.

By expanding the product of the two summations in equation (3.3.21), each term is on the form of equation (3.3.20) and the solution to the k_x-integral becomes:

$$\sum_{i=1}^{4} d_{x,i,1,1} d_{x,i,2,1} \delta(k_{x,i,1,1} - k_{x,i,2,1}) + d_{x,i,1,2} d_{x,i,2,1} \delta(k_{x,i,1,2} - k_{x,i,2,1})$$
$$+ d_{x,i,1,1} d_{x,i,2,2} \delta(k_{x,i,1,1} - k_{x,i,2,2}) + d_{x,i,1,2} d_{x,i,2,2} \delta(k_{x,i,1,2} - k_{x,i,2,2}), \qquad (3.3.22)$$

where we have employed the substitution:

$$d_{x,i,n,j} = \frac{\sqrt{h_{\alpha\alpha,i}(k_{x,i,n,j})}}{\left| m'_{x,i,n}(k_{x,i,n,j}) \right|}. \qquad (3.3.23)$$

Solving the k_y-integral can be done in a very similar fashion as the k_x-integral. To show this we can rewrite equation (3.3.22) on the following form, now including the k_y integral notation:

$$\sum_{i=1}^{4} \sum_{l=1}^{4} \int_0^{\infty} H_{y,i,l} \delta(m_{y,i,l}) dk_y, \qquad (3.3.24)$$

where the substitutions $H_{y,i,l}$ and $m_{y,i,l}$ are defined as:

$$H_{y,i,1} = d_{x,i,1,1} d_{x,i,2,1}, \qquad m_{y,i,1} = k_{x,i,1,1} - k_{x,i,2,1},$$

$$H_{y,i,2} = d_{x,i,1,2} d_{x,i,2,1}, \qquad m_{y,i,2} = k_{x,i,1,2} - k_{x,i,2,1},$$

$$H_{y,i,3} = d_{x,i,1,1} d_{x,i,2,2}, \qquad m_{y,i,3} = k_{x,i,1,1} - k_{x,i,2,2},$$

$$H_{y,i,4} = d_{x,i,1,2} d_{x,i,2,2}, \qquad m_{y,i,4} = k_{x,i,1,2} - k_{x,i,2,2}. \qquad (3.3.25)$$

Here, the two indices n and j have been merged into a single index l. This is not strictly necessary, but it allows us to solve the k_y-integrals in the same manner as the k_x-integrals and reduces the number of indices needed forwards. Now, the new parameter l is an index for the terms of equation (3.3.24) just like i denotes the terms of equation (3.3.17). This makes equation (3.3.24) essentially the same as equation (3.3.18) in terms of integration, apart from the latter having a single delta function. Hence we get:

$$\sum_{i=1}^{4} \sum_{l=1}^{4} \int_0^{\infty} \sum_{j} \frac{H_{y,i,l} \delta(k_y - k_{y,i,l,j})}{\left| m'_{y,i,l}(k_{y,i,l,j}) \right|} dk_y, \qquad (3.3.26)$$

which for the two unique roots of $m_{y,i,l}$ have the solution:

$$\sum_{i=1}^{4} \sum_{l=1}^{4} \sum_{j=1}^{2} \frac{H_{y,i,l}(k_{y,i,l,j})}{|m'_{y,i,l}(k_{y,i,l,j})|}. \tag{3.3.27}$$

Equation (3.3.27) is the full solution to the **k**-integrals, where the direction-dependency is encapsulated in $h_{\alpha\alpha,i}$, contained in $H_{y,i,l}$. The remaining parameters are independent of direction. Rewriting the derived Kubo formula from equation (3.3.17), we get the optical conductivity:

$$\mathrm{Re}[\sigma_{\alpha\alpha}] = \frac{4e^2}{\pi\hbar\Omega} \int_{-\infty}^{\infty} d\omega [f(\omega - \mu) - f(\omega + \Omega - \mu)]$$
$$\times \sum_{i=1}^{4} \sum_{l=1}^{4} \sum_{j=1}^{2} \frac{H_{y,i,l}(k_{y,i,l,j})}{|m'_{y,i,l}(k_{y,i,l,j})|}. \tag{3.3.28}$$

At zero temperature, this can be simplified even further. By inspecting the Fermi function at absolute zero, it can be seen that it becomes a square function with the value of unity inside the region $\omega \in [\mu - \Omega, \mu]$ and zero elsewhere. In essence:

$$f(\omega - \mu) - f(\omega + \Omega - \mu) = 1, \qquad \omega \in [\mu - \Omega, \mu], \tag{3.3.29}$$

and zero elsewhere. Thus, we can account for this with the integration limits to obtain a simplification of equation (3.3.28) at $T = 0$K:

$$\mathrm{Re}[\sigma_{\alpha\alpha}] = \frac{4e^2}{\pi\hbar\Omega} \int_{\mu-\Omega}^{\mu} \sum_{i=1}^{4} \sum_{j=1}^{4} \sum_{n=1}^{2} \frac{H_{y,i,j}(k_{y,i,j,n})}{|m'_{y,i,j,n}(k_{y,i,j,n})|} d\omega. \tag{3.3.30}$$

The last step regarding the Fermi function is described in greater detail in the next section.

This is the furthest that the Kubo formula will be analysed analytically, since solving the final ω-integral is highly challenging if not impossible. Writing out the substitutions in equation (3.3.30) results in a very large expression, considering that $k_{y,i,l,j}$ and $k_{x,i,n,j}$ are complicated expressions inserted into the already complicated expressions $H_{y,i,l}$, $d_{x,i,n,j}$ and $m'_{\alpha,i,n/l}$.

3.3.5 Numerical approach

The Kubo formula presented in equation (3.3.17) was solved numerically using the concepts explained in equation (2.6.1). However, in order to solve the integration numerically a few considerations in terms of integral limits and the integrand needs to be done.

Firstly, the limits of the **k**-integrals must be limited to a finite region for the integral to be solvable numerically. For this, the physical foundation for the system can be considered. Since the Hamiltonian was derived using the method of invariants, the Hamiltonian is a good approximation to the system within the low-energy region in **k**-space. Additionally, the method

of invariants is built upon the principle of symmetry between the Brillouin zones of the material. In other words, the physics of the problem using this model is entirely confined within the region $\mathbf{k} \in [-2\pi, 2\pi]$. By additionally considering that the integrand is even in $\mathbf{k}$-space, the $\mathbf{k}$-integrals can be confined to the region $\mathbf{k} \in [0, 2\pi]$.

Next, the limits of the ω-integral needs to be determined. The zero-temperature limits were presented in equation (3.3.30) as a Heaviside-Θ square function, but at non-zero temperatures this definition needs to be expanded. Figure 6 highlights why the Heaviside step function approximation used in (3.3.30) is inaccurate for large temperatures, since the whole expression will be pulled towards zero within the region if the tail of each Fermi function overlaps. Multiplied with another non-constant function, the Heaviside step function approximation will overestimate the integrand within the region and underestimate it outside. This effect is clearly seen for temperatures at T3=1.0K and higher in Figure 6. The effect is greater at lower photon energies $\hbar\Omega$, as seen by comparing Figure 6 a) and 6 b). Nevertheless, it is worth noting that Figure 6 has energies in the order of meV which is comparable to the energies in zero-gap materials. For semiconductors with bandgaps in the order of eVs, temperatures need to be roughly 10^3 times larger to see the same effects as in Figure 6.

To include the slope of the edges for the Fermi function, we can write the integration limits as:

$$\int_{-\infty}^{\infty} \frac{d\omega}{2\pi} f(\omega - \mu) - f(\omega + \Omega - \mu) \rightarrow \int_{\mu-\Omega-|\delta_T|}^{\mu+|\delta_T|} \frac{d\omega}{2\pi} f(\omega - \mu) - f(\omega + \Omega - \mu), \quad (3.3.31)$$

where δ_T is a temperature-dependent parameter to account for the broadening of each of the edges in the Fermi functions. Since the maximum of the Fermi distribution is unity, the δ_T parameter can be derived in terms of an acceptable tolerance σ_f as follows:

$$\frac{1}{e^{\gamma|\delta_T|} + 1} \geq \sigma_f$$

$$|\delta_T| \leq k_B T \cdot \ln\left(\frac{1}{\sigma_f} - 1\right). \quad (3.3.32)$$

Here, $|\delta_T|$ ensures that all values before $f(x - |\delta_T|)$ and beyond $f(x + |\delta_T|)$ and are smaller than the tolerance ratio σ_f. For instance, if the tolerance is $\sigma_f = 0.01$ it means that all values beyond $f(x + |\delta_T|)$ are smaller than 0.01.

In summary, the Kubo formula adjusted for numerical calculations and physical approximations can be rewritten as:

$$\text{Re}[\sigma_{\alpha\alpha}] = \frac{4e^2}{\pi\hbar\Omega} \int_{\mu-\Omega-|\delta_T|}^{\mu+|\delta_T|} d\omega [f(\omega - \mu) - f(\omega + \Omega - \mu)] \times \int_0^{2\pi} \int_0^{2\pi} dk_y dk_x$$

$$\times \{h_{\alpha\alpha,1}[\delta_L(\omega - f_1 + g_1)\delta_L(\omega + \Omega - f_1 - g_1)] + h_{\alpha\alpha,2}[\delta_L(\omega - f_1 - g_1)\delta_L(\omega + \Omega - f_1 + g_1)]$$

$$+ h_{\alpha\alpha,3}[\delta_L(\omega - f_1 + g_1)\delta_L(\omega + \Omega - f_1 + g_1)] + h_{\alpha\alpha,4}[\delta_L(\omega - f_1 - g_1)\delta_L(\omega + \Omega - f_1 - g_1)]\}.$$
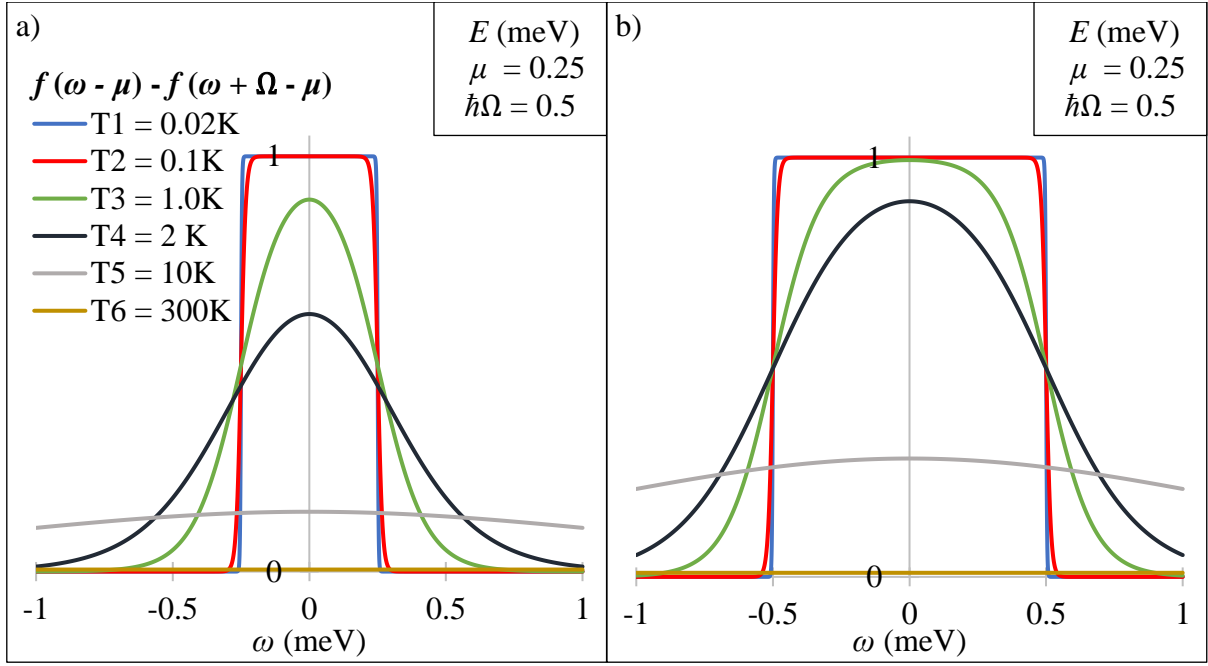
$$(3.3.33)$$

Figure 6: Fermi-Dirac distribution functions at temperatures ranging from T=0.02K to T=300K, for various values of μ and Ω in the energy regime meV.

Equation (3.3.33) can be rewritten in terms of a Riemann sum can for a given photon energy $\hbar\Omega_m$ as:

$$\text{Re}\left[\sigma_{\alpha\beta}(\Omega_m)\right] = \frac{4e^2}{\pi\hbar\Omega_m} \sum_{i=1}^{n}\sum_{j=1}^{n}\sum_{l=1}^{n} \chi\left(\overline{\omega}_i, \overline{k}_{y,j}, \overline{k}_{x,l}\right)\Delta\omega(\Omega)(\Delta\mathbf{k})^2, \qquad (3.3.34)$$

where n is the number of integration steps, $\chi\left(\overline{\omega}_i, \overline{k}_{y,j}, \overline{k}_{x,l}\right)$ represents the integrand of equation (3.3.33). The parameters $\overline{\omega}_i$, $\overline{k}_{y,j}$ and $\overline{k}_{x,l}$ are the midpoints of the integration cubes of volume $\Delta\omega(\Omega)(\Delta\mathbf{k})^2$ defined explicitly in equation (3.3.37) and (3.3.38). These step sizes are defined as:

$$\Delta\omega(\Omega) = \frac{\Omega + 2|\delta_T|}{n}, \qquad (3.3.35)$$

$$\Delta k = \frac{2\pi}{n}. \qquad (3.3.36)$$

Thus, n should be scaled such that $\Delta\mathbf{k} \ll \eta$ to capture all the features of the integrand. Additionally, $\Delta(\omega)$ should be significantly smaller than $|\delta_T|$ at larger temperatures, where the Heaviside Θ is no longer a good approximation. The midpoints are defined as:

$$\overline{\omega}_i = (\mu - \Omega_m - |\delta_T|) + \left(i - \frac{1}{2}\right)\Delta\omega(\Omega_m), \qquad (3.3.37)$$

$$\overline{k}_j = \left(j - \frac{1}{2}\right)\Delta k_y. \qquad (3.3.38)$$

Since all the steps in equation (3.3.34) are independent of one another, it was implemented for both central processing unit (CPU) calculation and graphical processing unit (GPU) computation, to select the favourable method. Equation (3.3.30) was also attempted to be solved numerically in similar fashion, though unsuccessfully. Due to the complexity of the analytical expression itself, the computational time to calculate function values made the equation (3.3.30) unfavourable compared to (3.3.33).

To properly validate the integration of the Kubo formula, the integrals were also evaluated using a global adaptive quadrature method which is generally considered to be more stable for bad-behaved integrands. This method was only used to validate the integrals and was not used to produce any of the results presented in this thesis, because the midpoint rule was significantly easier to optimize for a triple integral and thus converged faster in this case. In terms of optimization, it is worth noting that the $\mathbf{k}$ integrals can be solved for multiple values of μ and temperature simultaneously since they are independent of these parameters. In this thesis, this was done for the midpoint-rule.

Once the result for the real part of $\sigma_{\alpha\alpha}$ was calculated, the imaginary part was calculated using the Kramer-Kronig relations presented in equation (2.4.8). The Kramer-Kronig relation was solved numerically in the same manner as the Kubo formula presented in this chapter, excluding a small symmetric region around the point $\overline{\omega}_i{}^2 = \Omega_m^2$ which is a singularity. The upper limit of the integral was set to the maximum value of the set Ω_m.

Next, the Drude weight was calculated from the real part of the optical conductivity. This was done by integrating the Ω near zero response of the optical conductivity for 51 different values of μ between zero and two electron volts. Finally, after calculating both the real and imaginary part of the optical conductivity, the permittivity was calculated using (2.4.1).

4 Results and discussion

4.1 Band structure analysis

4.1.1 Basic properties

The conduction and valence bands derived from the low-energy effective Hamiltonian is presented in equations (3.2.1) and (3.2.2), respectively. With no strain, the resulting band structure around the Γ-point is plotted as a function of k_x and k_y in Figure 7. In this figure, the orange uppermost surface is the conduction band and can be seen to have a strictly positive curvature. The valence band is represented by the lower blue surface and has a strictly negative curvature. The curvature of both bands can also be seen to be greater in the k_y-direction compared to the k_x-direction, and hence the bands are anisotropic in **k**-space. It can also be seen that phosphorene has a direct bandgap at the Γ-point, which for zero strain resides at 1.52 eV. The bandgap can be more easily extracted from Figure 8.
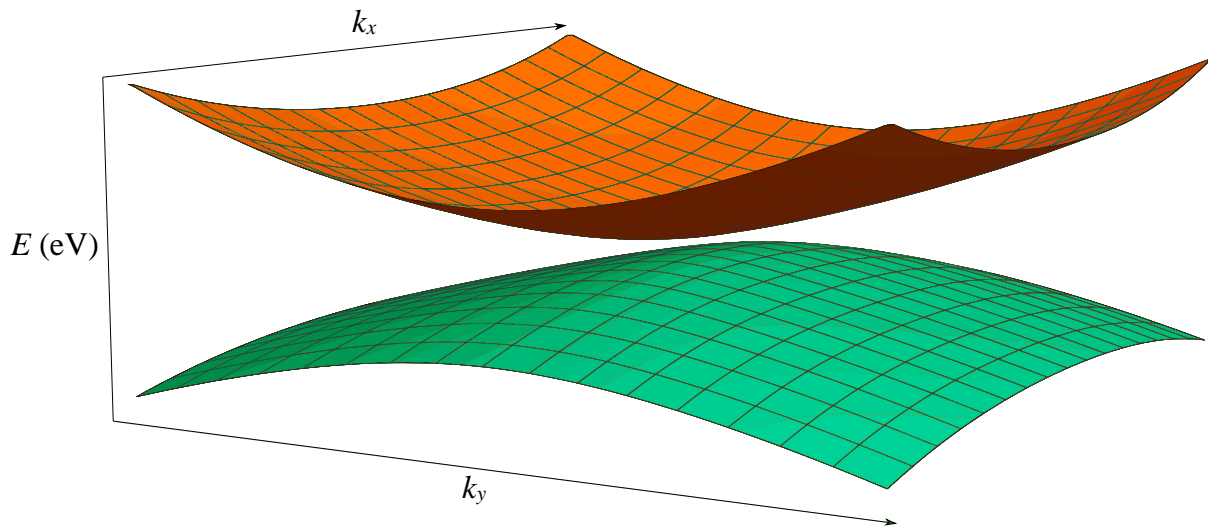

Figure 7: Band structure of phosphorene as a function of k_x and k_y. The orange uppermost surface shows the conduction band, the cyan lower band shows the valence band.

The main morphological features of the bands shown in Figure 7 is preserved for different values of μ and most values of strain, and it can therefore be more informative to plot the bands with respect to k_x and k_y separately. Plotting the band structure for the same values as in Figure 7 separately, i.e., for zero strain at $\mu = 0$ eV, results in the plot shown in Figure 8.

The value of the band gap is more visible in this picture. If we compare Figure 8 to Figure 4, it is apparent that intraband transitions are impossible in the conduction band at $\mu = 0$ as it resides below the bottom of the conduction band. Furthermore with $\mu = 0$ eV, all the states below this energy are in fact filled which also disallows intraband transitions altogether. It is therefore only at energies of μ greater than the energy at the bottom of the conduction band that we expect intraband transitions. An example of this is shown with the green line at $\mu = 0.6$ eV in Figure 8.
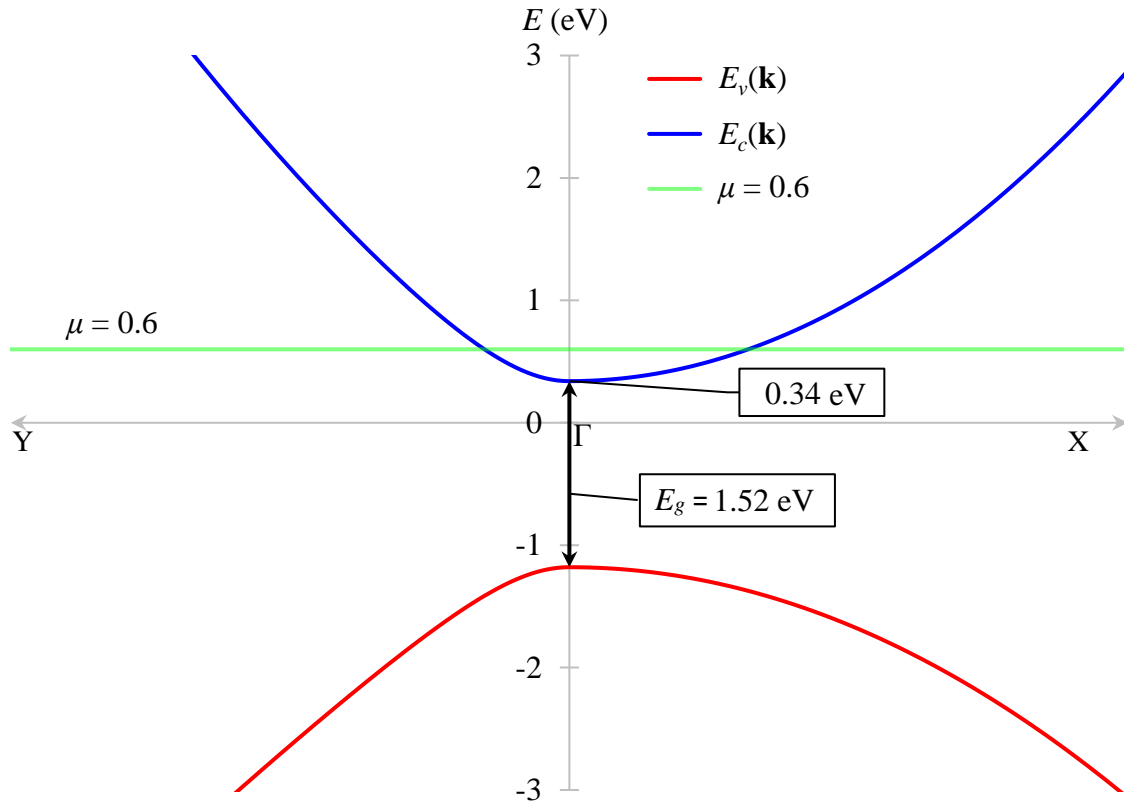
Figure 8: Band structure of phosphorene as a function of **k** near the Γ-point, showing k_x (X) towards the right and k_y (Y) towards the left. An example value of the chemical potentials is shown as a green line for $\mu = 0.6$ eV.

By looking at the band structures in Figure 7 and Figure 8, they resemble that of a semiconductor. It is therefore natural to expect direct-bandgap semiconductor behaviour for the conductivity and permittivity with zero strain and low chemical potentials. The more detailed study of the semiconductor behaviour can be shown by plotting the Drude weights, which were obtained from the bands through equation (3.2.7) and (3.2.8). The Drude weights in the x- and y-directions is shown in Figure 9 a) and 9 b), respectively. The onset of the Drude conductivity emerges when the chemical potential μ reaches the bottom of the conduction band. This is highlighted by the black dotted vertical line, that denotes the energy at the bottom of the conduction band. Values of the chemical potential higher than $\mu = 2$ eV is considered to be outside the low-energy scope of this study.

Figure 9 shows semiconductor-behaviour at low chemical potentials, because the metallic Drude response is only apparent when there are electrons with enough energy to reside in the conduction band. This happens just as the energy of μ is greater than the bottom of the conduction band. As the chemical potential μ increases further into the conduction band, phosphorene can be seen to become more metallic in its conductivity characteristics.
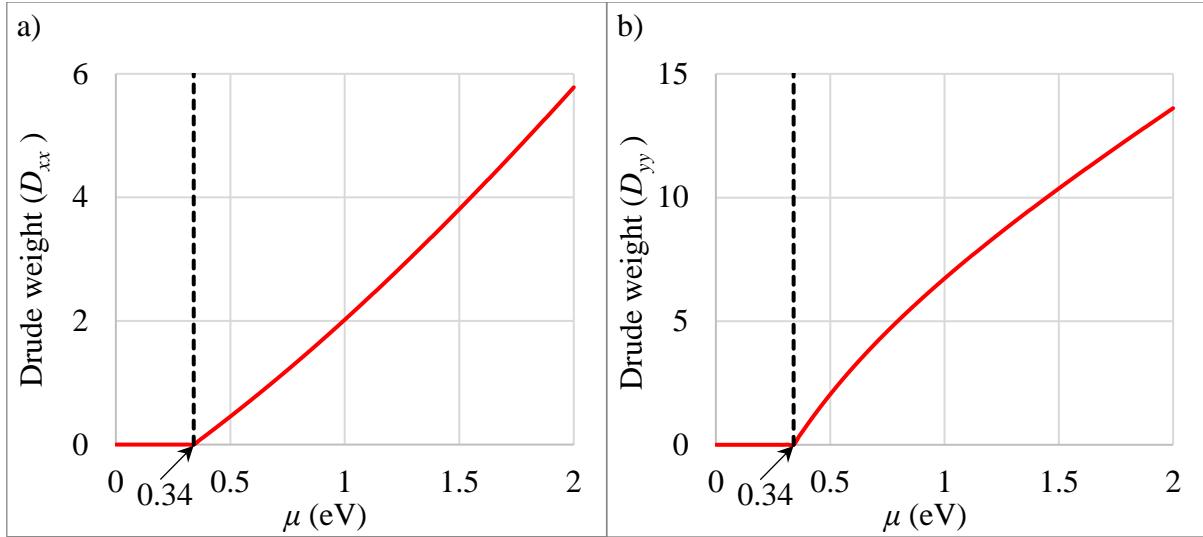
Figure 9: Drude weights for phosphorene in a) the x-direction and b) the y-direction, obtained from the band structure presented in equation (3.2.1) and (3.2.2) shown in Figure 8. The energy at the bottom of the conduction band is highlighted by the black dotted vertical line.

However, it is important to notice that even though there are electrons in the conduction band at high μ-values, the electrons are not conductive in the same sense as in metals. At zero temperature, all states below μ are still occupied by electrons and they require additional energy to become conductive. In metals on the other hand, the overlap between the conduction band and valence band leads to more available states than there are electrons at the same energy. Thus, there is a fundamental difference between the conductivity that appears at high values of μ and conductivity in metals, even though the electron transport in either case is accurately described by the Drude model.

4.1.2 Effect of strain on the band structure

Applying strain to phosphorene changes the band structure significantly. The effect of strain is incorporated in our model as the $\mathcal{E}_{\alpha\beta}$ parameter introduced in equation (2.5.1), that appears in the a_i, b_i, c_i substitutions defined in equation (3.1.2). This thesis focuses on in-plane strain between -10% and 10% to stay within the valid range of this low-energy model.

The band structures for phosphorene subjected to two different strains are shown in Figure 10, namely for a biaxial strain $\mathcal{E}_{xy}$ of -10% and 10% respectively. If we compare the bands in Figure 8 and Figure 10 a) and 10 b), it is apparent that the bandgap of black phosphorous can be strain-engineered. By applying positive (tensile) strain, phosphorene behaves more like an insulator as the bandgap gets larger, and by applying negative (compressive) strain the material behaves more like a metal as the gap closes. In fact, for a biaxial strain of -10% it can be seen that the conduction band is driven below the Fermi level $\mu = E_F = 0$, meaning that charges are present in the conduction band even at $\mu = 0$ eV. For negative strains of this magnitude, it can therefore be expected that the Drude weight is non-zero even when the chemical potential is zero.
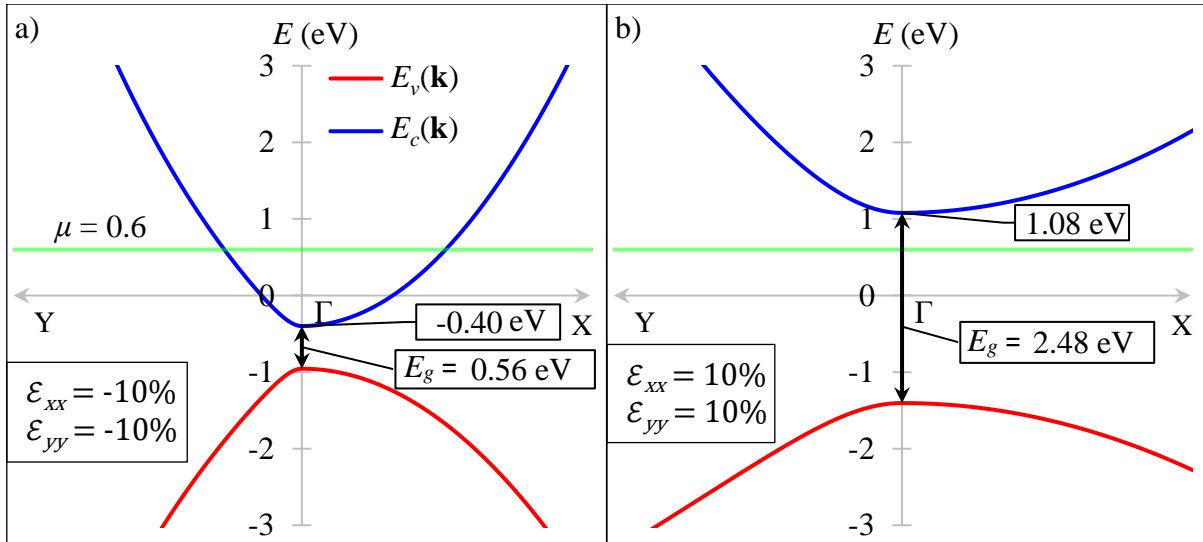
Figure 10: The band structure of phosphorene for a) -10% and b) 10% biaxial strain with respect to k_x towards the right and k_y towards the left.

The effect of strain on the Drude weight can be studied in greater detail by plotting them as a function of μ as done previously. Figure 11 shows exactly this, where the Drude weights are plotted as functions of μ for the strains -10%, 0% and 10%. These are the same strain values used to create the band structures in Figure 8 and Figure 10. From these we can see that the Drude weights are strictly zero for μ below the bottom of the conduction band, and that it has a sudden onset just as it reaches that minimum energy. For the system subjected to -10% strain, the Drude weight is therefore apparent even at $\mu = 0$.
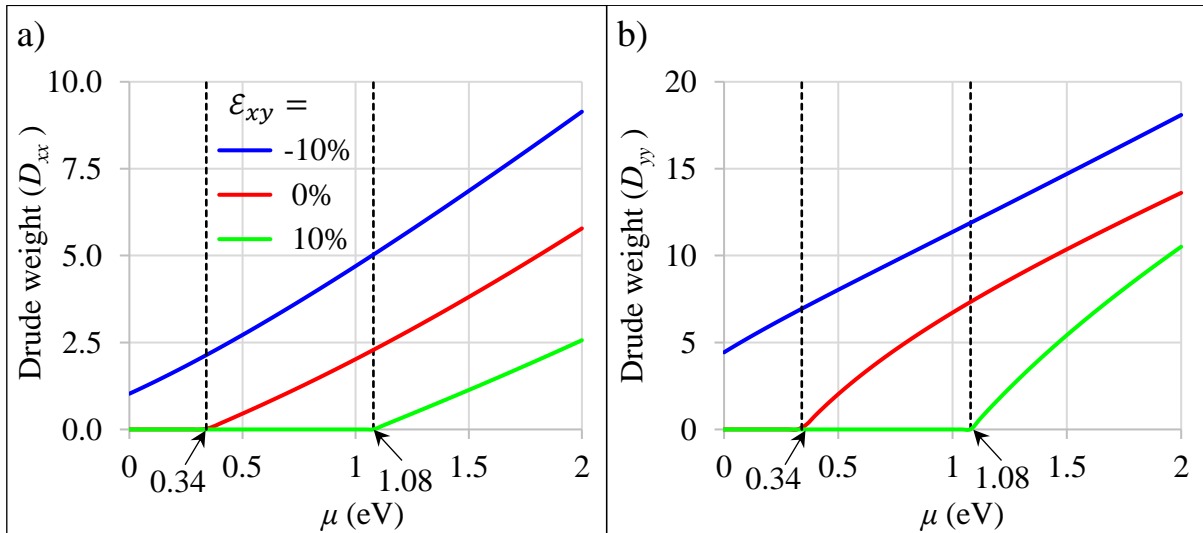

Figure 11: Strain-dependent Drude weights for phosphorene subjected to -10%, 0% and 10% biaxial strain $\mathcal{E}_{xy}$, in a) the x-direction and b) the y-direction obtained from the band structure.

The results in this section so far can be summarized neatly in Figure 12 which shows how the bandgap varies as a function of biaxial strain. Additionally, the bottom of the conduction band E_c^{Min} and top of the valence band E_v^{Max} is also plotted to give some idea of how each band responds to external strain. E_c^{Min} shows at which energy levels of the chemical potential that Drude conductivity is expected to appear.
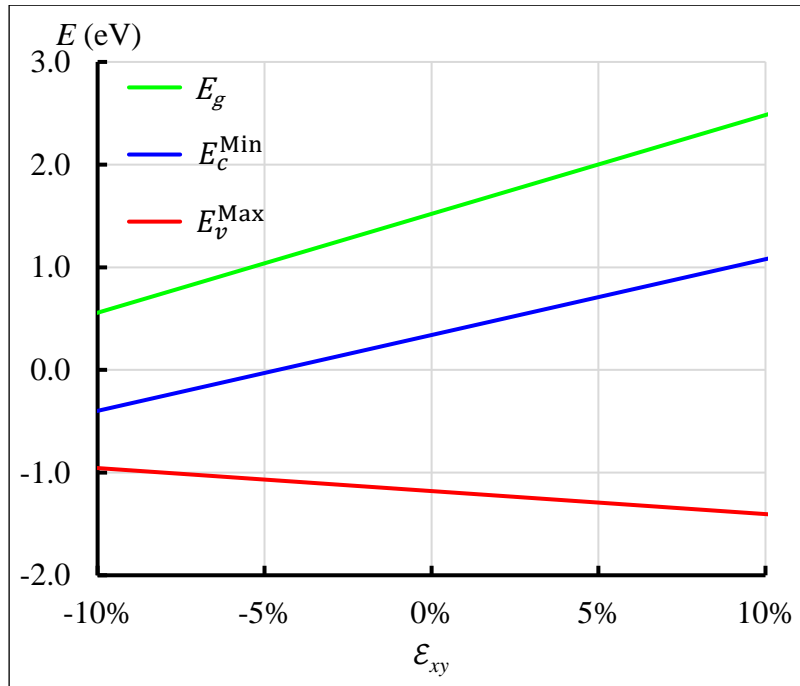
Figure 12: Diagram of the bandgap E_g (green), the bottom of the conduction band E_c^{Min} (blue) and the top of the valence band E_v^{Max} (red) of phosphorene as a function of biaxial strain ε_{xy}, from -10% to 10%.
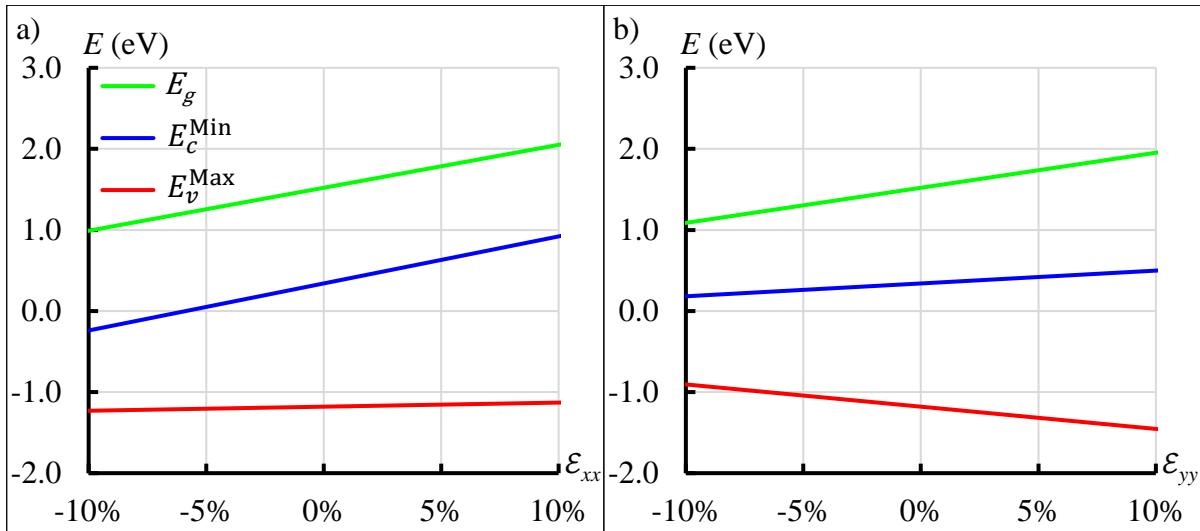

Figure 13: Diagrams showing the effect of uniaxial strain on the band structure. The bandgap (green), the bottom of the conduction band (blue) and the top of the valence band (red) are plotted as functions of a) ε_{xx} and b) ε_{yy}.

The same analysis was done by applying uniaxial strain, and the effects were quite similar to the application of biaxial strain. Studying the overall shape of the bands upon applying uniaxial strain showed that the bands were very similar to the case of zero strain shown in Figure 8. Hence, the effect of uniaxial strain is well summarized by Figure 13.

The Drude weights for -10% and 10% were also calculated for uniaxial strain and is shown in Figure 14. Here, it can be seen that the Drude response is very similar to the case with biaxial strain presented in Figure 11 for strain applied in the x-direction. However, the Drude weight seems to be far less effected by strain applied in the y-direction. This can be understood from Figure 13, where strain in the x-direction primarily affects the conduction band while strain in the y-direction primarily effects the valence band. Thus, the effect on the bandgap is quite similar in each direction while the Drude weight is highly anisotropic with regards to the direction of strain.
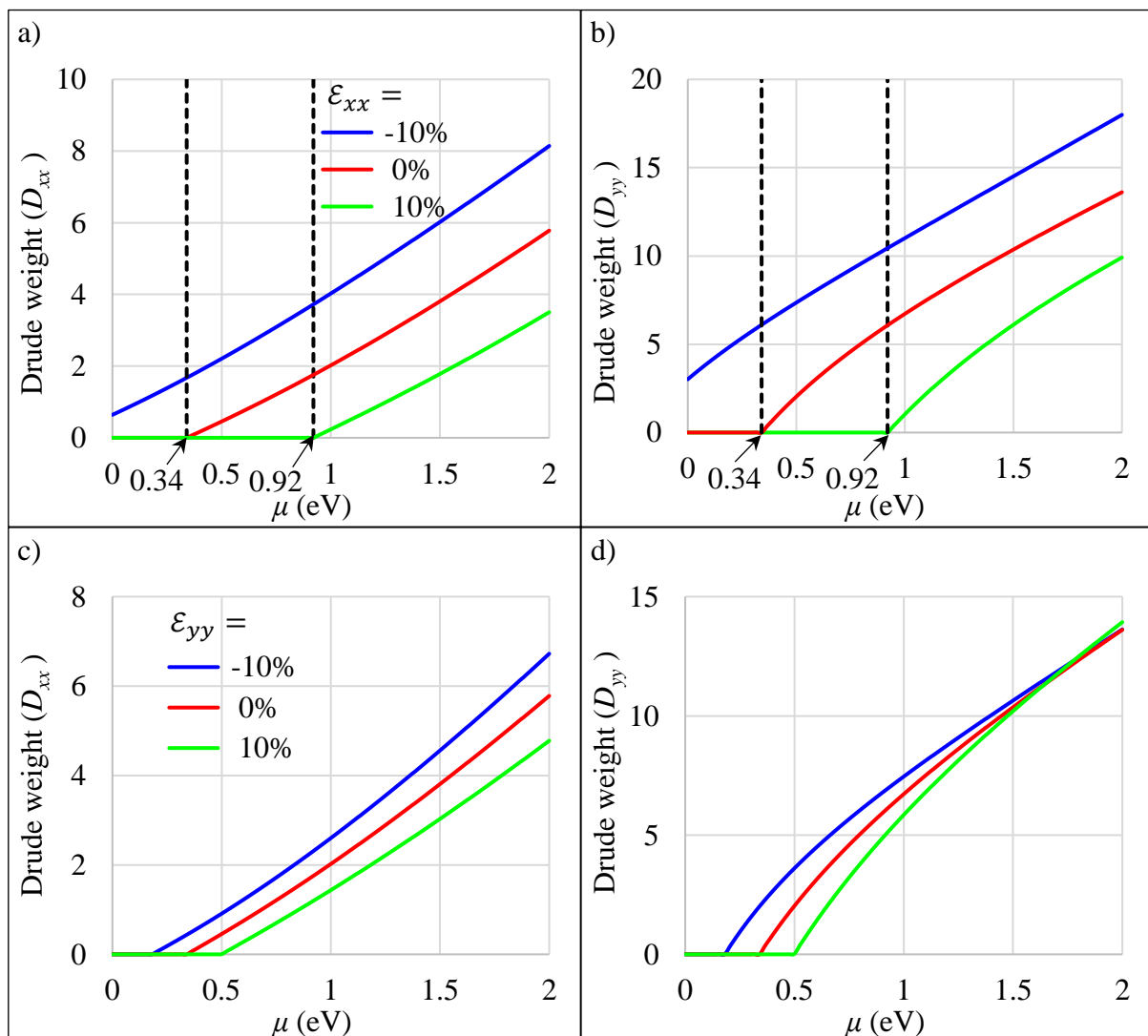

Figure 14: Drude weights for uniaxial strains ranging from -10% to 10%, for strain in a) and b) the x-direction and c) and d) the y-direction. The figures a) and c) shows the Drude weight in the x-direction and b) and d) the y-direction.

4.2 Dielectric response

In this section, the calculations for dielectric response are presented. This includes the optical conductivity calculated from the Kubo formula, as well as the Drude and permittivity response functions obtained from the optical conductivity.

The previous chapter that presented the band structure analysis, already gives a solid foundation of what to expect from the dielectric response, based on the theory presented in section 2.3. According to the theory, we expect no intraband transitions when the chemical potential μ is below the bottom of the conduction band. Thus, the blue lines representing E_c^{Min} in Figure 12 and Figure 13 shows clearly where the onset of intraband transitions, in essence the Drude conductivity, are expected for various strains. Next, we know from Figure 4 that interband transitions only are allowed for photon energies that correspond to a vertical transition in the band diagram. In this case it means a photon energy greater than whichever is largest of the bandgap and $\mu - E_v(\mathbf{k})$. Additionally, the curvature of the bands can give more information about what sort of response to expect. If the bands are flat, a relatively localized peak in optical conductivity can be expected compared to steeper bands curving away from each other.

4.2.1 Optical conductivity and permittivity

The Greenwood-Kubo formula in its spectral representation was solved numerically as the Riemann sum shown in equation (3.3.34) within the limits of equation (3.3.33). Benchmarking the algorithms with maximum multithreading on an *AMD Ryzen 9 3900x* (CPU) and an *NVIDIA RTX 2080 Super* (GPU), showed that the GPU implementation performed identical calculations roughly 230 times faster than the CPU counterpart. This highlights the potential performance benefit of adapting these types of calculations to run with high parallelization. Solving the same integral with the global-adaptive quadrature rule showed equivalent results but they converged more slowly. This is likely due to lack of optimization for this particular problem rather than a weakness of the method itself. Developing an efficient global-adaptive quadrature algorithm can be highly challenging, and is outside the scope of this thesis.

To produce the results presented in this section, it was used $n = 4000$ steps for the $\mathbf{k}$- and ω-integrals, a scattering of $\eta = 0.01$ eV, a temperature of 1K, 800 steps for Ω, and the integration limits shown in (3.3.33). The tolerance σ_f for the Fermi function was set to 0.0001. These parameters were chosen carefully after rigorous testing, ensuring that the integrals converged nicely.

First, we can study the dielectric response of unstrained phosphorene. The optical conductivity of phosphorene is shown in Figure 15 a) and 15 b) as a function of incident photon energy $\hbar\Omega$. Here, the plots are normalized by $\sigma_0 = e^2/(8\hbar)$. This is half the universal conductivity for graphene [35], taking into consideration graphene's extra degeneracy factor $g_v = 2$. These figures show that photon energy lower than the bandgap E_g does not induce any conductivity, which is an expected behaviour. In other words, there are no intraband transitions and hence the Drude weight is zero for unstrained phosphorene. It can also be seen that the conductivity in the y-direction has a localized response just around the bandgap while the response in the x-direction increases more slowly and is of smaller magnitude in general. Naturally, this denotes the minimum energy required for interband transitions. The anisotropic behaviour of the optical conductivity can be understood from the anisotropic band structures presented in

the previous section. However, to further link the shape of the conductivity plots to the band structure, a detailed analysis of the allowed energy transitions accompanied by a density of states study needs to be performed. Some details about this study are presented later in this section.
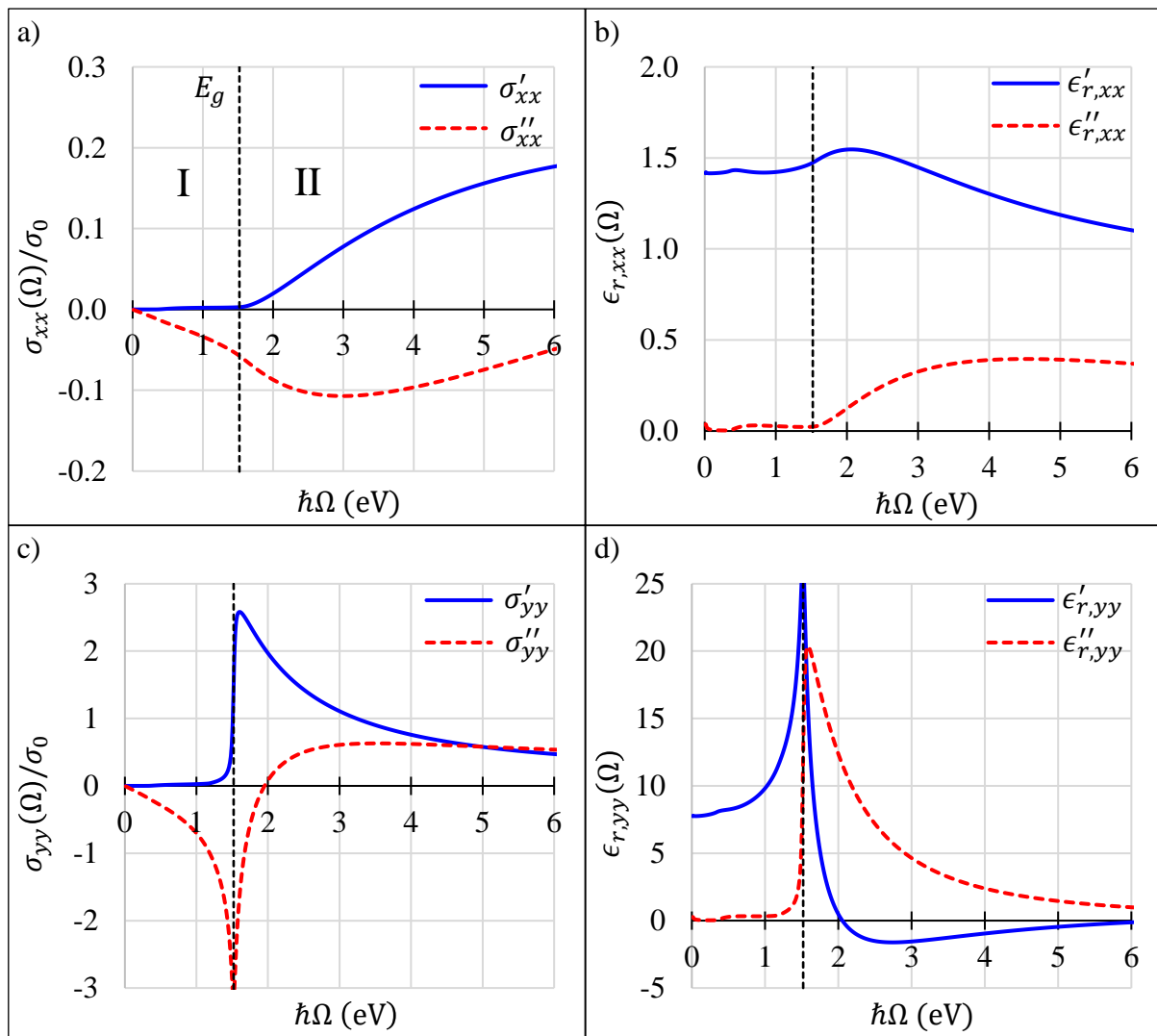

Figure 15: Optical conductivity in a) the x- and c) the y-direction, and the permittivity in b) the x-direction and d) the y-direction. I and II denotes the intraband and interband regime, respectively. The real and imaginary parts are denoted by solid and dotted lines, respectively.

Moving on to the plots in Figure 15 b) and 15 d), the relative permittivity response function can be studied. Figure 15 b) shows that the real part of the relative permittivity for an incident electric field polarized in the x-direction resides within 1.0 to ∼1.5, which is similar to the dielectric properties of air and vacuum. The response for the same process in the y-direction is quite different, where it resides in the range $\epsilon_{r,yy} \in [-5,30]$. This means that the dielectric response of pristine phosphorene is a lot more frequency dependent of incident electric fields polarized in the y-direction compared to the x-direction. In both cases, the relative permittivity seems to converge towards $\epsilon_r = 1$ as photon energies approach 6.0 eV and beyond. It is however important to point out that photon energies higher than this is beyond the scope of this

low-energy model, and hence also outside the scope of this thesis. The imaginary part of the permittivity is simply $\epsilon_{r,\alpha\alpha}'' = (\sigma_{\alpha\alpha}'/\sigma_0) \cdot (4\pi/\Omega)$ which follows from equation (2.4.1).

If we study the relative permittivity in the y-direction, shown in more detailed in Figure 15 d), an interesting property is that it crosses zero for photon energies at ~2 eV and ~6 eV. If we recall the related quantities presented in section 0, these points highlight some interesting physical properties. Some of the most noteworthy properties, are that the power dissipation of an incident y-polarized alternating electric field has zero power dissipation associated with it and the capacitance in such a case is zero. Additionally, it can be seen from equation (2.4.12) coupled with (2.4.14) that the absorption and index of refraction at these photon energies are ultimately determined by the magnitude of $\epsilon_{r,yy}''$. The absorptance is studied in greater detail in the attached paper manuscript.
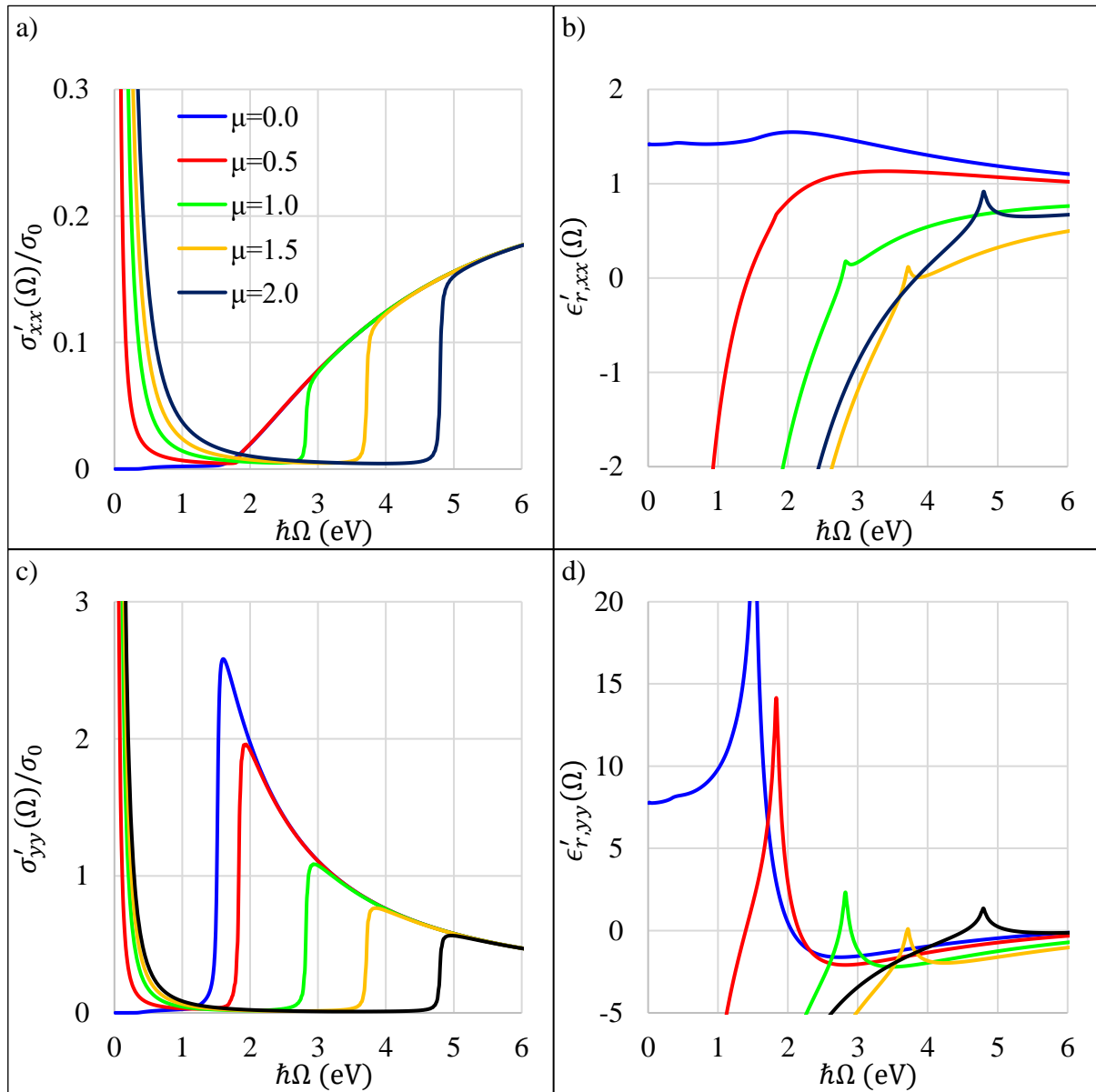

Figure 16: The effect of μ on the optical conductivity in a) the x-direction and c) the y-direction, as well as its effect on the permittivity in b) the x-direction and d) the y-direction.

Next, we can study the effect that changing the chemical potential has on the optical conductivity and permittivity. The chemical potential can be changed by introducing dopants to phosphorene or combining it with a gate electrode. This is shown in Figure 16, which shows that raising the chemical potential primarily changes two properties: it introduces Drude conductivity from intraband transitions at roughly $\mu > E_c^{\text{Min}}$ and it increases the minimum energy required for interband transitions. These effects are coherent with expectations from the band analysis in previous sections. Integrating the low energy response $\hbar\Omega \ll E_g$ for multiple values of μ results in the Drude weight as a function of μ like the one presented in Figure 9, but this study is saved for section 4.2.2. Finally, it can be seen that the real and imaginary parts of the relative permittivity approach negative and positive infinity as $\hbar\Omega$ approaches zero, respectively. This permittivity characteristic is typical for metals.

Additionally, the effect of strain on the conductivity and permittivity can be investigated. Figure 17 shows the optical conductivity and permittivity for biaxial strain ranging from -10% to 10%. Applying negative strain reduces the bandgap and hence the onset of interband transitions are shifted to lower energies. In the y-direction the magnitude is inversely related to the strain, which can be understood from Figure 10 as negative strain increases the curvature of the bands in the k_y-direction and vice versa for positive strain. In the x-direction, negative strain increases the optical activity for energies smaller than 5 eV and positive strain increases the optical activity at higher energies. Thus, strain can be used to shift the active optical energy range for x-polarized incident **E**-fields.

To better visualize the interband transitions possible within phosphorene, Figure 18 can be used. Figure 18 shows surfaces of all possible interband transitions that conserves energy and momentum simultaneously, and thus illustrates the effect of strain on interband transitions. Here it can be seen that applying a positive biaxial strain of 10% flattens the bands in **k**-space, which means that there are more possible **k**-values for any given energy transition. It also means that the **k**-states near the Γ point are restricted to lower-energy transitions. At first sight there seems to be a contradiction between this figure and the results for optical conductivity. Since the bands are flatter in k_x- direction compared to k_y-direction it would be natural to expect opposite behaviours for σ_{xx} and σ_{yy}. However, a comparison of the interband conductivity across the x- and y-directions based solemnly on the shape in **k**-space is insufficient as it disregards the density of states in either direction. The map of allowed interband transitions can therefore alone only be used to indicate the effect of various parameters along the same axes. To fully link Figure 18 to the optical conductivities, it needs to be coupled with a density of states analysis.

An equivalent study to the biaxial strain was also performed for the case of uniaxial strain. The results from this analysis is presented in Figure 19, where 19 a) to 19 d) shows the case of strain along the x-direction and 19 e) to 19 h) shows strain along the y-direction. It was found that applying strain along the x-direction is mostly equivalent to applying biaxial strain, with only small differences between the magnitudes in either case. Applying strain in the y-direction on the other hand shows very little deviation from unstrained phosphorene. Applying strain along the y-direction effectively just modulates the magnitude of the dielectric response, where the magnitude is proportional to the applied tensile strain.
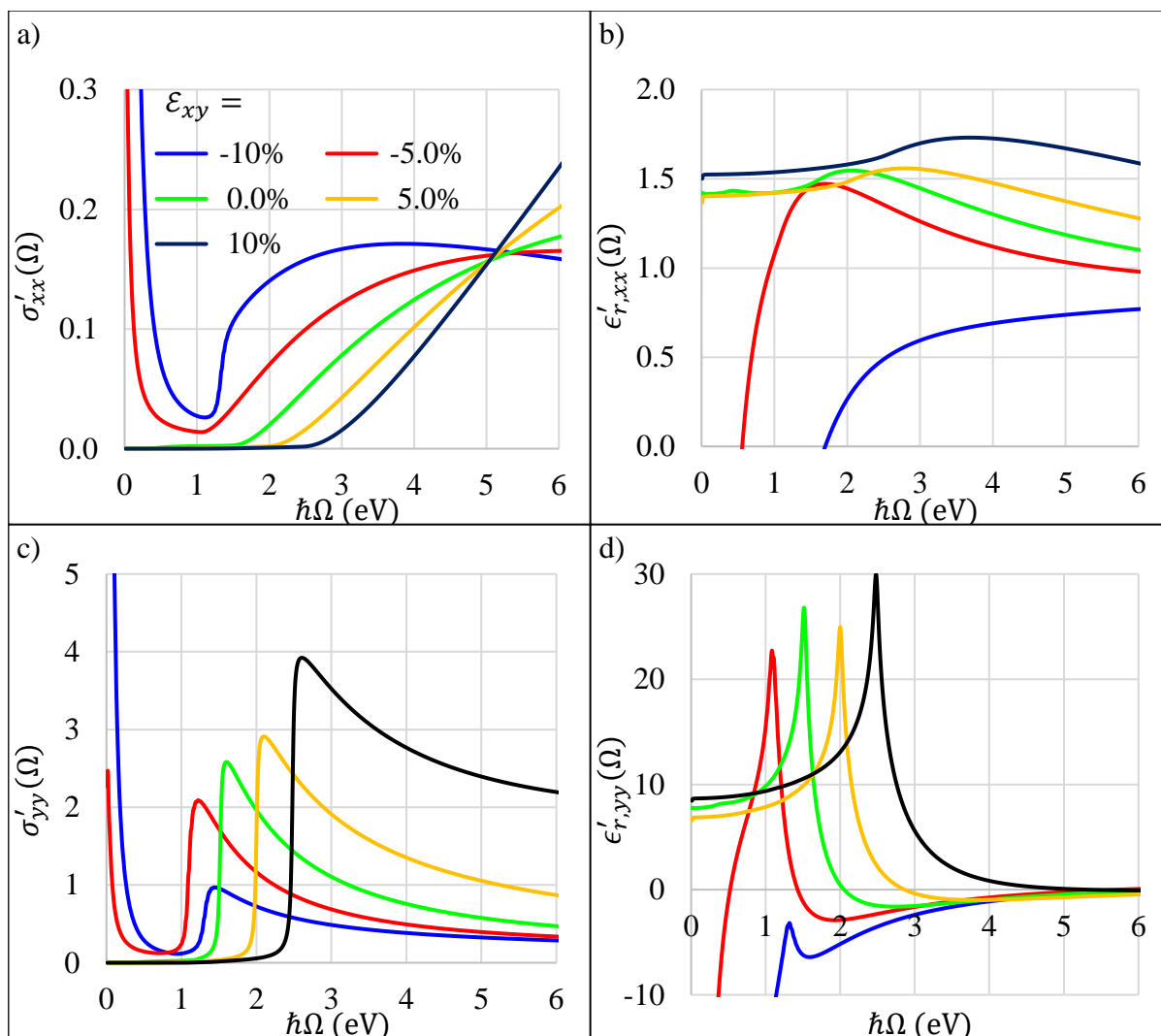
Figure 17: The effect of biaxial strain on the optical conductivity in a) the x-direction and c) the y-direction, as well as its effect on the permittivity in b) the x-direction and d) the y-direction.
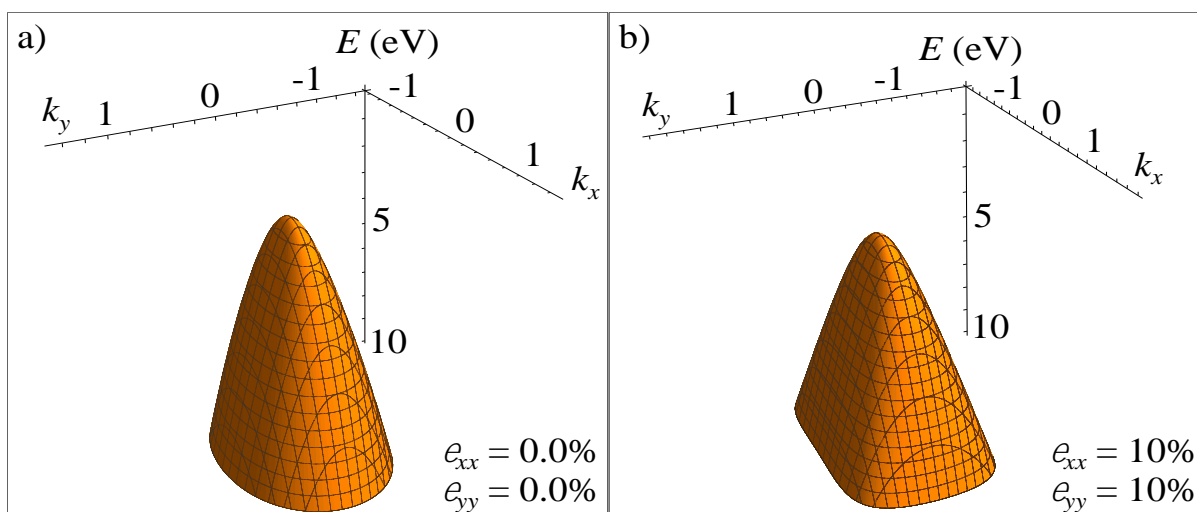

Figure 18: A surface showing the possible interband transitions in terms of energy E and momentum $\mathbf{k}$ for a) pristine phosphorene and b) phosphorene subjected to 10% biaxial strain.
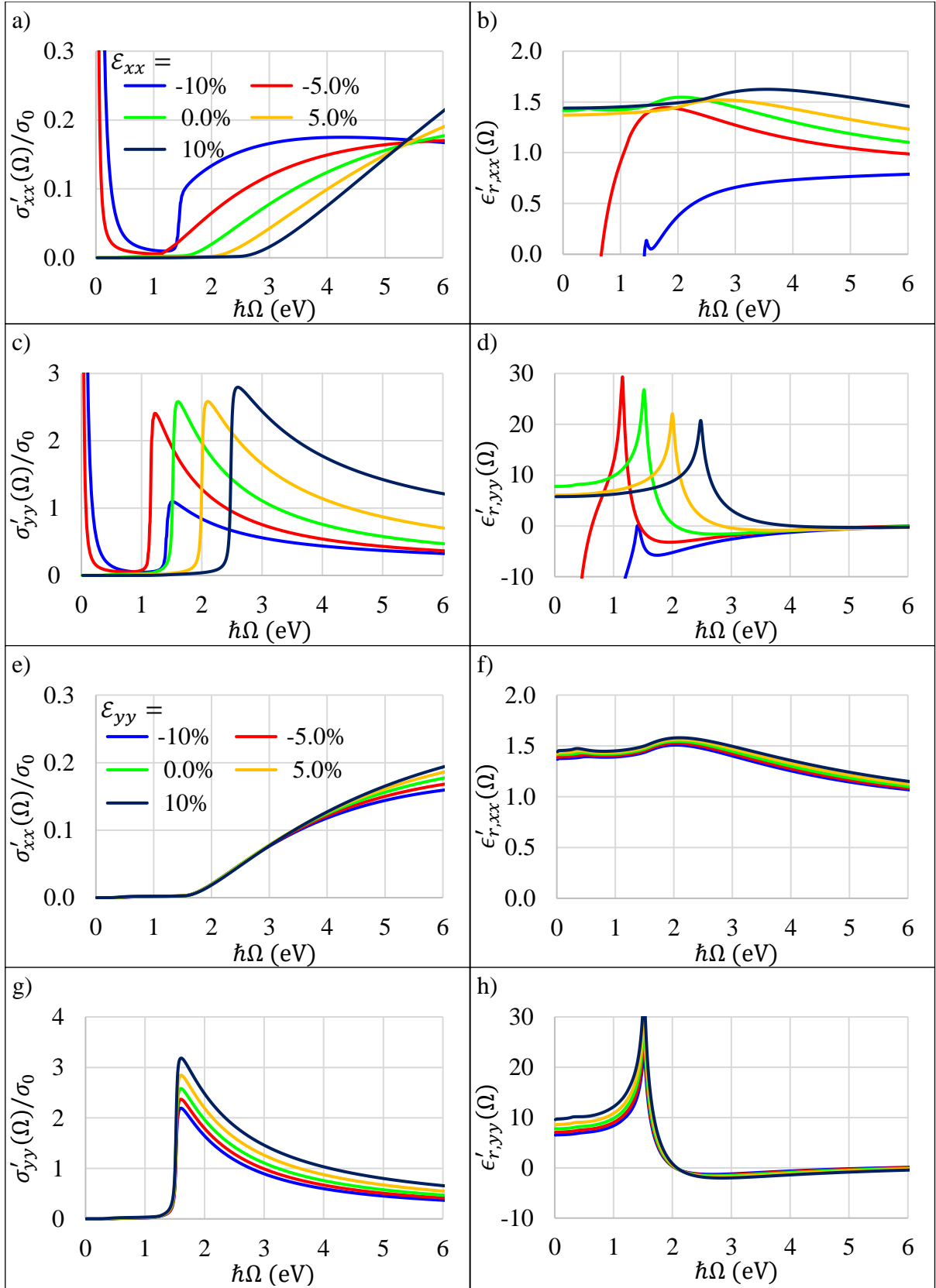
Figure 19: Optical conductivity and permittivity for uniaxial strain in the x-direction (a-d) and the y-direction (e-h).

4.2.2 Drude response

To further link the optical conductivity to the band structure, the Drude weights for various strain values were also calculated from the optical conductivity by integrating it over the Ω near zero response. The result of this analysis is shown in Figure 20, where the same analysis from the bands is included as dotted lines. These dotted lines are the same plots presented in Figure 14, only scaled by a factor of ~0.46. The fact that the Drude weights obtained from equation (2.2.2) requires scaling to fit the ones obtained from the optical conductivity is not very surprising, considering that equation (2.2.2) only describes a proportional relationship between the left- and right-hand side. The solid curves are spline-interpolations of the Drude part of the optical conductivity calculated for 51 different μ values for each strain value.

The analysis from the optical conductivity thus shows a perfect match to those obtained from the band structure, including the key features such as the onset at $\mu = E_c^{\mathrm{Min}}$. In addition to just plotting the Drude weights, we can adjust all the curves to start from the origin. This is done in Figure 21, which shows how only the slopes of the Drude weight is affected by strain in both directions. Yet again, the anisotropic properties of phosphorene is apparent. In this figure, it can be seen that the Drude weight for positive 10% strain is the smallest of the three strain-values in the x-direction, but the largest in the y-direction, and vice versa for -10% strain. This can be attributed to the high anisotropy between the directions in the phosphorene system.
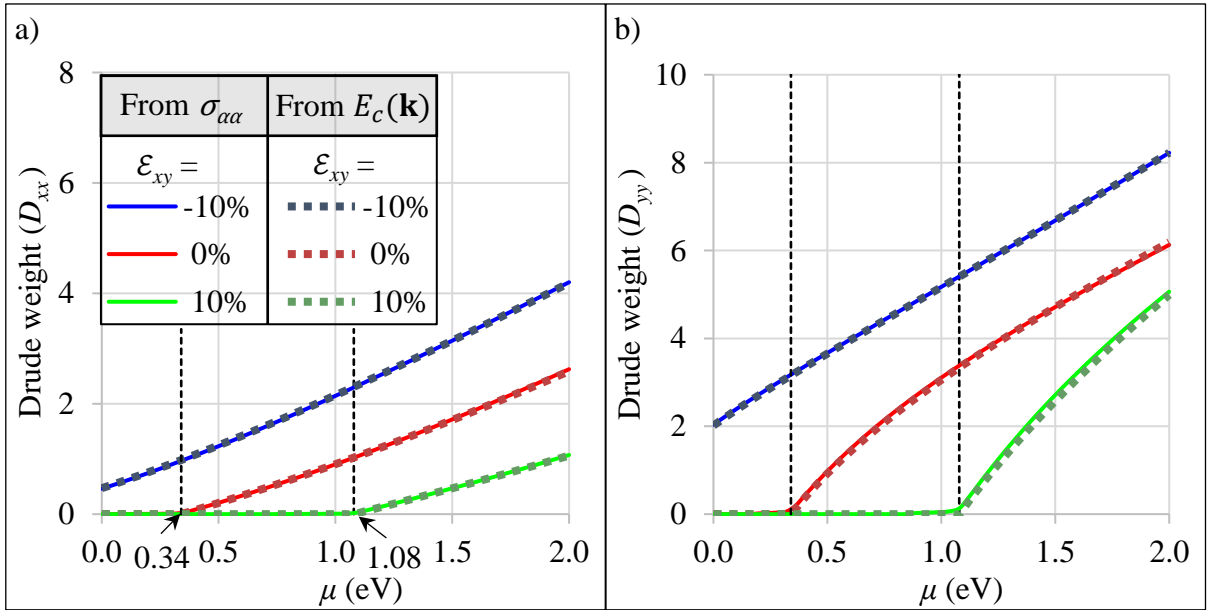

Figure 20: Drude weights in a) the x-direction and b) the y-direction. The solid lines are the Drude weights calculated by integrating the Ω near zero part of the optical conductivity, and the dotted lines are the ones calculated from the band structure scaled by a factor of ~0.46.
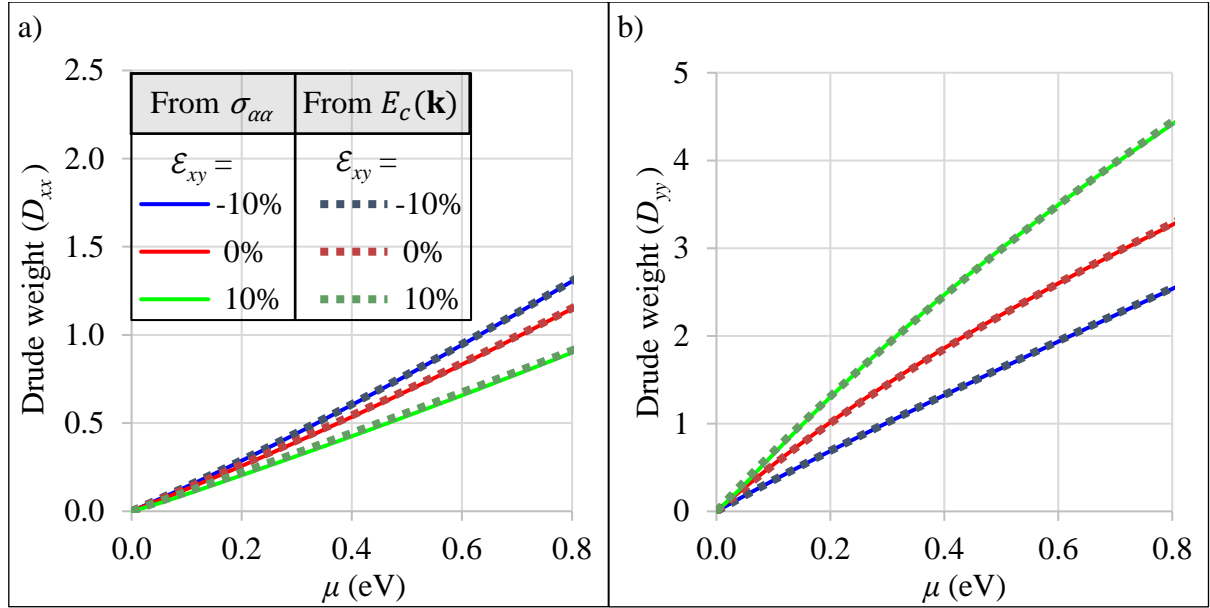
Figure 21: Drude weights from both the optical conductivity and the band structure, adjusted to the origin.

4.3 Validity and significance of results

In addition to the detailed study of each parameter individually, such as the band structure, dielectric response and Drude weights, it is useful to evaluate the results in its full picture as well as compare them to similar studies. This is important in order to notice inconsistencies with own and others results.

Through the study of the band structure, Drude weights, and optical conductivities, the results are in excellent agreement. The results are also well-behaved within the studied regime, meaning that there are no obvious discontinuities or unexpected artifacts. This reduces the probability of severe numerical errors or weaknesses in the underlying model. Additionally, by varying the numerical parameters, such as the integration step size and limits in various directions, the integral could be observed to nicely converge towards the obtained results. This indicates that the numerical precision is satisfactorily high, to the point where a reduction in step sizes makes an unnoticeable difference to the results. By additionally evaluating the integrals with the adaptive quadrature method, known for better stability with badly behaved integrands, the probability of systematic errors and overlooked features in the integrand, is significantly reduced.

Compared to other studies, the results presented here are generally consistent with the available literature. A detailed review of the properties of phosphorene was presented in 2017, and it includes details about phosphorene's band structure, mechanical properties, electrical transport properties and optical properties. The bandgap of phosphorene was found to generally reside around ~ 1.6 eV [36] according to band structures calculated from numerous methods including the hybridized and meta density functional theory (DFT) [37, 38], the tight binding approximation [39] and the arguably more reliable GW method in terms of bandgap estimations [40, 41]. The band structures obtained from these models have close resemblance to those obtained here using the low energy $\mathbf{k} \cdot \mathbf{p}$ Hamiltonian. Experimental measurements of the bandgap of phosphorene have found it to reside at ~ 1.73 eV [46]. Thus, the fundamental

properties presented in this thesis are in close agreement with alternative theoretical approaches, and in decent agreement with experimental observations.

In terms of the optoelectronic properties of phosphorene, the optical conductivity calculated in this thesis is in good agreement with the literature. A paper published by Yang *et al.* in 2018 presents a similar study to the one presented here, including the strain-dependence of the optical conductivity. They used a nearest-neighbour tight-binding approximation for obtaining the Hamiltonian, and an alternative approach to solving the Kubo formula in its non-spectral variant. The optical conductivities obtained in their study are in excellent agreement to those obtained in this thesis, showing almost identical magnitudes and shapes in either direction within the range $\hbar\Omega < 6.0$ eV [34].

A more recent paper published in 2020 measured the optical conductivity of few-layered black phosphorous in the y -direction experimentally, by using room-temperature infrared spectroscopy. Their results for σ_{yy} show similar physics and magnitude to the one found in this thesis, including the sharp onset just at the bandgap and a steady but weak decay beyond. However, this paper only studies the y-polarized response and no fewer layers than two-layered black phosphorous [47]. Additionally, their measurements for two-layer black phosphorous are too noisy to compare the delicate features of the curves found here. Thus, their results indicate similar physics to those found here, though it is impossible to fully extrapolate their results to single layer black phosphorous and hence fully validate the detailed shapes of $\sigma_{\alpha\alpha}$ found here.

In summary, the results presented in this thesis are arguably in good agreement with most other theoretical and experimental studies. This indicates that employing a $\mathbf{k} \cdot \mathbf{p}$ low-energy effective Hamiltonian together with the Greenwood-Kubo formula is a viable method to accurately calculate the low-energy dielectric response of 2D materials like phosphorene.

However, this method has some shortcomings to fully model the dielectric response of phosphorene and similar 2D materials, primarily due to its limitation to the low-energy regime. In this study, the low-energy regime was considered to be energies smaller than ~6.0 eV and the study accurately simulates the response of the first bands E_n within this regime. However, even within this region there are higher energy bands that could be considered and added to the conductivity results presented here. It could therefore be highly interesting to perform similar analyses using expanded multi-band models. While the optical response related to the intraband and first interband transitions would remain intact, the inclusion of multiple bands in the study would better model the tails of the conductivity plots from ~3.0 eV and beyond. Future studies performing infrared spectroscopy on single layer black phosphorous, extending the experimental study mentioned earlier, would also be highly valuable to fully compare the theoretical dielectric response of phosphorene found here and in other studies to real measurements.

One of the methods to perform multiband analysis is DFT calculations, which coupled with the random phase approximation (RPA) is a commonly used method to calculate the permittivity and band structures of numerous solids. However, in the attached manuscript, that was mainly extracted from the current thesis (the DFT-RPA calculations for phosphorene were performed by Dr. Alidoust), this ab initio method implied significantly different physics to those obtained by the low-energy effective model. A selection of the results obtained in this thesis has been incorporated in the manuscript to highlight these differences. The DFT-RPA calculations were

found to be inconsistent, as the permittivity calculations among other things implied an anisotropic bandgap that is neither physical nor apparent in the band structure calculated within the same model. Additionally, the DFT-RPA underestimates the bandgap compared to other theoretical studies and experimental results, and shows photon absorption processes that cannot be explained from the corresponding DFT band structure.

Based on these observations, it is pointed out in the manuscript how the DFT-RPA calculations are insufficient to accurately predict the dielectric response of 2D materials similar to phosphorene. Furthermore, it is illustrated in the manuscript how the inaccurate predictions by the DFT-RPA approach for the dielectric response of these materials lead to significant deviations when incorporated in even simple devices, based on the device implementation calculations performed by Dr. Halterman.

It would therefore be highly valuable if future studies were to efficiently incorporate more realistic parameters into dielectric DFT-RPA calculations of 2D materials like phosphorene, to be more consistent with their band structure and experimental results. It is worth noting that the strained phosphorene system studied here is a representative case of 2D materials, and that the findings and conclusions are applicable to a wide range of semiconductors (for further details, the reader is referred to the manuscript). Alternatively, it would be valuable to incorporate multi-band analysis in low-energy calculations and use the Kubo formula like what was carried out here, though this quickly becomes complicated and is still limited to the low-energy regime. In particular, it becomes difficult to obtain analytical expressions for the spectral functions through equation (2.3.6) from complicated Hamiltonians.

5 Conclusion

In this theoretical study, the band structure, the optical conductivity and the permittivity was obtained for single-layer phosphorous from a low-energy effective $\mathbf{k} \cdot \mathbf{p}$ Hamiltonian. A large portion of the study was to investigate the effect of the chemical potential μ and directional in-plane strain on these properties. Additionally, the Drude weights as a function of μ were calculated from both the band structure and the optical conductivity. Overall, the results from these approaches showed great consistency with one another and matched the expectations from theory. The bandgap for various parameters was obtained from both the band analysis and the dielectric analysis, as well as the Drude response. This links the optical conductivity to both the energy level and shape of the conduction band and the maximum energy of the valence band. Phosphorene was found to be a very intriguing material for designing novel optoelectronic devices, with its anisotropic properties along the x- and y-directions.

From the low-energy band structure, it was found that pristine phosphorene is a semiconductor with a direct bandgap of 1.52 eV. The bands had anisotropic structure in the k_x- and k_y-directions, showing the greatest curvature in the k_y-direction. Increasing the chemical potential, which effectively can be done by adding dopants or incorporating gate electrodes, was shown to induce a non-zero Drude weight at $\mu \geq 0.34$ eV. This corresponds to the energy at the bottom of the conduction band, meaning that charge carriers are introduced to the conduction band beyond this energy. Thus, the chemical potential can be used to control the charge density in the conduction band, which when excited by low-energy perturbations becomes conductive. To stay within the low-energy bounds of the model, a chemical potential ranging from zero to two electron volts was used.

Applying strain to phosphorene shifted the energy level of both the conduction band and valence band, and also changed the curvature of the bands. Strain values of both biaxial and uniaxial strain in the range -10% to 10% was studied, which is within the limits of the low-energy regime and the elastic range of phosphorene, without causing any structural transitions or rupture. Negative biaxial strain (compressive strain) reduced the bandgap to as low as 0.56 eV, increased the curvature of the bands, and shifted the conduction band below the Fermi energy $\mu = E_F = 0$ eV, and thus made phosphorene metallic in its conductivity characteristics. Positive strain resulted in the opposite effect by increasing the bandgap to as high as 2.5 eV and reduced the curvature of the bands. Uniaxial strain along the x-axis yielded similar effects as the biaxial strain, and primarily effected the conduction band, while the effect of uniaxial strain along the y-axis made a smaller impact on the bandgap and primarily lowered the energy of the valence band. The application of strain shifted the onset of the Drude weight as a result of the conduction band being shifted towards and below the Fermi energy.

The real part of the optical conductivity was obtained from the low-energy effective Hamiltonian through the Greenwood-Kubo formula in its spectral representation, and the imaginary part was then obtained through the Kramer-Kronig relations. At chemical potentials below the conduction band, the intraband conductivity at photon energies $\hbar\Omega \approx 0$, corresponding to the Drude part, was found to be zero as expected. The onset of the conductivity from interband transitions had an onset on photon energies $\hbar\Omega \geq E_g$, which was further shifted to higher energies for chemical potentials greater than the conduction band: $\mu > E_c^{\mathrm{Min}}$. The conductivity in the x-direction increased with increasing photon energies, and

the conductivity in the y-direction had a localized response near the energy of the bandgap and then decayed. As soon as the chemical potential was raised beyond the bottom of the conduction band, the Drude conductivity appeared. Apart from introducing Drude weights and shifting the interband transitions to higher energies, the chemical potential had little effect on the optical conductivity.

Applying biaxial strain and uniaxial strain in the x-direction had similar effects on the optical conductivity, by introducing Drude conductivity and shifting the energy of the onset of the interband regime. The physical nature of these effects is well described by the effect of strain on the band structures. Strain in the y-direction on the other hand, only slightly altered the optical properties by primarily modulating the magnitude of the optical conductivity in both directions.

Next, the relative permittivity was found to mostly reside between zero and two in the x-direction, though a metal-like behaviour was seen at higher chemical potentials and for negative biaxial strain and uniaxial strain in the x-direction. The metallic behaviour was manifested as the permittivity approaching negative infinity in the $\hbar\Omega$ near zero regime. The permittivity in the y-direction showed a localized peak around the bandgap, as well as some interesting points where the relative permittivity equated zero. The real part of the relative permittivity in this direction resided within $\epsilon'_{r,yy} \in [-5, 30]$ for the most part. At the zero-points, an electric field polarized in the y-direction thus has no power dissipation and the capacitance for that frequency is zero. There were some exceptions to the ranges specified above for both $\epsilon'_{r,xx}$ and $\epsilon'_{r,yy}$, specifically at large chemical potentials and strain values below -5%, as they were both seen to approach negative infinity at these values and beyond.

Finally, it was found that the results for the optical conductivity was coherent to the band structure. This was apparent through the expectations for the intraband and interband transitions, as well as a perfect match in the Drude weights calculated from the optical conductivity and the band structure separately. Hence, the results were found to be compatible, solidly founded in established physics and in good agreement with other theoretical and experimental studies. The low-energy $\mathbf{k} \cdot \mathbf{p}$ effective Hamiltonian was therefore concluded to be a viable approach to accurately predict the dielectric response of the first bands of 2D materials alike phosphorene, within a low-energy regime of photon energies $\hbar\Omega < 6$ eV. To expand the analysis, it would be highly valuable with experimental studies of phosphorene, and multi-band theoretical approaches to better simulate the tails of the optical conductivity and permittivity beyond ~ 3 eV. This includes more complex low-energy studies, or alternatively an improved DFT approach.

By comparing the results in this thesis to an equivalent analysis utilising density functional theory with a random phase approximation (DFT-RPA), performed in the attached manuscript, there was however a significant deviation between the results obtained by the two methods. In contrast to the low-energy model, common DFT-RPA approaches were unable to reveal intricate features of the optoelectronic properties of 2D materials, and they disagree with physical expectations from the corresponding band structure. The manuscript shows how accurate predictions of the optical response are essential for designing optoelectronic devices. It would therefore be highly valuable if future studies were to efficiently incorporate more realistic parameters into dielectric DFT-RPA calculations of 2D materials like phosphorene, to be more consistent with experimental results and the materials' corresponding bandgap.

6 References

[1] V. Petrova-Koch, Milestones of Solar Conversion and Photovoltaics, Berlin: Springer, 2009.

[2] W. Smith, "Effect of Light on Selenium During the Passage of An Electric Current*," *Nature,* vol. 7, no. 173, p. 303, 1873. DOI: 10.1038/007303e0.

[3] M. Planck, "Ueber das Gesetz der Energieverteilung im Normalspectrum," *Annalen der Physik,* vol. 309, no. 3, pp. 553-563, 1901. DOI: 10.1002/andp.19013090310.

[4] The Noble Prize in Physics, "NobelPrize.org," Nobel Media AB, June 2020. [Online]. Available: https://www.nobelprize.org/prizes/physics/1921/summary/. [Accessed 20 June 2021].

[5] X. Wang, Y. Cui, T. Li, M. Lei, J. Li and Z. Wei, "Recent Advances in the Functional 2D Photonic and Optoelectronic Devices," *Advanced optical materials,* vol. 7, p. 1801274, 2019. DOI: 10.1002/adom.201801274.

[6] O. Lopez-Sanchez, D. Lembke and M. Kayci, et al., "Ultrasensitive photodetectors based on monolayer MoS2," *Nature Nanotechnology,* vol. 8, pp. 497-501, 2013. DOI: 10.1038/nnano.2013.100.

[7] S. L. He, M. Sung-Wook and C. Youn-Gyung, et al., "MoS2 Nanosheet Phototransistors with Thickness-Modulated Optical Energy Gap," *Nano Letters,* vol. 12, no. 7, p. 3695–3700, 2012. DOI: 10.1021/nl301485q.

[8] C. Woong, Y. C. Mi and K. Aniruddha, et al., "High-Detectivity Multilayer MoS2 Phototransistors with Spectral Response from Ultraviolet to Infrared," *Advanced Materials,* vol. 24, no. 43, pp. 5832-5836, 2012. DOI: 10.1002/adma.201201909.

[9] R. B. Laughlin, "Quantized Hall conductivity in two dimensions," *Phys. Rev. B,* vol. 23, no. 10, pp. 5632-5633, 1981. DOI: https://link.aps.org/doi/10.1103/PhysRevB.23.5632.

[10] L. A. Walch and C. L. Hinkle, "van der Waals epitaxy: 2D materials and topological insulators," *Applied materials today,* vol. 9, pp. 504-515, 2017. DOI: 10.1016/j.apmt.2017.09.010.

[11] C. Kittel, Introduction to Solid State Physics, California: John Wiley & Sons, Inc., 2004.

[12] E. Malic and A. Knorr, Graphene and Carbon Nanotubes. Ultrafast Optics and Relaxation Dynamics, Weinheim: Wiley-VCH Verlag, 2013.

[13] J. M. Luttinger, Quantum Theory of Cyclotron Resonance in Semiconductors: General Theory, American Physical Society, 1956. DOI: 10.1103/PhysRev.102.1030.

[14] L. C. L. Y. Voon and M. Willatzen, The k p Method, Berlin: Springer, 2009. DOI: 10.1007/978-3-540-92872.

[15] G. D. Mahan, Many-Particle Physics, New York: Plenum Press, 1981.

[16] J. Singh, Smart Electronic Materials, Fundamentals and Applications, Cambridge: Cambridge University Press, 2005. ISBN: 978-0-521-85027-4.

[17] V. P. Gusynin, S. G. Sharapov and J. P. Carbotte, "Sum rules for the optical and Hall conductivity in graphene," *Phys. Rev. B,* vol. 75, no. 16, p. 165407, 2007. DOI: 10.1103/PhysRevB.75.165407.

[18] M. Jablan, H. Buljan and M. Solja, "Transverse electric plasmons in bilayer graphene," *Opt. Express,* vol. 19, no. 12, pp. 11236-11241, 2011. DOI: 10.1364/OE.19.011236.

[19] N. W. Ashcroft and N. D. Mermin, Solid State Physics, Philadelphia: Harcourt, 1976.

[20] E. N. Economou, Green's Functions in Quantum Physics, Third Edition, Berlin Heidelberg: Springer, 2006.

[21] P. Justice, E. Marshman and C. Singh, "Student understanding of Fermi energy, the Fermi-Dirac distribution and total electronic energy of a free electron gas," *European Journal of Physics,* vol. 41, no. 1, p. 015704, 2019. DOI: 10.1088/1361-6404/ab537c.

[22] E. J. Nicol and J. P. Carbotte, "Optical conductivity of bilayer graphene with and without an asymmetry gap," *Phys. Rev. B,* vol. 77, no. 15, p. 155409, 2008. DOI: 10.1103/PhysRevB.77.155409.

[23] S. H. Hall and H. L. Heck, Advanced Signal Integrity For High-Speed Digital Designs, John Wiley sonds, inc., 2009.

[24] D. K. Cheng, Field and Wave Electromagnetics, California: Addison-Wesley publishing company, 1983. ISBN: 0-201-01239-1.

[25] B. I. Bleaney, Electricity and Magnetism (Third edition), Oxford University Press, 1976. ISBN: 978-0-19-851141-0.

[26] F. Wooten, Optical Properties of Solids, New York: Academic Press, 1972. ISBN: 978-0-12-763450-0.

[27] L. Li, Y. Yu, G. J. Ye, Q. Ge, X. Ou, H. Wu, D. Feng, X. H. Chen and Y. Zhang, "Black phosphorus field-effect transistors," *Nature Nanotechnology,* vol. 9, no. 5, pp. 372-377, 2014. DOI: 10.1038/nnano.2014.35.

[28] C. Liu, H. Jiang and Y. Yao, "Low-energy effective Hamiltonian involving spin-orbit coupling in silicene and two-dimensional germanium and tin," *Phys. Rev. B,* vol. 84, no. 19, p. 195430, 2011. DOI: 10.1103/PhysRevB.84.195430.

[29] M. Alidoust, M. Willartzen and A.-P. Jauho, "Strain-engineered Majorana Zero Energy Modes and φ0 Josephson State in Black Phosphorus," *Physical Review B,* vol. 98, no. 8, p. 085414, 2018. DOI: 10.1103/PhysRevB.98.085414.

[30] P. Li and I. Appelbaum, "Electrons and holes in phosphorene," *Phys. Rev. B,* vol. 90, no. 11, p. 115439, 2014. DOI: 10.1103/PhysRevB.90.115439.

[31] L. C. L. Y. Voon, A. Lopez-Bezanilla, J. Wang, Y. Zhang and M. Willatzen, "Effective Hamiltonians for phosphorene and silicene," *New Journal of Physics,* vol. 17, no. 2, p. 025004, 2015. DOI: 10.1088/1367-2630/17/2/025004.

[32] M. Alidoust, M. Willatzen and A.-P. Jauho, "Control of superconducting pairing symmetries in monolayer black phosphorus," *Phys. Rev. B,* vol. 99, no. 12, p. 125417, 2019. DOI: 10.1103/PhysRevB.99.125417.

[33] E. U. Condon, G. R. Harrison, E. Hutchisson and K. K. Darrow, Quantum Mechanics, International series in pure and applied physics, 1983.

[34] H. Ting, H. Yang and D. Jinming, "Mechanical and electronic properties of monolayer and bilayer phosphorene under uniaxial and isotropic strains," *Nanotechnology,* vol. 25, no. 45, p. 455703, 2014. DOI: 10.1088/0957-4484/25/45/455703.

[35] L. C. L. Y. Voon, J. Wang, Y. Zhang and M. Willatzen, "Band parameters of phosphorene," *Journal of Physics: Conference Series,* vol. 633, p. 012042, 2015.

[36] S. Dragomir, P. Cerone and A. Sofo, "Some remarks on the midpoint rule in numerical integration," *Studia Universitatis Babeş-Bolyai. Mathematica,* vol. 45, no. 2, 2000.

[37] P. P. Schmidt, "A method for the convolution of lineshapes which involve the Lorentz distribution," *Journal of Physics B: Atomic and Molecular Physics,* vol. 9, no. 13, pp. 2331-2339, 1976. DOI: 10.1088/0022-3700/9/13/018.

[38] C. H. Yang, J. Y. Zhang, G. X. Wang and C. Zhang, "Dependence of the optical conductivity on the uniaxial and biaxial strains in black phosphorene," *Phys. Rev. B,* vol. 97, no. 24, p. 245408, 2018. DOI: 10.1103/PhysRevB.97.245408.

[39] Y. Wang and D. R. Andersen, "First-principles study of the terahertz third-order nonlinear response of metallic armchair graphene nanoribbons.," *Phys. Rev. B,* vol. 93, no. 23, p. 235430, 2016. DOI: 10.1103/PhysRevB.93.235430.

[40] A. Chaves, W. Ji, J. Maassen and T. L. T. Dumitrica, "Theoretical overview of black phosphorus," in *2D Materials: Properties and Devices*, Cambridge, Cambridge University Press, 2017.

[41] J. Qiao, X. Kong, Z.-X. Hu, F. Yang and W. Ji, "High-mobility transport anisotropy and linear dichroism in few-layer black phosphorus.," *Nature Communications,* vol. 5, p. 4475, 2014. DOI: 10.1038/ncomms5475.

[42] A. Sengupta, M. Audiffred, T. Heine and T. A. Niehaus, "Stacking dependence of carrier transport properties in multilayered black phosphorous," *Phys Condens Matter,* vol. 28, no. 7, p. 075001, 2016. DOI: 10.1088/0953-8984/28/7/075001.

[43] J. M. Pereira and M. I. Katsnelson, "Landau levels of single-layer and bilayer phosphorene," *Phys. Rev. B,* vol. 92, no. 7, p. 075437, 2015. DOI: 10.1103/PhysRevB.92.075437.

[44] A. N. Rudenko and M. I. Kasnelson, "Quasiparticle band structure and tight-binding model for single- and bilayer black phosphorus," *Phys. Rev. B,* vol. 89, no. 20, p. 201408, 2014. DOI: 10.1103/PhysRevB.89.201408.

[45] M. Alidoust, K. Halterman, D. Pan, M. Willatzen and J. Akola, "Strain-engineered widely tunable perfect absorption angle in black phosphorus from first principles," *Phys. Rev. B,* vol. 102, no. 11, p. 115307, 2020. DOI: 10.1103/PhysRevB.102.115307.

[46] L. Li, J. Kim, C. Jin, G. Ye and D. Y. Qui, et al., "Direct Observation of the layer-dependent electronic strucutre in phosphorene.," *Nature nanotechnology,* vol. 12, p. 21–25, 2016. DOI: 10.1038/nnano.2016.171.

[47] G. Zhang, S. Huang and F. Wang, et al., "The optical conductivity of few-layer black phosphorus by infrared spectroscopy," *nature communications,* vol. 11, p. 1847, 2020. DOI: 10.1038/s41467-020-15699-7.

7 Appendix - Manuscript

Comparison of Optical Response from DFT-Random-Phase-Approximation and Low-Energy Effective Model: The Case of Strained Phosphorene

Mohammad Alidoust,[1] Erlend Isachsen,[1] Klaus Halterman,[2] and Jaakko Akola[1,3]

[1]*Department of Physics, Norwegian University of Science and Technology, N-7491 Trondheim, Norway*
[2]*Michelson Lab, Physics Division, Naval Air Warfare Center, China Lake, California 93555, USA*
[3]*Laboratory of Physics, Faculty of Natural Sciences, Tampere University of Technology, FI-33101 Tampere, Finland*
(Dated: June 22, 2021)

The engineering of the optical response of materials is a paradigm that demands microscopic-level accuracy and reliable predictive theoretical tools. Here we compare and contrast the dispersive permittivity tensor, using both a low-energy effective model and density functional theory (DFT). As a representative material, phosphorene subject to strain is considered. Employing a low-energy model Hamiltonian with a Green's function current-current correlation function, we compute the dynamical optical conductivity and its associated permittivity tensor. For the DFT approach, first-principles calculations make use of the first-order random-phase approximation (RPA). Our results reveal that although the two models are generally in agreement within the low-strain and low-frequency regime, the intricate features associated with the fundamental physical properties of the system and optoelectronic device implementation such as band gap, Drude absorption response, vanishing real part, absorptivity, and sign of permittivity over the frequency range show significant discrepancies. Our results suggest that the RPA approximation employed in widely used DFT packages should be revisited and improved to be able to predict these fundamental electronic characteristics of a given material with confidence.

I. INTRODUCTION

The dynamical finite-frequency optical conductivity and permittivity are the most pivotal quantities in designing optoelectronic devices.[1,2] Various measurable optical properties such as the complex index of refraction, the reflectivity, and absorptivity are governed directly by the permittivity of the medium, which in turn is directly related to the optical conductivity of a time varying incident electromagnetic (EM) wave.[1,3] The permittivity also connects the mutual influence of the medium and electric field of the incident EM wave, i.e., the light-matter interactions, and can reveal the precise nature of the medium.[1,4] Moreover, there is an emerging need for optoelectronic chip architectures that require precise determination and manipulation of the permittivity and optical conductivity to benefit current fabrication techniques and advance technological applications.[2] Only then can fast, ultracompact low-power applications be efficiently realized.

First-principles calculations reside at the frontier of accurate simulations of various materials platforms.[5] For example, density functional theory (DFT) calculations have shown success in simulating the general band gap trend as a function of the number of layers in certain two-dimensional (2D) materials, such as black phosphorus, which constitutes a designed material (with desirable key characteristics such as epsilon-near-zero response[6,7]), and observed in experiments.[8–15] Many 2D materials consist of 2D layers of strongly bonded atoms attached to each other in the third dimension by weak forces. These weakly interacting 2D layers allow for designing novel materials with controllable electronics characteristics with low-cost operations, such as layer displacement. Nevertheless, it has proven that differing functionals and approximations in DFT calculations can modify the absolute band-gap of materials. This issue is more pronounced in 2D materials where both strong covalent bonds and weak van der Waals (vdW) forces are present. This is an important point in the context of DFT, which is unable to properly account for vdW forces.[5]

The weak interlayer vdW interactions provide a unique opportunity to peel off the layers and eventually create a one-atom thick 2D sheet with drastically different electronics properties than the bulk material. Furthermore, performing mechanical operations such as the exertion of strain, on a single-layer material is much easier, as it responds more effectively to these operations compared to the bulk material. The most famous examples include graphene (a single layer of carbon atoms extracted from graphite)[16] and phosphorene (shown in Fig. 1, a single layer of phosphorus atoms extracted from black phosphorus)[17]. Unlike graphene where carbon atoms reside in a single plane, the phosphorene atoms reside within two planes with a finite separation distance, making a puckered structure [see Figs. 1(a) and (b)]. Compared to bulk black phosphorus, phosphorene acquires a fairly large band gap, ~ 1.52 eV, very suitable for semiconductor and field-effect transistor technologies.[14] In the following, we specifically focus on phosphorene (with the possibility of incorporating strain) as its low energy Hamiltonian is available and provides an excellent semiconductor platform for strictly comparing and contrasting the results of DFT and those obtained by the low energy model.

As the influence of vdW forces in a single layer of black phosphorus weakens, one may expect that the deficiencies in the various DFT simulations described earlier would consequently diminish. However, as we shall see below, DFT with a traditional functional still underestimates the band gap of phosphorene. On the other hand, a low-energy effective model can incorporate a proper band gap, as it is calibrated through band structure calculations and experimental inputs when parameterizing a particular model. Furthermore, the low-energy effective model can provide precise and deep insights into the fundamental physical properties of the material, such as dominant transitions across the band gap, which are inaccessible
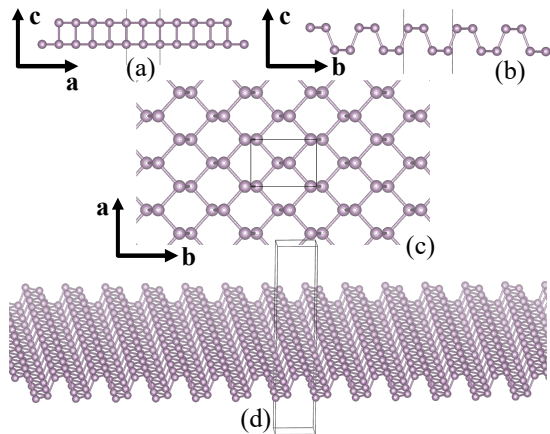
FIG. 1. An expanded unit cell of phosphorene. (a) and (b) exhibit the side views of the 2D material along the **a** and **b** principle axes, whereas (c) shows phosphorene from the top view along the **c**-axis. Panel (d) displays the expanded crystal with a generic view. The 2D material is located at the middle of the unit cell with sufficiently large vacuum regions along the **c** principle axis.

in purely computational approaches like DFT.

In this paper, we compute each component of the permittivity tensor of phosphorene subject to in-plane strain. Two methods are used: One involves DFT combined with a random phase approximation (DFT-RPA),[18–25] and the other uses a low-energy model Hamiltonian with the Green's function current-current correlator. Our results reveal that the permittivity components calculated from DFT-RPA indicate an anisotropic band gap (direction dependent) with magnitude that is incompatible with the corresponding band structure obtained from DFT and the Perdew-Burke-Ernzerhof (PBE) functional. The permittivity tensor computed by the low-energy model however is fully consistent with the associated band gap and clearly describes the underlying physical characteristics of phosphorene. The low energy model also allows for studying the influence of chemical potential or doping variations. We show that in addition to chemical potential variations, the application of strain provides an effective on/off switching mechanism for the Drude response. The underlaying mechanism is the on/off switching of the intraband transitions that can provide valuable information on the band structure of the system. Finally, employing the permittivity data from the DFT and low-energy models, we demonstrate how their differing predictions can influence the precise design of an optoelectronic device. It should be emphasized that although we have studied a specific 2D semiconductor, our conclusions are generalizable to other materials and point to the urgent need for revisiting DFT-RPA implementations used in many DFT packages.

The paper is organized as follows. In Sec. II, the formalisms used in both the DFT-RPA and low-energy models are summarized. In Sec. III A, the components of the permittivity tensor will be presented and the associated physics will be analyzed through band structure diagrams. It will be discussed how the inaccurate results of DFT-RPA are unable to provide correct information on the microscopic properties of the system. In

Sec. III B, the Drude absorption response, and how it provides information on the band structure will be analyzed and discussed. In Sec. III C, the results of DFT and low-energy models will be contrasted in a practical device scenario, where the importance of accurate permittivity predictions are paramount to the proper design of a functional optical device. Finally, a summary and concluding remarks will be given in Sec. IV.

II. FRAMEWORKS AND FORMALISMS

Below, in Sec. II A and Sec. II B, the basics of the two approaches, i.e., first-principles DFT-RPA and the low-energy effective model Hamiltonian used in the Green's function current-current correlator are summarized.

A. First-principles density functional theory

The density functional calculations are based upon the charge density response to sufficiently weak external interactions, such as an electric field. In this case, the Kohn-Sham equations can be evaluated to obtain the dielectric response of the material.[26] In most DFT packages, such as GPAW, Quantum Espresso, and VASP, a random phase approximation (RPA)[18–20] is implemented to evaluate the dielectric response, or permittivity tensor.[21,27] Unfortunately, this approximation neglects the exchange-correlation contribution and can lead to *unphysical* modifications to the original band structure obtained through a specific functional and its associated exchange-correlation.[21] In the linear response regime, the dielectric matrix is given by

$$\epsilon_{G,G'}(\mathbf{q}, \omega) = \delta_{G,G'} - \frac{4\pi}{|\mathbf{q} + \mathbf{G}|} \chi^0_{G,G'}(\mathbf{q}, \omega), \qquad (1)$$

which is linked to the first-order density response χ^0, Bloch vector of the incident wave $\mathbf{q}$, reciprocal lattice vectors $\mathbf{G}$, and the conventional Kronecker delta δ_{ij}. In the RPA regime, the dielectric function is obtained at the Γ point so that

$$\epsilon(\mathbf{q}, \omega) = \frac{1}{\epsilon^{-1}_{0,0}(\mathbf{q}, \omega)}. \qquad (2)$$

In this work, first-principles DFT calculations of the dielectric response are performed using RPA as implemented in the GPAW DFT package.[27–29] The gradient-corrected functional by PBE is used for the exchange-correlation energy when calculating the electronic band structure and the dielectric response. To grid $\mathbf{k}$-space on the basis of the Monkhorst-Pack scheme, a sufficiently large value, i.e., 6.0 $\mathbf{k}$-points per Å^{-1} is incorporated. The cut-off for the kinetic energy of the plane-waves is set to 800 eV, and 60 unoccupied electronic bands are included with a convergence on the first 50 bands. These high values ensure avoiding any artificial effects due to the application of strain in the subsequent calculations that follow. A small imaginary part is added to the frequency variable throughout the calculations, i.e., $\eta = 0.01$ eV, and the width of the Fermi-Dirac distribution is fixed at 0.01 eV.

TABLE I. Band parameters of phosphorene subject to an in-plane strain[30,31].

u_0(eV)	δ_0(eV)	α_x(eV)	α_y(eV)	μ_x(eV)
-0.42	+0.76	+3.15	-0.58	+2.65
μ_y(eV)	η_x(eVÅ^2)	η_y(eVÅ^2)	γ_x(eVÅ^2)	γ_y(eVÅ^2)
+2.16	+0.58	+1.01	+3.93	+ 3.83
β_{xx}(eVÅ^2)	β_{yx}(eVÅ^2)	β_{xy}(eVÅ^2)	β_{yy}(eVÅ^2)	
-3.48	-0.57	+0.80	+2.39	
ν_{xx}(eVÅ^2)	ν_{yx}(eVÅ^2)	ν_{xy}(eVÅ^2)	ν_{yy}(eVÅ^2)	χ_y(eVÅ)
-10.90	-11.33	-41.40	-14.80	+5.25

We introduce the strain parameters s_{ii} (for the $i = x, y, z$ directions), to describe the expansion and compression of the atom's location and unit cell with respect to the relaxed unit cell in each direction, i.e., $a = s_{xx}a_0$, $b = s_{yy}b_0$, and $c = s_{zz}c_0$. Here a, b, and c are the three strained unit cell axis lengths, and the unstrained unit cell axis lengths are a_0, b_0, and c_0. Therefore, in this notation, $s_{xx} = s_{yy} = s_{zz} = 0.9, 1.0$, and 1.1 correspond to strains of -10%, 0%, and $+10\%$, respectively. The strain-free expanded unit cell with differing view angles is shown in Fig. 1. The phosphorene sheet is located in the **a**-**b** plane and a large vacuum region is included in the unit cell in the **c** direction. Since periodic boundary conditions in all directions are set in the numerical simulations, the vacuum spacing in the **c** direction ensures zero overlap of the wave-functions in replicated sheets in the **c** direction. Additionally, as the system is non-magnetic, the permeability is isotropic and can be set to its vacuum value.

B. Low-energy effective model

To study the permittivity of phosphorene subject to an in-plane strain ε_{ii} within the effective low-energy regime, we employ the model Hamiltonian presented in Refs. 30 and 31:

$$H = \int \frac{d\mathbf{k}}{(2\pi)^2} \hat{\psi}_\mathbf{k}^\dagger H(\mathbf{k}) \hat{\psi}_\mathbf{k} =$$
$$\int \frac{d\mathbf{k}}{(2\pi)^2} \hat{\psi}_\mathbf{k}^\dagger \left\{ \left[u_0 + \alpha_i s_{ii} + (\eta_j + \beta_{ij}s_{ii})k_j^2 \right] \tau_0 + \left[\delta_0 + \mu_i s_{ii} + (\gamma_j + \nu_{ij}s_{ii})k_j^2 \right] \tau_x - \chi_y k_y \tau_y \right\} \hat{\psi}_\mathbf{k}, \quad (3)$$

where the indices (i, j) run over the coordinates x, y. Here τ_i are the Pauli matrices in pseudospin space, and $\mathbf{k} = (k_x, k_y)$ is the momentum. The field operator associated with the Hamiltonian is given by $\hat{\psi}^\dagger(\mathbf{k}) = (\psi_A^\dagger, \psi_B^\dagger)$, where the pseudospins are labeled by A and B. The parameters used for this model are summarized in Table I. This model has also been employed to study superconductivity and supercurrent in strained and magnetized phosphorene systems[32,33] where it was found that strain can induce Majorana zero energy modes and drive s-wave and p-wave superconducting correlations to d-wave and f-wave correlations that might explain experimental observations in these contexts[34].

In the low-energy regime, the many-body dielectric response can be expressed by[35],

$$\epsilon_{ab}(\omega) = \delta_{ab} - \lim_{|\mathbf{q}| \to 0} \frac{\Pi_{ab}(\omega, \mathbf{q}) - \Pi_{ab}(0, \mathbf{q})}{\epsilon_0 \omega^2}, \quad (4)$$

in which δ_{ab} is the Kronecker-delta and ϵ_0 is the vacuum permittivity. The current-current correlation functions are given by:

$$\Pi_{ab}(\omega, \mathbf{q}) = e^2 T \sum_n \sum_s \text{Tr} \int \frac{d^2p}{(2\pi)^2} J_a^s G_s(\varepsilon_n + \omega_k, \mathbf{p} + \mathbf{q})$$
$$\times J_b^s G_s(\varepsilon_n, \mathbf{p})\Big|_{i\omega_k \to \omega + i\delta}. \quad (5)$$

Here $J_{a,b}^s$ are the components of the current operators in the a, b directions. The components of the Green's function are labeled G_s, and $\omega_k = 2\pi T k$ and $\varepsilon_n = \pi T(2n + 1)$ are the bosonic and fermionic Matsubara frequencies, respectively (k, n are integers). Finally, the finite-frequency optical conductivity tensor can be obtained from,

$$\sigma_{ab}(\omega) = \frac{i}{\omega} \lim_{|\mathbf{q}| \to 0} \left\{ \Pi_{ab}(\omega, \mathbf{q}) - \Pi_{ab}(0, \mathbf{q}) \right\}. \quad (6)$$

Below, we employ separately these two frameworks discussed in Sec. II A and Sec. II B and compute the components of the permittivity tensor.

III. RESULTS AND DISCUSSIONS

This section is divided into three subsections: In Sec. III A, the various aspects of permittivity and their underlying physical origins will be analyzed by visualizing the associated band structures. In Sec. III B, the Drude absorption of strained phosphorene will be discussed.[36–39] In Sec. III C, the device implications will be presented.

A. Optical transitions and band gap equivalence

We begin with the DFT-RPA approach to calculate the anisotropic dielectric response and band structure of phosphorene. In Fig. 2, the permittivity components $\epsilon_{xx}(\omega)$ and $\epsilon_{yy}(\omega)$ are shown as a function of frequency of the incident light. The associated band structure along the high-symmetry paths in **k**-space calculated by GPAW is also shown. Biaxial in-plane strains of representative strengths -10%, 0%, and $+10\%$ are applied to the phosphorene in columns 2(a)-2(c), respectively. The blue and red curves in the top and middle rows of Fig. 2 correspond to the real and imaginary parts of the permittivity components (as labeled). Both permittivity components $\epsilon_{xx}(\omega)$ and $\epsilon_{yy}(\omega)$ at zero strain [Fig. 2(b1) and Fig. 2(b2)] are nonzero within the low-frequency regime, and approach zero at $\omega \approx 4.7$ eV. The imaginary parts of $\epsilon_{xx}(\omega)$ and $\epsilon_{yy}(\omega)$ exhibit zero loss at frequencies below $\omega \approx 1.5$ eV and $\omega \approx 0.63$ eV, respectively. As the onset of a nonzero imaginary permittivity generally points to photon energies
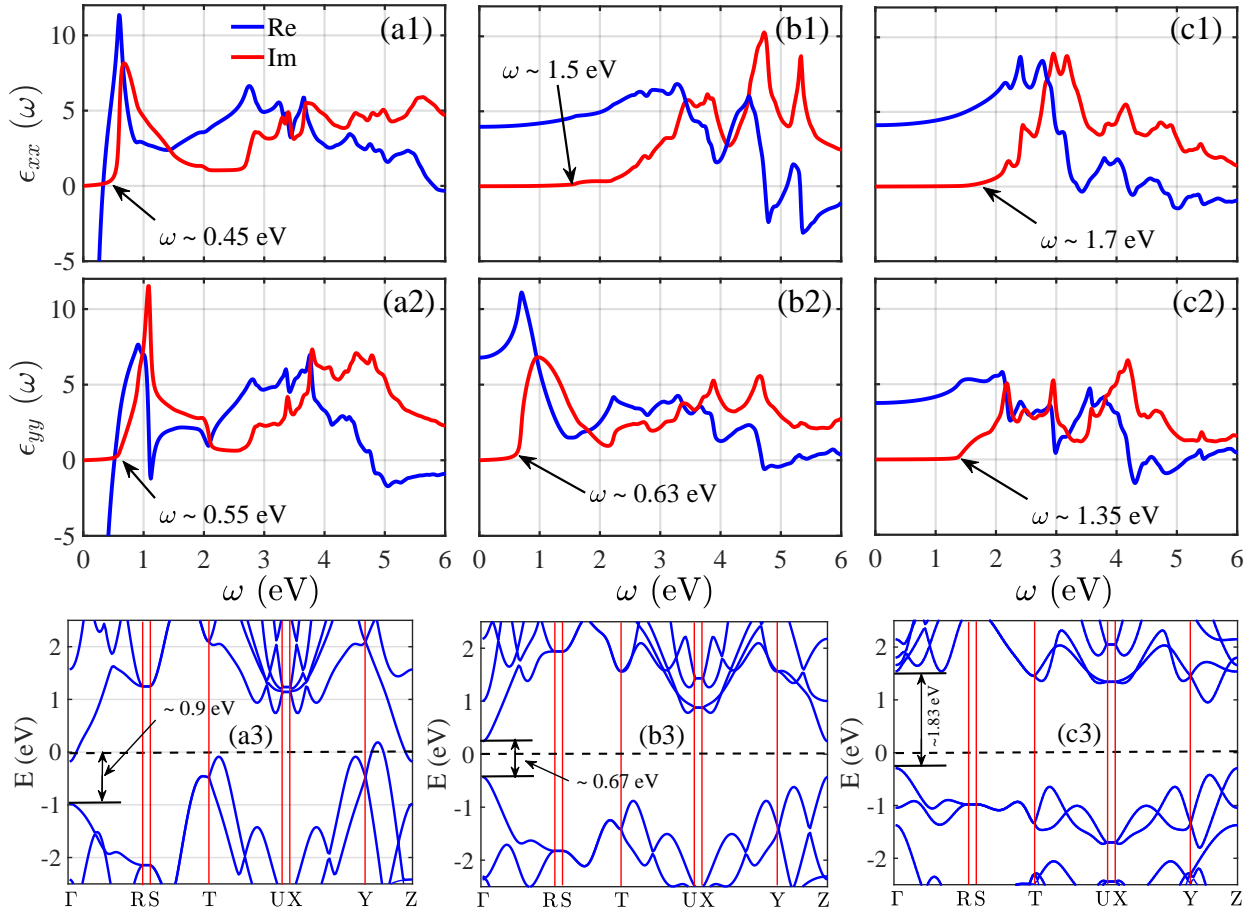
FIG. 2. Real (blue) and imaginary (red) parts of permittivity obtained from first-principles calculations in combination with the RPA (GPAW). The top and middle rows show $\epsilon_{xx}(\omega)$ and $\epsilon_{yy}(\omega)$, respectively, whereas the bottom row is the band structure of phosphorene along the different paths in k-space. Column-wise, (a)-(c) correspond to biaxial strains of -10%, 0%, and $+10\%$, respectively.

that generate electron interband transitions in semiconductors and insulators, one may conclude that the corresponding band structure of the results shown in Figs. 2(b1) and 2(b2) should possesses bidirectional band gap on the orders of $\omega \approx 1.5$ eV and $\omega \approx 0.63$ eV. Note that the intraband transitions within the valence bands are not allowed due to the Pauli exclusion principle. Next, upon applying a compressive strain of -10%, Figs. 2(a1) and 2(a2) show that the real part of the permittivity now begins to diverge when $\omega \to 0$. There are also multiple zero crossings over the given frequency range, and peaks at $\omega \approx 0.59$ eV [Fig. 2(a1)] and $\omega \approx 0.9$ eV [Fig. 2(a2)]. The different threshold frequencies for nonzero imaginary parts, i.e., $\omega \approx 0.45$ eV and $\omega \approx 0.55$ eV, suggest anisotropic interband transitions where the electronic transitions in the x direction experience a larger gap than those occurring in the y direction. Turning the strain type to tensile with the same magnitude, i.e., $+10\%$, Figs. 2(c1) and 2(c2), show that the permittivity components exhibit qualitatively similar behavior to those of zero strain shown in Figs. 2(b1) and 2(b2). As is also seen, the frequency thresholds where the imaginary parts vanish have increased to $\omega \approx 1.7$ eV and $\omega \approx 1.35$ eV, compared to the cases with strains of -10% and 0%, suggesting that there is an increase in the energy gap for the interband

transitions.

To confirm the correlation between the band gap transitions and key regions of the frequency dispersion of the permittivity, the band structure of phosphorene along high symmetry paths in **k**-space is plotted in Figs. 2(a3), 2(b3), and 2(c3). The phosphorene is subject to the same biaxial strain columnwise. The energies are scaled so that the Fermi level resides at $E = 0$ (marked by the dash line). As seen in Fig. 2(b3), the unstrained system has a gap of ~ 0.67 eV at the Γ point. Although it is known that the PBE functional underestimates the band gap of phosphorene (~ 1.52 eV)[6], the information extracted earlier from the permittivity components calculated through DFT-PRA are not consistent with this band gap either. By exerting $+10\%$ strain in Fig. 2(c3), the band gap increases to ~ 1.83 eV, consistent with the behavior of the permittivity seen in Figs. 2(c1) and 2(c2), although the intricate features that correlate with the interband transitions at low energies are not consistent with the band structure. With the application of -10% compressive strain, it is seen in Fig. 2(a3) that the band gap closes and the conduction band at the Γ point crosses the Fermi level. Therefore, the associated permittivity should show metallic characteristics at low energies. Indeed, the real part of permittivity in Figs. 2(a1) and 2(a2) acquires metallic
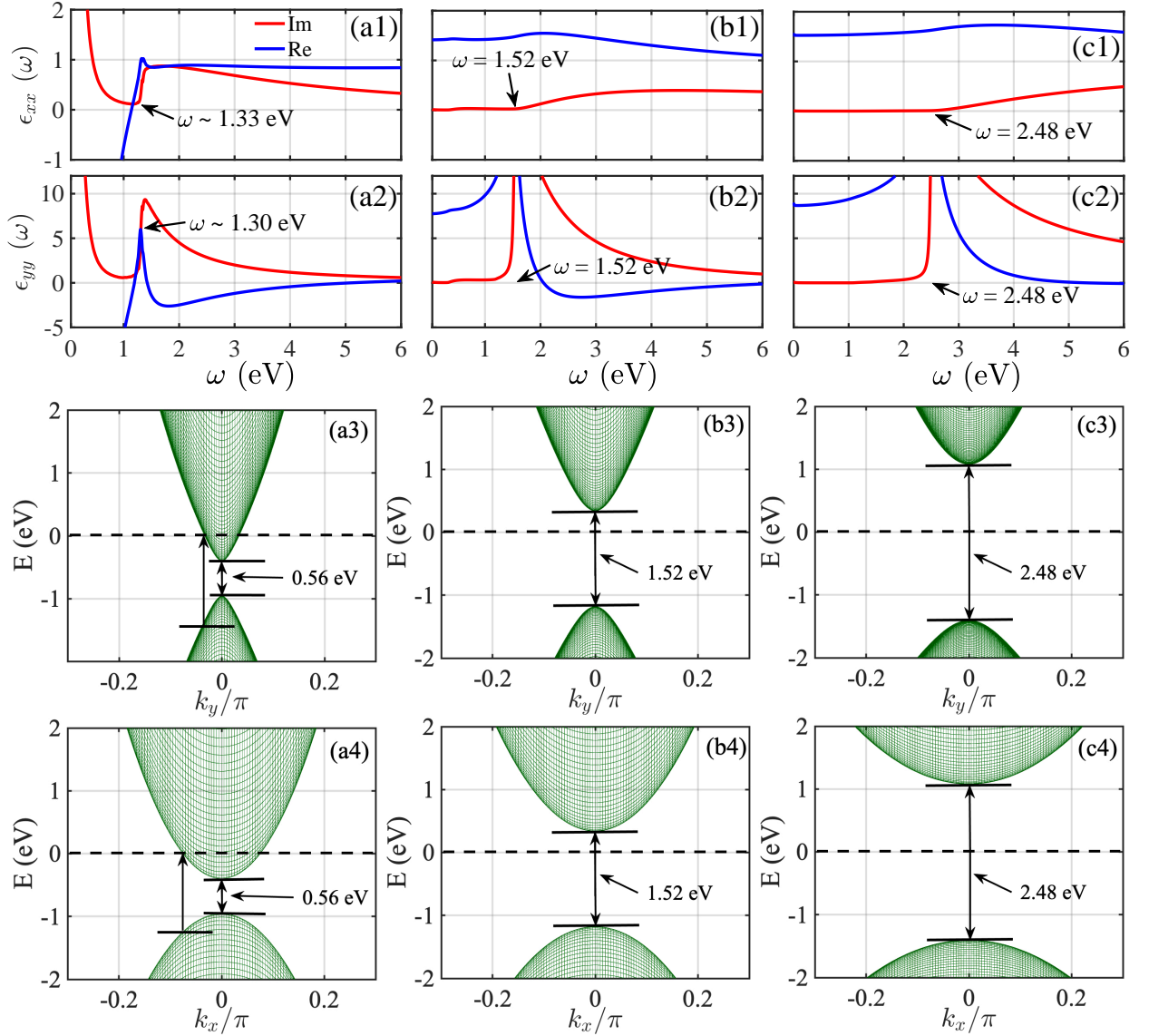
FIG. 3. The permittivity components and associated band structure when using the low-energy effective Hamiltonian. The two top rows show the $\epsilon_{xx}(\omega)$ and $\epsilon_{yy}(\omega)$ components, whereas the two bottom rows depict the band structure along the k_x and k_y directions. In columns (a), (b), and (c) biaxial in-plane strains are applied to the phosphorene system with strengths -10%, 0%, and $+10\%$, respectively.

properties with a Drude-like response, centered around $\omega = 0$, due to the intraband transitions within the conduction band. Nevertheless, the imaginary part of permittivity in Figs. 2(a1) and 2(a2) does not overlap with the Drude peak, suggesting an anisotropic band gap, which is incompatible with the band structure.

We now discuss the finite-frequency optical conductivity and Drude response within the framework of the low-energy model. To simplify our notation in what follows, we rewrite the low-energy Hamiltonian model (3) by introducing new parameters $a_{1,2}, b_{1,2}, c_{1,2}$:

$$H(k_x, k_y) = (a_1 + b_1 k_x^2 + b_2 k_y^2)\tau_0$$
$$+ (a_2 + c_1 k_x^2 + c_2 k_y^2)\tau_x - \chi_y k_y \tau_y. \quad (7)$$

In this notation, the components of Green's function are given

by

$$G_{11,22}(k_x, k_y, i\omega) =$$
$$\frac{1}{2}\left(\frac{1}{i\omega - f_1 + g_1} + \frac{1}{i\omega - f_1 - g_1}\right), \quad (8a)$$

$$G_{12,21}(k_x, k_y, i\omega) =$$
$$\frac{f_2 \pm i\chi_y k_y}{2g_1}\left(\frac{1}{i\omega - f_1 - g_1} - \frac{1}{i\omega - f_1 + g_1}\right), \quad (8b)$$

where the variables f_1, f_2, and g_1 are given by,

$$f_1 = a_1 + b_1 k_x^2 + b_2 k_y^2, \quad (9a)$$

$$f_2 = a_2 + c_1 k_x^2 + c_2 k_y^2, \quad (9b)$$

$$g_1 = \sqrt{f_2^2 + \chi_y^2 k_y^2}. \quad (9c)$$

Substituting the Green's function components (9) into Eq. (6), we obtain the real parts of the optical conductivity tensor, expressed in terms of Dirac-delta functions:

$$
\sigma_{ab}(\omega) = \frac{e^2}{2\pi\hbar\omega} \int\int\int d\Omega \, dk_x \, dk_y \mathcal{F}(\Omega, \omega, \mu, T)
$$
$$
\times \Big\{ h_{ab} \left[\delta(\Omega - f_1 + g_1)\delta(\omega + \Omega - f_1 - g_1) \right.
$$
$$
\left. + \delta(\Omega - f_1 - g_1)\delta(\omega + \Omega - f_1 + g_1) \right]
$$
$$
+ g_{ab}^- \delta(\Omega - f_1 + g_1)\delta(\omega + \Omega - f_1 + g_1)
$$
$$
+ g_{ab}^+ \delta(\Omega - f_1 - g_1)\delta(\omega + \Omega - f_1 - g_1) \Big] \Big\}. \quad (10)
$$

The temperature dependence of the optical conductivity in the continuum regime is given by $\mathcal{F}(\Omega, \omega, \mu, T) = f(\Omega - \mu, T) - f(\Omega + \omega - \mu, T)$, in which μ stands for the chemical potential and $f(X, T)$ is the Fermi-Dirac distribution at temperature T. Also, we have introduced the following new variables to further simplify the final expressions

$$
h_{xx} = 4k_x^2 \left(\frac{c_1^2 \chi_y^2 k_y^2}{f_2^2 + \chi_y^2 k_y^2} \right), \quad (11a)
$$

$$
g_{xx}^\pm = 4k_x^2 \left(b_1^2 + \frac{c_1^2 f_2^2}{f_2^2 + \chi_y^2 k_y^2} \pm \frac{2b_1 c_1 f_2}{\sqrt{f_2^2 + \chi_y^2 k_y^2}} \right), \quad (11b)
$$

$$
h_{xy} = 2c_1 k_x k_y \chi_y^2 \frac{2c_2 k_y^2 - f_2}{f_2^2 + \chi_y^2 k_y^2}, \quad (11c)
$$

$$
g_{xy}^\pm = \frac{2k_x k_y}{f_2^2 + \chi_y^2 k_y^2} \left(c_1 f_2 \pm b_1 \sqrt{f_2^2 + \chi_y^2 k_y^2} \right)
$$
$$
\times \left(2c_2 f_2 \pm 2b_2 \sqrt{f_2^2 + \chi_y^2 k_y^2} + \chi_y^2 \right), \quad (11d)
$$

$$
h_{yy} = \frac{\left(f_2 - 2c_2 k_y^2 \right)^2 \chi_y^2}{f_2^2 + \chi_y^2 k_y^2}, \quad (11e)
$$

$$
g_{yy}^\pm = k_y^2 \left(4b_2^2 + \frac{\left(2c_2 f_2 + \chi_y^2\right)^2}{f_2^2 + \chi_y^2 k_y^2} \pm \frac{4b_2 \left(2c_2 f_2 + \chi_y^2\right)}{\sqrt{f_2^2 + \chi_y^2 k_y^2}} \right), \quad (11f)
$$

Here $h_{yx} = h_{xy}$, $g_{yx}^\pm = g_{xy}^\pm$, and the functions f_1 and f_2 are even functions of momenta k_x and k_y. Therefore, h_{ab} and $g_{ab}^\pm$ determine the symmetry of the optical conductivity integrand [Eq. (10)] with respect to momenta. As is seen, the integrands of $\sigma_{xy}(\omega)$ and $\sigma_{yx}(\omega)$ are odd functions of momenta due to the aforementioned symmetry properties of $h_{xy}, h_{yx}, g_{xy}^\pm$, and $g_{yx}^\pm$. Hence, without performing any further calculations, we find that $\sigma_{xy}(\omega) = \sigma_{yx}(\omega) = 0$ in this system. On the other hand, $h_{xx}, g_{xx}^\pm, h_{yy}$, and $g_{yy}^\pm$ are even functions of momenta, and determine the diagonal optical conductivity tensor components $\sigma_{xx}(\omega)$ and $\sigma_{yy}(\omega)$. The real part of the optical conductivity tensor, Eq. (6), is a complicated function of frequency and momenta that must be evaluated numerically. In what follows, we first compute the optical conductivity as a function of ω and then obtain the components of permittivity through Eq. (4).

In Fig. 3, a study comparable to Fig. 2 is shown, except now we implement the method based on the low-energy effective Hamiltonian, Eq. (3). The parameters for the Hamiltonian are obtained through fitting the model Hamiltonian to the band structure obtained from first-principles around the Γ point (summarized in Table I). The corrected band gap used in the low-energy Hamiltonian is on the order of 1.52 eV, although the magnitude of the band gap plays no role in our conclusions. Comparing Figs. 2(b1) and 2(b2) to Figs. 3(b1) and 3(b2), we see that the two approaches share similarities at low energies ($\omega \lesssim 3$ eV). For example, the generic behaviors are similar, namely, $\epsilon_{xx}(\omega)$ has a flat, smooth variation with ω while $\epsilon_{yy}(\omega)$ has a clearly defined peak at low frequencies. Also, the strongly anisotropic nature of phosphorene is exhibited by the vastly different frequency-dependence of $\epsilon_{xx}(\omega)$ and $\epsilon_{yy}(\omega)$. Both DFT-RPA and the low-energy Hamiltonian model show some similar trends, i.e., the magnitudes follow $|\epsilon_{xx}(\omega)| \ll |\epsilon_{yy}(\omega)|$ within low energies. There are however significant quantitative differences between the two approaches. The origins of these disagreements between the two are two-fold: First, the threshold value for nonzero imaginary permittivity in both $\epsilon_{xx}(\omega)$ and $\epsilon_{yy}(\omega)$ obtained through the low-energy model are identical and equal to $\omega = 1.52$ eV, unlike the different values obtained using DFT-RPA. Hence the low-energy effective model suggests that the same band gap exists in both directions. Second, we find from the low-energy model that the real part of $\epsilon_{yy}(\omega)$ vanishes at $\omega = 2$ eV despite the fairly large nonzero imaginary part of $\epsilon_{yy}(\omega)$ at the same frequency. This feature is absent in the DFT-RPA results and can play a pivotal role in devising novel optoelectronic devices that are sensitive to loss.

Next, we incorporate strain, beginning with a $+10\%$ tensile strain [Fig. 3(c1) and Fig. 3(c2)]. It is observed that now the frequency cutoff for a nonzero imaginary permittivity increases to $\omega = 2.48$ eV, suggesting an enlarged band gap. Also, the permittivity is now nonzero over a larger interval of frequencies, indicating a flattening of the conduction and valence bands following application of this type of strain. Reversing the strain direction, Figs. 3(a1) and 3(a2) display the permittivity components subject to -10% compressive in-plane strain. As seen, both the real and imaginary parts possess Drude absorption peaks, when $\omega \to 0$, indicating metallic behavior. Unlike the DFT-RPA results in Figs. 2(a1) and 2(a2), within the low-energy regime, the imaginary component of the permittivity has a diverging Drude response for low frequencies, and a secondary peak appears at $\omega = 1.33$ eV and $\omega = 1.30$ eV, for $\epsilon_{xx}(\omega)$ and $\epsilon_{yy}(\omega)$, respectively.

In order to fully understand these features, we have plotted the band structure associated with the low-energy effective model along both the k_x and k_y directions. For the strain-free case, the band structure in Figs. 3(b3) and 3(b4) illustrates that the bottom of valence band and the top of conduction band are separated by a gap of 1.52 eV for both directions. This clearly explains the identical threshold values for the nonzero imaginary permittivities shown in Figs. 3(b1) and 3(b2). The exertion of $+10\%$ tensile strain in Figs. 3(c3) and 3(c4), increases the band gap to 2.48 eV for both the k_x and k_y directions, and results in smaller band curvatures compared to unstrained
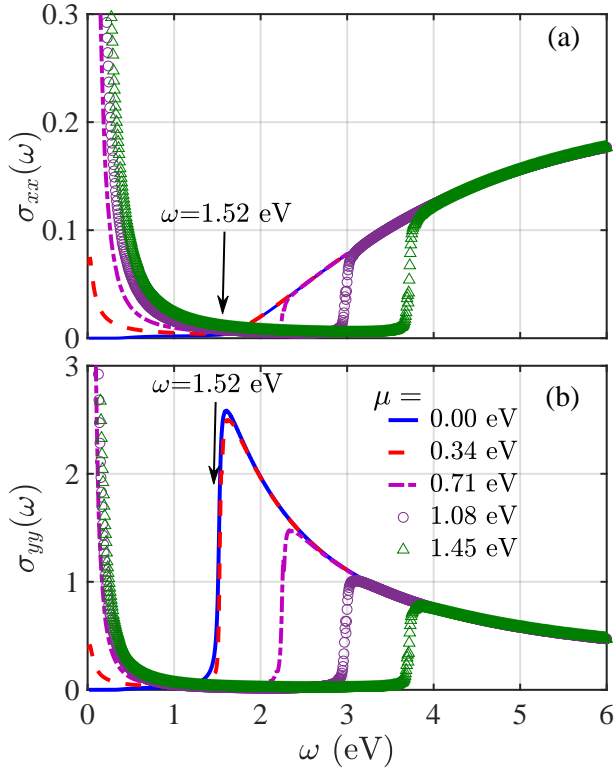
FIG. 4. The normalized real part of the optical conductivity for a strain-free system. Panels (a) and (b) show the diagonal components of the optical conductivity tensor as a function of frequency. The chemical potential takes the values, $\mu = 0, 0.34, 0.71, 1.08, 1.45$ eV.

phosphorene. This accounts for the nonzero imaginary permittivity for frequencies beyond the threshold $\omega = 2.48$ eV in Figs. 3(c1) and 3(c2). For a compressive strain of -10%, Figs. 3(a3) and 3(a4) show a closing of the gap, and the valence band now crosses the Fermi level. This crossing allows for intraband transitions, and thus the Drude peak for very low frequencies, $\omega \to 0$, emerges. As seen, the band curvature now has further increased, resulting in a suppressed peak in the permittivity components [Figs. 3(a1) and 3(a2)]. Also, the two transitions at the energies of $\omega = 1.33$ eV and $\omega = 1.30$ eV (marked in Figs. 3(a3) and 3(a4)) follow from the anisotropic band curvatures in the k_x and k_y directions. Note that one is unable to make an immediate conclusion for identifying the locations of these peaks by looking at the band structure because $\epsilon_{xx,yy}(\omega)$ are obtained by integrating over k_x and k_y. Unlike the zero strain and tensile strain cases, these differing transitions appear as peaks with differing locations in both permittivity components presented in Figs. 3(a1) and 3(a2).

B. Optical conductivity and Drude weight

For completeness, Fig. 4 presents the absorptive components of the dynamical optical conductivity $\text{Re}\{\sigma_{xx}(\omega)\}$ and $\text{Re}\{\sigma_{yy}(\omega)\}$ as a function of frequency in the strain-free sys-

tem. We normalize each component by $\sigma_0 = e^2/4\hbar$. To sample the different regions of the band structure, several representative values of the chemical potential are chosen. When the chemical potential is equal to zero or a value within the band gap, e.g., $\mu = 0.34$ eV (see Figs. 3(b3) and 3(b4)), the optical conductivity is zero at low frequencies and then sharply rises at $\omega = 1.52$ eV (the band gap magnitude), corresponding to the absorption onset. In other words, the onset of nonzero optical absorption is controlled by the band gap edges. The associated transitions are schematically shown by arrows in Figs. 4(a) and 4(b). By increasing the chemical potential, the Drude absorption peak persists as $\omega \to 0$, and the onset of nonzero optical absorption shifts to higher values of ω. Note that when $\mu = 0$ and $\mu = 0.34$ eV, the optical conductivities do not exhibit low-frequency divergences, as those energies reside inside the band gap. Meanwhile, the small $\sigma_{xx,yy}$ that is observed at low frequencies for $\mu = 0.34$ eV is due to a small imaginary term $\eta = 0.01$ eV, added to the frequencies for numerical stability, and is physically equivalent to nonelastic scattering. When the chemical potential crosses the valence band at, e.g., $\mu = 0.71$ eV, and larger values, the Drude response acquires more pronounced values as $\omega \to 0$. Similar to the components of the permittivity tensor, the magnitudes of the components of the optical conductivity tensor obey $|\sigma_{xx}(\omega)| > |\sigma_{yy}(\omega)|$.

From observations of the strain-free case, it is straightforward to understand how strain affects the dynamical optical conductivity. In the presence of e.g., $+10\%$ tensile strain, the optical conductivity has the same structure as the strain-free case except now the band gap increases to 2.48 eV (see Figs. 3(c3) and 3(c4)). Conversely, a -10% compressive strain closes the band gap and therefore, the low-frequency Drude response appears (even when $\mu = 0$), with unequal dissipation threshold values, i.e., $\omega = 1.33$ eV and $\omega = 1.30$ eV at the first peak of the optical conductivity components $\sigma_{xx}(\omega)$ and $\sigma_{yy}(\omega)$, respectively. This anisotropy originates again, from the differing curvatures of the valence and conduction bands in different directions, causing the different interband transition gaps shown in Figs. 3(a3) and 3(a4).

The Drude weight of the anisotropic optical response can be obtained by integrating the Drude response part of the optical conductivity near $\omega \to 0$: $\mathcal{D}_{xx} = \lim_{\omega \to 0}\langle\sigma_{xx}(\omega)\rangle_\omega$, and $\mathcal{D}_{yy} = \lim_{\omega \to 0}\langle\sigma_{yy}(\omega)\rangle_\omega$. Thus, $\mathcal{D}_{xx,yy}$ gives a weight to the zero-frequency divergence of the optical conductivity and is closely associated with intraband transitions. In Fig. 5, we illustrate the Drude weight for both components of the optical conductivity $\sigma_{xx}(\omega)$ and $\sigma_{yy}(\omega)$ as a function of chemical potential μ, for three biaxial strain values of $-10\%, 0\%,$ and $+10\%$. The calculations shown in Figs. 5(a) and 5(b) reaffirm the anisotropic Drude response in this system. Nevertheless, the threshold chemical potential where the Drude weight becomes nonzero, is the same for both the x and y directions. Note that this threshold value for μ, determines the distance between the Fermi level and the bottom of conduction band. When there is a compressive strain on the phosphorene, there is a Drude response, even at $\mu = 0$. The remaining strain cases show that the distance between the Fermi level and the bottom of the conduction band is 0.32 eV and 1.04 eV
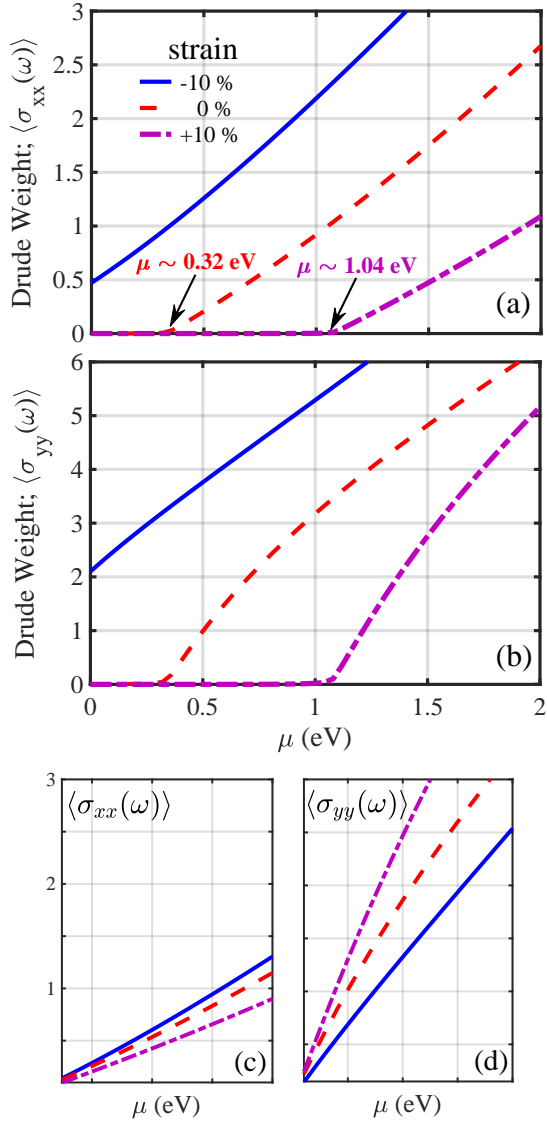
FIG. 5. The Drude weight is shown as a function of chemical potential μ. Three values of biaxial strain are considered: $-10\%, 0\%$, and $+10\%$. The panels (a) and (b) show the Drude weight for the conductivity components $\sigma_{xx}(\omega)$ and $\sigma_{yy}(\omega)$, respectively. For easier comparison, (c) and (d) show each curve from (a) and (b) shifted to begin at the origin.
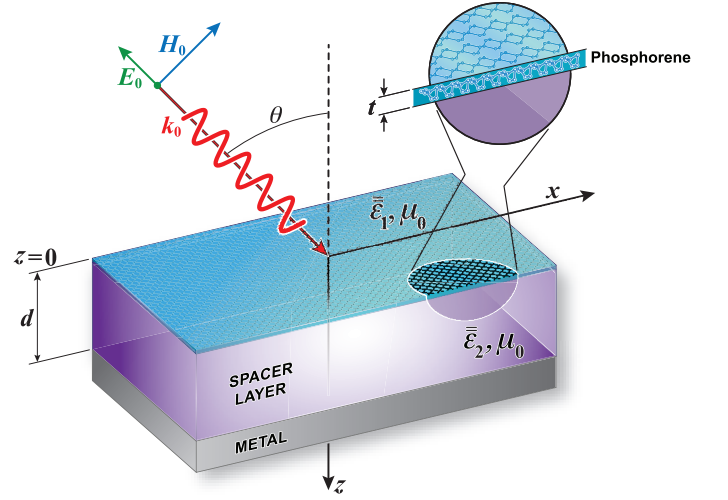

FIG. 6. Schematic of the configuration involving a single-layer of phosphorene with an effective thickness t on top of a spacer layer of thickness d, and metal reflecting substrate. The phosphorene resides in the x-y plane. The phosphorene layer is exposed to an electromagnetic wave from the vacuum region, where the incident electric field is polarized along $\hat{y}$, and the magnetic field is polarized in the x-z plane. The incident wavevector $\boldsymbol{k}_0$ makes an angle θ with the z axis. The crystallography principal directions are set as follows: $x \equiv a$, $y \equiv b$, and $z \equiv c$.

findings, we have performed checks by summing up the contributions from the vertical intraband transitions through the following formula:[35,40]

$$\lim_{\omega \to 0} \left\langle \sigma_{xx(yy)}(\omega) \right\rangle \propto \int \sum_{k_{x(y)}^i} \left| \frac{dE(k_{x(y)}, k_{y(x)})}{dk_{x(y)}} \right| dk_{y(x)}.$$

(12)

As seen, this formula accounts for the vertical intraband transitions through the slope of the conduction band $E(k_x, k_y)$ at $E(k_x, k_y) = \mu$, where $k_{x(y)}^i$ are the roots of $E(k_x, k_y) - \mu = 0$. The total Drude weight is proportional to the integration of all these states over $k_{y(x)}$. These calculations were found to have perfect agreement with those presented in Fig. 5.

C. Implications for device design

We now demonstrate that having an accurate microscopic model for predicting the optical response of a material is crucial for the successful design of even a simple optics device, which in this case involves phosphorene. As seen in Fig. 6, the basic design involves a phosphorene layer deposited on top of an insulator layer with thickness d, and a perfect conductor, serving as a back plate. The incident EM wave, propagating through vacuum, impinges on the device from the phosphorene side with an angle of θ measured from the normal to the phosphorene plane. In general, the permittivity tensor $\bar{\bar{\varepsilon}}$ and permeability tensor $\bar{\bar{\mu}}$ in the principal coordinates take the following biaxial forms for a given (uniform) region

in the presence of 0% and $+10\%$ strain, which are in excellent agreement with the band structure diagrams in Fig. 3. To illustrate the nonuniformity of the Drude response, the Drude weight curves are shifted to the origin in Figs. 5(c) and 5(d). As seen, the steepest response belongs to $\mathcal{D}_{yy}$ for the case of $+10\%$ strain, whereas $\mathcal{D}_{xx}$ has a moderate response for the same strain value. This counterintuitive finding cannot be deduced by simple examination of the conduction bands in Fig. 3. This is due to the fact that the band structure is nonuniform in the k_x-k_y plane (see e.g., the isoenergy contour plots presented in Ref. 34), and to obtain the Drude weight, the intraband transitions are integrated over the entire isoenergy curves in the k_x-k_y plane. Nevertheless, to confirm these

$(n = 0, 1, 2)$:

$$\bar{\bar{\varepsilon}}_n = \varepsilon_{nx}\hat{\boldsymbol{x}}\hat{\boldsymbol{x}} + \varepsilon_{ny}\hat{\boldsymbol{y}}\hat{\boldsymbol{y}} + \varepsilon_{nz}\hat{\boldsymbol{z}}\hat{\boldsymbol{z}}, \tag{13a}$$

$$\bar{\bar{\mu}}_n = \mu_{nx}\hat{\boldsymbol{x}}\hat{\boldsymbol{x}} + \mu_{ny}\hat{\boldsymbol{y}}\hat{\boldsymbol{y}} + \mu_{nz}\hat{\boldsymbol{z}}\hat{\boldsymbol{z}}, \tag{13b}$$

where n denotes the vacuum region ($n = 0$), the phosphorene layer ($n = 1$), or the spacer layer ($n = 2$).

We now investigate the absorption of EM waves from the layered configuration shown in Fig. 6. The metallic back plate for simplicity is taken to have perfect conductivity (PEC). The electric field of the incident wave is polarized along $\hat{\boldsymbol{y}}$, and is incident from the vacuum region with wavevector $\boldsymbol{k}_0$ in the x-z plane: $\boldsymbol{k}_0 = \hat{\boldsymbol{x}}k_{0x} + \hat{\boldsymbol{z}}k_{0z}$, where $k_{0x} = k_0 \sin\theta$, and $k_{0z} = k_0 \cos\theta$. Since $\bar{\bar{\varepsilon}}_n$ has no off-diagonal components, the transverse electric (TE) and transverse magnetic (TM) modes are decoupled. The absorption can be calculated from Maxwell's equations. Assuming a harmonic time dependence $\exp(-i\omega t)$ for the EM field, we have,

$$\begin{aligned} \boldsymbol{\nabla} \times \boldsymbol{E}_n &= +i\omega\mu_0\bar{\bar{\mu}}_n\cdot\boldsymbol{H}_n, \\ \boldsymbol{\nabla} \times \boldsymbol{H}_n &= -i\omega\varepsilon_0\bar{\bar{\varepsilon}}_n\cdot\boldsymbol{E}_n. \end{aligned} \tag{14}$$

Combining Eqs. (14), we get,

$$\begin{aligned} \boldsymbol{\nabla} \times \left(\bar{\bar{\mu}}_n^{-1}\cdot\boldsymbol{\nabla}\times\boldsymbol{E}\right) &= k_0^2\left(\bar{\bar{\varepsilon}}_n\cdot\boldsymbol{E}\right), \\ \boldsymbol{\nabla} \times \left(\bar{\bar{\varepsilon}}_n^{-1}\cdot\boldsymbol{\nabla}\times\boldsymbol{H}\right) &= k_0^2\left(\bar{\bar{\mu}}_n\cdot\boldsymbol{H}\right). \end{aligned} \tag{15}$$

We consider TE modes, corresponding to non-zero field components E_{ny}, H_{nx}, and H_{nz}. The electric field E_{ny} satisfies the following wave equation:

$$\frac{1}{\mu_{nz}}\frac{\partial^2 E_{ny}}{\partial x^2} + \frac{1}{\mu_{nx}}\frac{\partial^2 E_{ny}}{\partial z^2} + k_0^2\varepsilon_{ny}E_{ny} = 0, \tag{16}$$

which admits separable solutions of the form $\psi(z)\exp(ik_{0x}x)$. In what follows, we consider non-magnetic media, so that $\mu_{nx} = \mu_{nz} = 1$. The parallel wave-vector k_{0x} is determined by the incident wave, and is conserved across the interface. The form of $\psi(z)$ then simply involves linear combinations of the exponential $\exp(ik_{nz}z)$ for a given region. Thus, the electric field in the vacuum region, $\boldsymbol{E}_0$, is written in terms of incident and reflected waves: $\boldsymbol{E}_0 = (e^{ik_{0z}z} + E_{0ry}e^{-ik_{0z}z})e^{ik_{0x}x}\hat{\boldsymbol{y}}$. From the electric field, we can use Eq. (14) to easily deduce the magnetic field components. Due to the presence of the perfect metal plate, in the spacer region, the general form of the electric field is written in terms of standing waves: $E_{2y} = E_2\sin[k_2(z-d)]e^{ik_{0x}x}$, where from Eq. (16), the wave number k_2 is given by, $k_2 = \pm\sqrt{\varepsilon_2 k_0^2 - k_{0x}^2}$. Note that the boundary condition that E_{2y} vanishes at the ground plane ($z=d$) is accounted for (see Fig. 6). To construct the $\boldsymbol{H}$ fields we use Eqs. (14) to arrive at, $\boldsymbol{H}_n = (-\partial_z E_{ny}, \partial_x E_{ny})/(i\eta_0 k_0)$, for $n = 0, 2$, and where $\eta_0 = \sqrt{\mu_0/\varepsilon_0}$ is the impedance of free space. The presence of phosphorene enters in the boundary condition for the tangential component of the magnetic field by writing,

$$\hat{\mathbf{n}} \times (\boldsymbol{H}_0 - \boldsymbol{H}_2) = \boldsymbol{J}, \tag{17}$$

where $\hat{\mathbf{n}}$ is the normal to the vacuum/phosphorene interface, and $\boldsymbol{J}$ is the current density. Thus, we have

$H_{2x}(z=0) - H_{0x}(z=0) = J_y$, where Ohm's Law connects the surface current density J_y to the electric field in the usual way: $\boldsymbol{J} = \bar{\bar{\sigma}}\boldsymbol{E}$. The dielectric tensor in turn is defined through the surface conductivity tensor $\bar{\bar{\sigma}}$ via,

$$\varepsilon_{ab}(\omega) = \delta_{ab} + \frac{i\sigma_{ab}(\omega)}{t\varepsilon_0\omega}, \tag{18}$$

where t is the effective thickness of the phosphorene layer, which we take to be $\approx 1\,\mathrm{nm}$ (see Fig. 6). One can also consider the phosphorene layer as a finite sized slab, like the spacer layer, and solve for the fields within the layer. This approach leads to equivalent results, but treating the phosphorene layer as a current sheet with infinitesimal thickness leads to simpler expressions. Upon matching the tangential electric fields at the vacuum/spacer interface, and using Eq. (17), it is straightforward to determine the unknown coefficients E_{0ry} and E_2. First, the reflection coefficient E_{0ry} is found to be,

$$E_{0ry} = -1 + \frac{2\cos\theta}{i\kappa_2\cot(k_2 d) + \cos\theta + \eta_0\sigma_{yy}}, \tag{19}$$

where we define $\kappa_2 = k_2/k_0$. The coefficient E_2 for the electric field in the spacer region is similarly found to be

$$E_2 = -\frac{2\cos\theta\csc(k_2 d)}{\cos\theta + \eta_0\sigma_{yy} + i\kappa_2\cot(k_2 d)}, \tag{20}$$

where from Eq. (18), the dimensionless quantity $\eta_0\sigma_{yy}$ can be expressed in terms of the permittivity: $\eta_0\sigma_{yy} = i(1-\varepsilon_{yy})k_0 t$.

The fraction of energy that is absorbed by the system is determined by the absorptance (A): $A = 1 - R$, where R is the reflectance index. Note that due to the metallic substrate, there is no transmission of EM fields into the region $z > d$. In determining the absorptance of the phosphorene system, we consider the time-averaged Poynting vector in the direction perpendicular to the interfaces (the z direction), $S_{0z} = \Re\{-E_{0y}H_{0x}^*\}/2$. Upon inserting the electric and magnetic fields for the vacuum region, we find, $A = 1 - |E_{0ry}|^2$, where $A = S_{z0}/S_0$, and $S_0 \equiv k_{0z}/(2\varepsilon_0\omega)$ is the time-averaged Poynting vector for a plane wave traveling in the z direction.

In the following, we consider representative material and geometric parameters, and demonstrate how the differing predictions from the low-energy model and DFT-RPA can considerably influence the absorption of EM energy in a phosphorene-based system. We illustrate in Fig. 7 the absorptance as a function of incident angle θ, and thickness of the insulator layer, d. The absorptance is determined after the permittivity tensor is calculated from the DFT-RPA and low-energy models. Results are shown in in Figs. 7(a) and 7(b) for the DFT-RPA approach, and in Figs. 7(c) and 7(d), for the low-energy model. The frequency of the incident EM wave is set to $\omega = 0.06$ eV in Figs. 7(a) and 7(c), and $\omega = 1.4$ eV in Figs. 7(b) and 7(d). In all cases, the chemical potential is set to zero and a compressive strain of -10% is considered. Considering first the DFT-RPA results in 7(a) and 7(b), it is evident that over most of the parameter space, the incident beam reflects completely off the structure ($A \approx 0$). There is only a small region of the diagram in 7(b) where there is near
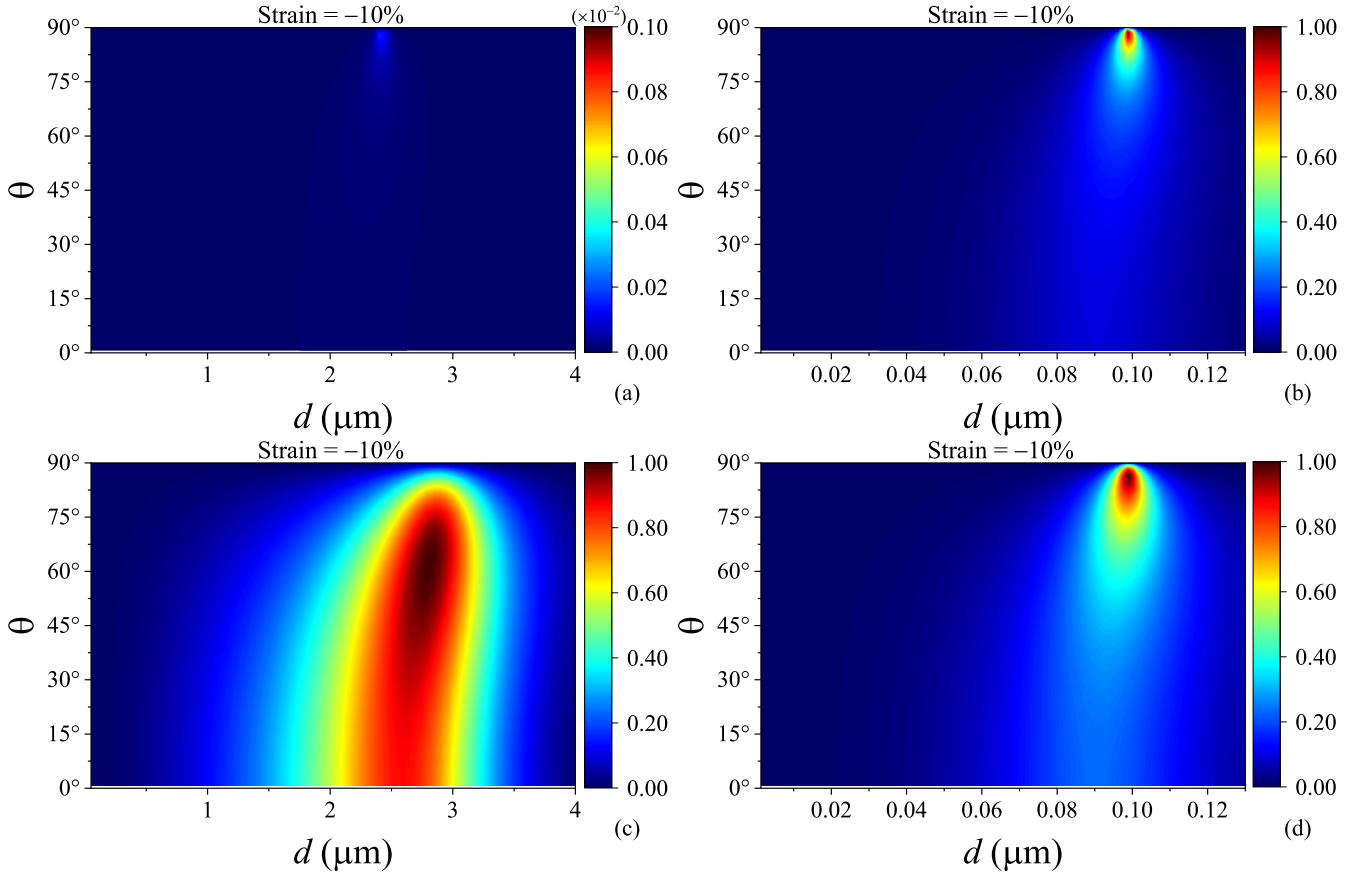
FIG. 7. The absorptance as a function of the angle of incident light θ and the thickness of the insulator layer d. The DFT data and low energy model are used in the top and bottom rows, respectively. The frequency of the incident light is set to $\omega = 0.06$ eV (left column) and 1.4 eV (right column). The biaxial strain is fixed at -10%, and for proper comparisons, the chemical potential is set to $\mu = 0$.

perfect absorption for near-grazing incidences ($\theta \approx 90°$). The low-energy model in Fig. 7(c) however predicts an extremely strong absorption region within $2\mu m \lesssim d \lesssim 3\mu m$. In contrast to the DFT approach, the low-energy model results in nearly perfect absorption within $45° \lesssim \theta \lesssim 75°$. Increasing the frequency to $\omega = 1.4$ eV in Fig. 7(d), the results of DFT and the low-energy model become more similar, although the low-energy model still predicts stronger absorption over a broader range of spacer layer thicknesses and angles θ.

To further contrast the DFT-RPA method and low-energy model, Fig. 8 displays the absorptance as a function of θ (left column) and ω (right column), for three values of the biaxial strain: -10%, 0%, and $+10\%$. Results in the left column have a set frequency $\omega = 1.4$ eV, and an insulator thickness of $d = 100$ nm, whereas the right column has $d = 310$ nm and $\theta = 80°$. Figure 8(c) corresponds to a slice of Figs. 7(b) and 7(d), and more clearly shows how the DFT results cause a shifting of the near-perfect absorption peak towards $\theta = 90°$. The discrepancies between the two models is seen to dramatically increase for the other strain values shown in 8(a) and 8(b). Examining the frequency response in Figs. 8(d)-8(f), it is evident that the two models again lead to different absorption characteristics. For zero strain [Fig. 8(d)] the absorptance profiles are similar but shifted in frequency. When a tensile

strain of $+10\%$ is applied to the phosphorene [Fig. 8(e)], the DFT approach shows a small amount of absorption, but overall both models predict that the incident EM wave is mostly reflected over the given frequency window. When a compressive strain of -10% is applied [Fig. 8(f)], there is again a shift similar to 8(d), but now the magnitudes of the peaks are much different, with the low-energy model exhibiting near perfect absorption at $\omega = 1.4$ eV. These discrepancies originate mainly from the different predictions for the permittivities, where e.g., the DFT and low-energy methods give different dissipation thresholds and significant amplitude variations (see Figs. 2 and 3).

IV. CONCLUSIONS

Due to the fundamental importance of light-matter interactions, we have investigated the permittivity of phosphorene, subject to in-plane strain, as a representative material platform, using two approaches: One approach employed density functional theory combined with the random phase approximation (DFT-RPA), and the other method involved a low-energy effective Hamiltonian model and Green's function. The permittivity components for this strongly anisotropic
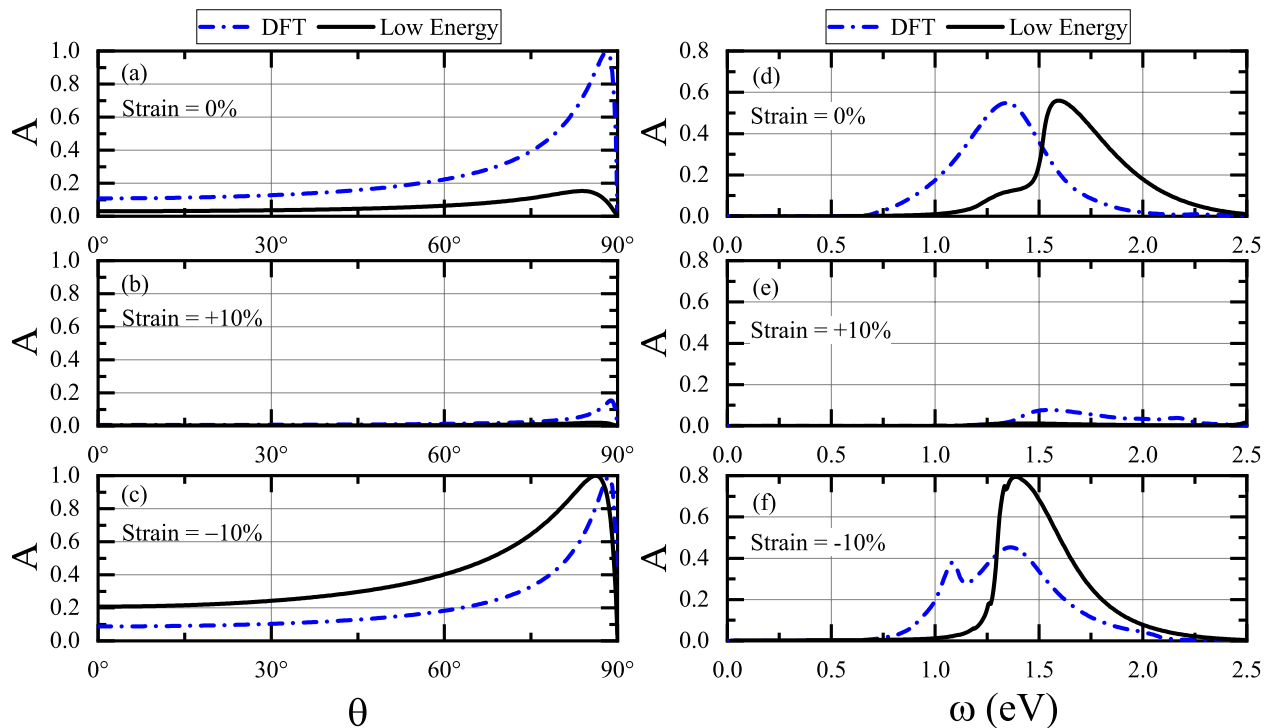
FIG. 8. The absorptance A calculated by employing the results of DFT and low-energy models. Three biaxial strain values are considered (as labeled): -10%, 0%, $+10\%$. The left column shows A as a function of the incident angle θ, at fixed frequency $\omega = 1.4$ eV, and for an insulator thickness of $d = 100$ nm. The right column has A as a function of frequency of the incident EM wave at an incident angle of $\theta = 80°$, and $d = 310$ nm. In all cases, the chemical potential is zero; $\mu = 0$.

material are fully explained by its associated band structures, transitions, and optical conductivities within the low-energy formalism. However, the results of DFT-RPA and the corresponding band structures calculated from the Perdew-Burke-Ernzerhof functional, showed considerable discrepancies. The DFT calculations were repeated using two different packages, and similar results were obtained. Although some broad, generic trends for the frequency dispersion of the permittivity components were in agreement for both approaches, several important differences stood out, including the onset of the imaginary part of the Drude response that revealed important fundamental physical characteristics of a material, such as the band gap, and interband and intraband transitions. Our results suggest that the DFT-RPA method implemented in many types of DFT packages needs to be revisited, and improvements made so that the results are at least more consistent with the associated band structures. Accurate predictions for the permittivity and optical conductivity are of pivotal importance in determining the physical properties of materials and designing novel optoelectronics devices.

[1] R. Gutzler, M. Garg, C. R. Ast, K. Kuhnke, K. Kern, Light–matter interaction at atomic scales, Nat. Rev. Phys. (2021). https://doi.org/10.1038/s42254-021-00306-5

[2] F. N. Xia, H. Wang, and Y. C. Jia, Rediscovering black phosphorus as an anisotropic layered material for optoelectronics and electronics, Nat. Commun. 5, 4458 (2014).

[3] T. Ahmed, etal Fully Light-Controlled Memory and Neuromorphic Computation in Layered Black Phosphorus, Advanced Materials (2021).

[4] A. Rodin, M. Trushin, A. Carvalho, A. H. Castro Neto, Collective Excitations in 2D Materials, Nat. Rev. Phys. 2, 524 (2020).

[5] A. Carvalho, P. E. Trevisanutto, S. Taioli, A. H. Castro Neto, Computational methods for 2D materials modelling, arXiv:2101.06859.

[6] M. Alidoust, K. Halterman, D. Pan, M. Willatzen, J. Akola, Strain-Engineered Widely-Tunable Perfect Absorption Angle in

Black Phosphorus from First-Principles, Phys. Rev. B 102, 115307 (2020).

[7] S. Biswas, W. S. Whitney, M. Y. Grajower, K. Watanabe, T. Taniguchi, H. A. Bechtel, G. R. Rossman, H. A. Atwater, Tunable intraband optical conductivity and polarization-dependent epsilon-near-zero behavior in black phosphorus, Sci. Adv. 7, eabd4623 (2021).

[8] V. Tran, R. Soklaski, Y. Liang, and L. Yang, Layer-controlled band gap and anisotropic excitons in few-layer black phosphorus, Phys. Rev. B 89, 235319 (2014).

[9] Y. Wei, F. Lu, T. Zhou, X. Luo, and Y. Zhao, Stacking sequences of black phosphorous allotropes and the corresponding few-layer phosphorenes, Physical Chemistry Chemical Physics 20, 10185 (2018).

[10] T. Fang, T. Liu, Z. Jiang, R. Yang, P. Servati, and G. Xia, Fabrication and the Interlayer Coupling Effect of Twisted Stacked Black phosphorous for Optical Applications, ACS Appl. Nano Mater. 2, 3138 (2019).

[11] Z. Zhang, L. Li, J. Horng, N. Z. Wang, F. Yang, Y. Yu, Y. Zhang, G. Chen, K. Watanabe, T. Taniguchi, X. H. Chen, F. Wang, Y. Zhang, Strain-modulated bandgap and piezoresistive effect in black phosphorous field-effect transistors, Nano Lett. 17 6097-6103 (2017).

[12] S. Das, W. Zhang, M. Demarteau, A. Hoffmann, M. Dubey, A. Roelofs, Tunable transport gap in phosphorene, Nano Lett. 14 5733-5739 (2014).

[13] Z. Qin, G. Xie, H. Zhang, C. Zhao, P. Yuan, S. Wen, and L. Qian, Black phosphorous as saturable absorber for the Q-switched Er:ZBLAN fiber laser at 28 μm, Opt. Express 23, 24713 (2015)

[14] A. Carvalho, M. Wang, X. Zhu, A. Rodin, H. Su, and A. C. Neto, Phosphorene: from theory to applications, Nat. Rev. Materials 1, Article number: 16061 (2016).

[15] G. Zhang, S. Huang, F. Wang, Q. Xing, C. Song, C. Wang, Y. Lei, M. Huang, and H. Yan, The optical conductivity of few-layer black phosphorus by infrared spectroscopy, Nat. Comm.11, 1847 (2020).

[16] A. H. Castro Neto, F. Guinea, N. M. R. Peres, K. S. Novoselov, and A. K. Geim, The electronic properties of graphene, Rev. Mod. Phys. 81, 109 (2009).

[17] H. Liu, A. T. Neal, Z. Zhu, Z. Luo, X. Xu, D. Tomanek, and P. D. Ye, Phosphorene: an unexplored 2D semiconductor with a high hole mobility, ACS NANO 8, 4033 (2014).

[18] D. Bohm and D. Pines, A collective description of electron interactions. I. Magnetic interactions Phys. Rev. 82, 625 (1951).

[19] M. W. Jørgensen and S. P. A. Sauer, Benchmarking doubles-corrected random-phase approximation methods for frequency dependent polarizabilities: Aromatic molecules calculated at the RPA, HRPA, RPA(D), HRPA(D), and SOPPA levels, J. Chem. Phys. 152, 234101 (2020).

[20] E. van Loon, M. Rosner, M. I. Katsnelson, T. O. Wehling, Random Phase Approximation for gapped systems: role of vertex corrections and applicability of the constrained random phase approximation, arXiv:2103.04419.

[21] M. Gajdos, K. Hummer, G. Kresse, J. Furthmüller and F. Bechstedt, Linear optical properties in the projected-augmented wave methodology, Phys. Rev. B 73, 045112 (2006).

[22] E. Sasıoglu, C. Friedrich, and S. Blugel, Effective Coulomb interaction in transition metals from constrained random-phase approximation, Phys. Rev. B 83, 121101(R) (2011).

[23] H. Shinaoka, M. Troyer, and P. Werner Accuracy of downfolding based on the constrained random-phase approximation, Phys. Rev. B 91, 245156 (2015).

[24] C. Honerkamp, H. Shinaoka, F. F. Assaad, and P. Werner Limitations of constrained random phase approximation downfolding, Phys. Rev. B 98, 235151 (2018).

[25] X.-J. Han, P. Werner, and C. Honerkamp, Investigation of the effective interactions for the Emery model by the constrained random-phase approximation and constrained functional renormalization group, Phys. Rev. B 103, 125130 (2021).

[26] M. S. Hybertsen and S. G. Louie, Ab initio static dielectric matrices from the density-functional approach. I. Formulation and application to semiconductors and insulators, Phys. Rev. B 35, 5585 (1987).

[27] M. N. Gjerding, M. Pandey and K. S. Thygesen, Band structure engineered layered metals for low-loss plasmonics, Nat. Commun. 8, 1 (2017).

[28] J. J. Mortensen, L. B. Hansen, K. W. Jacobsen , Real-space grid implementation of the projector augmented wave method, Phys. Rev. B 71, 035109 (2005).

[29] J. Enkovaara, C. Rostgaard, J.J. Mortensen, J. Chen, M. Dułak, L. Ferrighi, J. Gavnholt, C. Glinsvad, V. Haikola, H.A. Hansen, et al., Electronic structure calculations with GPAW: a real-space implementation of the projector augmented-wave method, J. Phys. Condens. Matter 22, 253202 (2010).

[30] L. Voon, A. Lopez-Bezanilla, J. Wang, Y. Zhang, M. Willatzen, Effective Hamiltonians for phosphorene and silicene, New J. Phys. **17**, 025004 (2015).

[31] L. Voon, J. Wang, Y. Zhang, and M. Willatzen, Band parameters of phosphorene, J. Phys.: Conf. Ser. **633**, 012042 (2015).

[32] M. Alidoust, M. Willatzen, and A.-P. Jauho, Strain-engineered Majorana zero energy modes and φ_0 Josephson state in black phosphorus, Phys. Rev. B 98, 085414 (2018).

[33] M. Alidoust, M. Willatzen, and A.-P. Jauho, Fraunhofer response and supercurrent spin switching in black phosphorus with strain and disorder, Phys. Rev. B 98, 184505 (2018).

[34] M. Alidoust, M. Willatzen, and A.-P. Jauho, Control of superconducting pairing symmetries in monolayer black phosphorus, Phys. Rev. B 99, 125417 (2019).

[35] G.D. Mahan, Many–Particle Physics (Plenum Press, New York) 1990.

[36] M. Tahir, P. Vasilopoulos, F. M. Peeters , Magneto-optical transport properties of monolayer phosphorene, Phys. Rev. B 92, 045420 (2015).

[37] J. Jang, S. Ahn, and H. Min, Optical conductivity of black phosphorus with a tunable electronic structure, 2D Mater. 6, 025029 (2019).

[38] C. H. Yang, J. Y. Zhang, G. X. Wang, and C. Zhang, Dependence of the optical conductivity on the uniaxial and biaxial strains in black phosphorene, Phys. Rev. B 97, 245408 (2018).

[39] D. Q. Khoa, B. D. Hoi, T. C. Phong, Transverse Zeeman magnetic field effects on the dynamical dielectric function of monolayer phosphorene: Beyond the continuum approximation, J. Mag. Mag. Mat. 491, 165637 (2019).

[40] C. Kittel, Introduction to Solid State Physics, California: John Wiley & Sons, Inc., 2004.

[41] D. Pines and P. Nozieres, The theory of quantum liquids, (Benjamin, New York 1966).